



universität
wien

DISSERTATION

Titel der Dissertation

„Variable jump barriers in Monte-Carlo simulations of atom configuration changes in alloys“

Verfasser

Mag. Martin Leitner

angestrebter akademischer Grad

Doktor der Naturwissenschaften (Dr. rer. nat.)

Wien, 2012

Studienkennzahl lt. Studienblatt:	A 091 411
Dissertationsgebiet lt. Studienblatt:	Studium der Naturwissenschaften Physik
Betreuerin / Betreuer:	Ao. Univ. Prof. Dr. Wolfgang Püschl

Zusammenfassung (German)

Eine Vielzahl günstiger Eigenschaften von Legierungen - z. B. Festigkeit, Widerstand gegen Korrosion oder magnetische Anisotropie - hängt von der mikroskopischen Anordnung der beteiligten Atomsorten auf dem Kristallgitter ab. Um die Kinetik solcher Atomkonfigurationen in intermetallischen Verbindungen zu untersuchen, werden oft Kinetische Monte-Carlo Simulationen (KMC) eingesetzt. In sie gehen als einzige kinetische Parameter die Wahrscheinlichkeiten für einzelne Atomsprünge ein. Diese Wahrscheinlichkeiten werden, unter Zuhilfenahme der Transition State Theory, durch den Energieunterschied zwischen dem ursprünglichen Gleichgewichtszustand und einem Sattelpunkt ('Transition State') bestimmt. Wirft man einen Blick in die existierende Literatur, stellt man oft fest, dass speziell für die Energie des Sattelpunkts relativ ungenaue Ansätze gemacht werden, z.B. wird sie auf einen festen Wert gesetzt oder auf die Art des springenden Atoms bezogen.

Diese Dissertation ersetzt diese approximative Behandlung dadurch, dass der Einfluss der atomaren Umgebung auf den spezifischen Wert der Energie des Sattelpunkts in die Simulation einfließt. Für diese Studie wurden die Energieprofile einer grossen Anzahl von verschiedenen Atomsprüngen mit Hilfe der aktuell genauesten Methode - *ab-initio*-Berechnungen basierend auf der Dichtefunktionaltheorie - analysiert. Die Berechnungen wurden mit dem Vienna Ab Initio Software Package (VASP) durchgeführt, dem am besten entwickelten und meistbenutzten Programm auf diesem Gebiet.

Als Modellsystem wurde die technologisch interessante intermetallische Verbindung Ni_3Al , die in der $L1_2$ -Struktur kristallisiert, gewählt. In dieser Legierung passiert Diffusion durch Nächst-Nachbarschaftssprünge von Atomen in Leerstellen. Aufgrund der Kristallstruktur müssen springende Atome ein enges Fenster passieren, das von gemeinsamen Nachbarschaftsatomen von Anfangs- und Endposition gebildet wird. Der Einfluss der Umgebungskonfiguration wurde mit Hilfe einer 'reinen' Barrierenhöhe analysiert, die dem Mittelwert von Hin- und Rücksprung entspricht. Die Besetzung des 4-Atom-Fensters hat erwartungsgemäss den grössten Einfluss auf die Barrierenhöhe. Die Ergebnisse wurden für $2 \times 2 \times 2$ und $3 \times 3 \times 3$ Simulationszellen als Tabellen angegeben und können, für die Berechnung von einzelnen Sprungwahrscheinlichkeiten benutzt werden.

Die atomare Besetzung in weiterer Entfernung zum springenden Atom wurde systematisch untersucht und erwies sich als Einfluss zweiter Ordnung. Der Einfluss der umgebungsabhängigen Sattelpunktenergien auf die Kinetik wurde mit Hilfe von KMC Simulationen an entordnenden Systemen gezeigt. Es wurde ein bemerkenswert geändertes Verhalten sowohl in der gesamten Fernordnungsparameter-Kinetik als auch in den detaillierten Sprungstatistiken gefunden. Sprungtypen werden stark nach niedrigen Sattelpunktenergien selektiert, und die Gesamtkinetik verlangsamt sich aufgrund von starken Korrelationseffekten.

Abstract

Most favorable properties like strength, corrosion resistance and magnetic anisotropy of alloy materials depend on the microscopic arrangement of component atoms on the crystal lattice. Kinetic Monte-Carlo simulation (KMC) is a widely used and valuable tool for the investigation of atom configuration kinetics in alloys such as intermetallic compounds. Its sole input is the probabilities of single atom jumps. According to transition state theory they are determined by the energy difference between an initial equilibrium state and a transitional saddle point state of the jumping atom. In existing literature, especially for the saddle point energy usually only rough assumptions are made, mostly setting it constant or relating it to the type of jumping atom.

This thesis sets out to remedy this specific weakness taking account of the atomic environment of the saddle point. For a systematic study of the influence of atomic surroundings, an extensive study of jump energy profiles was undertaken using the currently best method available for calculating atomic interaction in solids, i. e. *ab initio* calculations based on density functional theory. The VASP code was used as the most proven and elaborate software for this purpose.

The L1₂-ordered, technically relevant intermetallic Ni₃Al was taken as a model system. Diffusion here takes place via a nearest-neighbor vacancy exchange mechanism. Due to the crystal structure, jumping atoms have to pass through a narrow window consisting of nearest neighbors common to the initial and final positions of the jumping atom. The effect of the atomic neighborhood was investigated in terms of a pure barrier height being the average of the forward and backward jump barrier heights. The occupancy of the 4-atom window according to expectation exerts the main influence on barrier height. The results are given both for 2x2x2 and 3x3x3 calculation supercells as tables which can be used for the construction of individual jump probabilities. The influence of atom occupation in more distant coordination shells is found to be less important and decays systematically with distance.

The effect on kinetics of environment dependent saddle point energies was demonstrated in model KMC simulations of disordering systems. There is a remarkable change both in overall kinetics of the long range order parameter and detailed jump statistics. Jump types are strongly selected for low saddle points, and overall kinetics appears slowed down due to strong correlation effects.

Contents

Zusammenfassung (German)	iii
Abstract	v
List of Figures	xiii
List of Tables	xix
1 Introduction	1
1.1 General motivation	1
1.2 Organization of this work	1
1.3 Overview	2
2 Kinetic Monte-Carlo Simulations (KMC)	5
2.1 The single atom jump as a Markov process	5
2.2 Metropolis/Glauber algorithms	7
2.3 Residence time algorithm (RTA)	8
3 The single atom jump	11
3.1 Transition State Theory	11
3.2 The Nudged Elastic Band (NEB) method	14
4 The $L1_2$ structure	17
4.1 General remarks	17
4.2 Properties of the $L1_2$ structure	18
4.2.1 Conventional and primitive unit cell	18
4.2.2 Division into sublattices and long range order parameter	20
4.2.3 Pair correlation numbers	22
4.2.4 Point defects in the $L1_2$ structure	23
4.3 The 4-atom window in the $L1_2$ structure	25
4.4 Classification of jumps and window types	27
4.4.1 Classification of jump types in the $L1_2$ structure	27
4.4.2 Classification of window types	28
5 Density Functional Theory	29

5.1	General remarks	29
5.2	The many-body Schrödinger equation	30
5.3	Density Functional Theory	33
5.4	Approximations and Implementation	35
5.5	VASP	35
6	Publication in <i>Intermetallics</i>	37
6.1	Abstract	38
6.2	Introduction	38
6.3	Jump rates and energy barriers	39
6.4	Ab initio calculation of jump profiles	41
6.5	Results for the jump profiles	43
6.6	MC Simulation results and discussion	45
6.7	Conclusions	52
7	Publication in <i>Solid State Phenomena</i>	55
7.1	Abstract	56
7.2	Introduction	56
7.3	Jump rates and energy barriers	57
7.4	Results	59
7.5	Conclusions	62
8	Additional results for $L1_2 Ni_3Al$	65
8.1	Ab initio calculations: Convergence and validation	66
8.1.1	Methodology	66
8.1.2	Results: equilibrium values of pure Metals Ni and Al	67
8.1.3	Results: equilibrium values of undisturbed $L1_2 Ni_3Al$	69
8.2	Ab initio calculations: The size of the supercell	71
8.2.1	Methodology	71
8.2.2	Results	73
8.3	Realistic jump paths: straight vs. curved	79
8.3.1	General remarks	79
8.3.2	Methodology	81
8.3.2.1	Results	83
8.4	Dependence of saddle point on neighboring defects at various distances	93
9	Summary and Outlook	99
	Bibliography	103
	Publications and presentations	107

Curriculum Vitae

109

List of Figures

2.1	Schematic picture of the state before the single atom jump: a vacancy (square) is surrounded by Z nearest-neighbor atoms (dots). Each of this atoms may exchange their position with the vacancy. This corresponds to the state α of the system. After the j th atom has jumped into the vacancy the system finally reaches state β^j	6
2.2	Atom jumps as a Markov process, time evolution of probabilities (example): initial state α (dashed line) follow-up states β^j (full lines). At the marked coordinates the probability of the initial state has decreased to $1/e$	6
3.1	Energy landscape of a jump process. From: [18]	12
4.1	Left: Conventional cubic cell of the $L1_2$ structure. B atoms (white) are located on the cube corners and A atoms (black) on the face centers.	18
4.2	Nearest neighbor environments of the α - (left) and β -sublattice (right) for the state of perfect order. On the α -sublattice A atoms (black) have 8 further A atoms and 4 B atoms as nearest neighbors. On the β -sublattice a B atom (white) is surrounded by 12 A atoms in the first coordination shell.	20
4.3	Possible point defects (vacancies - left and antisites - right) in the $L1_2$ structure on the minority (top) and majority (bottom) sublattice.	24
4.4	4-atom window between an A atom located on the α -sublattice and a vacancy on the β -sublattice. It is made up of the four common nearest neighbor atoms.	25
4.5	4-atom window between 2 lattice positions in the $L1_2$ structure for (a): B atoms and (b): A atoms and a neighboring vacancy. Note that in the case of an A atom the explicit configuration of the window depends on the sublattice of the neighboring vacant lattice site.	26
4.6	Possible configurations for the 4-atom window. Note three different geometrically independent window types in the case of 2 Al atoms within this window.	28
6.1	Conventional cubic cell of the $L1_2$ structure and nearest neighbor surroundings of the α - and β -sublattice. Majority A atoms are marked by filled dots, minority B atoms by open circles, respectively. On the α -sublattice an A atom has 8 further A atoms and 4 B atoms as nearest neighbors. An atom of kind B on the β -sublattice is surrounded by 12 A atoms in the first coordination shell	40

6.2	4-atom window between an A atom located on the α -sublattice and a vacancy on the β -sublattice. It is made up of the four common nearest neighbor atoms.	40
6.3	Basic jump types in the L1 ₂ structure: Order-preserving (left) and ordering-disordering jumps (right) with their corresponding jump profiles (in the case of B: $\alpha \rightarrow \alpha$, artificial asymmetry due to limited supercell size was corrected). The energy profiles were calculated <i>ab initio</i> using VASP. See text for details.	42
6.4	The seven geometrically independent window configurations	43
6.5	MC-Time vs. MC-Steps for the CSP (dashed line) and the VSP (solid line) model as obtained by the RTA algorithm at 1200 K. Although the both models differ in slope, both curves show a strictly linear behaviour. . . .	47
6.6	Long range order parameter η versus MC step number for the VSP (full line) and CSP (dashed line) models for the energy parameters adapted to Ni ₃ Al. Annealing temperatures are 1200 K (left) and 1650 K (right). In both cases the initial stage was a system corresponding to perfect order and containing 1 vacancy. Dotted line: final equilibrium value. Note the different scalings.	48
6.7	Fractions of all possible jump types in the the new, improved VSP model as compared to the CSP model at temperatures of 1200 K and 1650 K in initial and equilibrium phases of the kinetics. The corresponding long-range order parameter is 0.96 and 0.76, respectively. In the upper row the first 100,000 jumps of independent runs were analyzed to demonstrate the initial phase of ordering. The bottom row shows the fractions of jump types after the systems have reached their equilibrium states. These statistics are based on 1,000,000 jumps for each independent run. In the initial state, the frequencies of disordering and ordering jumps differ but very slightly. This is however sufficient to generate the overall disordering effect.	49
6.8	Comparison of fractions of all possible window types that are passed by A and B atoms in order-preserving jumps at 1200 K and 1650 K and in different phases of the kinetics (top: initial, bottom: equilibrium).	50
6.9	Comparison of fractions of all possible window types that are passed by A and B atoms in disordering jumps at 1200 K and 1650 K and in different phases of the kinetics (top: initial, bottom: equilibrium).	51
7.1	Definition of the seven geometrically independent window configurations	58
7.2	Relaxation curves of the long range order (LRO) parameter η for two annealing temperatures 1200 K (left) and 1650 K (right). The overall kinetics of the improved VSP (full line) model and the CSP (dashed line) model are compared for the energy parameters adapted to Ni ₃ Al. In both cases the simulation was started in an initial stage of perfect order (containing 1 vacancy) and the system was relaxed towards its equilibrium state, which is shown by the dotted line. Note the different scalings.	60

7.3	Initial phase of the kinetics at temperatures of 1200 K and 1650 K: improved VSP model (black) as compared to the CSP model (grey). The initial phase of ordering corresponds to the first 100,000 jumps of independent runs. a) Distribution of jump types according to Tab. 7.1. b) For order-preserving B: $\beta \rightarrow \alpha$ jumps, statistics of jumps through windows with different configurations according to Fig. 7.1	61
8.1	Face centered cubic Aluminum: convergence of the most important parameters in VASP. On the left the number of k -points in each direction is drawn against the energy per atom at a fixed volume. On the right side the cut-off energy for plane waves is plotted versus the energy/atom. The most reliable energy value corresponding to the highest setting is drawn as a solid line. The area of reliable settings is shown as dashed lines (± 1 meV/atom).	67
8.2	Face centered cubic Nickel (spin polarized): convergence of the most important parameters in VASP. On the left the energy per atom at a fixed volume is drawn against the number of k -point in each direction. On the right side the energy/atom is plotted versus the cut-off energy for plane waves. The most reliable energy value corresponding to the highest setting is drawn as a solid line. The area of reliable settings is shown as dashed lines (± 1 meV/atom).	68
8.3	Energy vs. volume curve for fcc Aluminium and fcc Nickel. All values are per atom. The symbols show the calculated values.	68
8.4	L1 ₂ Ni ₃ Al: convergence of the most important parameters in VASP. On the left the energy per atom at a fixed volume is drawn against the number of k -point in each direction. On the right side the energy/atom is plotted versus the cut-off energy for plane waves. The most reliable energy value corresponding to the highest setting is drawn as a solid line. The area of reliable settings is shown as dashed lines (± 1 meV/atom).	70
8.5	Energy vs. volume curve L1 ₂ Ni ₃ Al. All values are per atom. The symbols show the calculated values.	70
8.6	[010] side view: Residual forces (black arrows) on fixed 'surface' atoms of a 32-atom (left) and 108-atom (right) supercell of L1 ₂ Ni ₃ Al containing an Al vacancy. Aluminum atoms are drawn with larger dots in white (top layer) and grey (lower layers). Nickel atoms are small black (top layer) and grey (lower layers) circles. The dotted line indicates the 'surface' of the supercell.	73
8.7	Local configuration around a Ni vacancy. Here only nearest neighbors are shown.	74
8.8	Relaxation of neighboring ions of a vacancy located on the majority sublattice in %. The values are given with respect to the equilibrium distance of the coordination shell in a perfectly ordered crystal. Two different choices of the size of the supercell are compared: 2x2x2 with 32 lattice sites (crosses) and 3x3x3 with 108 lattice sites (dots). Displacements of Ni and Al atoms are shown by black and blue symbols, respectively.	74

8.9	Local configuration around an Al vacancy. Here only nearest neighbors are shown.	75
8.10	Relaxation of neighboring ions of a vacancy located on the minority sublattice in %. The values are given with respect to the equilibrium distance of the coordination shell in a perfectly ordered crystal. Two different choices of the size of the supercell are compared: 2x2x2 with 32 lattice sites (crosses) and 3x3x3 with 108 lattice sites (dots). Displacements of Ni and Al atoms are shown by black and blue symbols, respectively.	75
8.11	Local configuration around an Ni antisite. Here only nearest neighbors are shown.	76
8.12	Relaxation of neighboring ions of an antisite located on the minority sublattice in %. The values are given with respect to the equilibrium distance of the coordination shell in a perfectly ordered crystal. Two different choices of the size of the supercell are compared: 2x2x2 with 32 lattice sites (crosses) and 3x3x3 with 108 lattice sites (dots). Displacements of Ni and Al atoms are shown by black and blue symbols, respectively.	76
8.13	Local configuration around an Al antisite. Here only nearest neighbors are shown.	77
8.14	Relaxation of neighboring ions of an antisite located on the majority sublattice in %. The values are given with respect to the equilibrium distance of the coordination shell in a perfectly ordered crystal. Two different choices of the size of the supercell are compared: 2x2x2 with 32 lattice sites (crosses) and 3x3x3 with 108 lattice sites (dots). Displacements of Ni and Al atoms are shown by black and blue symbols, respectively.	77
8.15	Local configuration of order-keeping Ni jumps. This environment corresponds to perfect long range order.	84
8.16	Comparison of jump profiles via static displacement along a straight path (dotted) and the NEB method (full circles) for Ni jumps in the L1 ₂ structure with different window configurations (for definitions see Fig. 4.6 in Sec. 4.4). Energy values are in eV.	85
8.17	Local configuration of order-keeping Al jumps. This environment corresponds to the highest possible degree of order.	86
8.18	Comparison of jump profiles via static displacement along a straight path (dotted) and the NEB method (full circles) for order-keeping Al jumps in the L1 ₂ structure with different window configurations (for definitions see Fig. 4.6 in Sec. 4.4). Energy values are in eV.	87
8.19	Local configuration of ordering-disordering Ni jumps. This environment corresponds to perfect long range order.	88
8.20	Comparison of jump profiles via static displacement along a straight path (dotted) and the NEB method (full circles) for ordering-disordering Ni jumps in the L1 ₂ structure with different window configurations (for definitions see Fig. 4.6 in Sec. 4.4). Energy values are in eV.	89
8.21	Local configuration of ordering-disordering Al jumps. This environment corresponds to perfect long range order.	90

8.22	Comparison of jump profiles via static displacement along a straight path (dotted) and the NEB method (full circles) for ordering-disordering Al jumps in the $L1_2$ structure with different window configurations (for definitions see Fig. 4.6 in Sec. 4.4). Energy values are in eV.	91
8.23	Comparison of jump profiles via static displacement along a straight path (dotted) and the NEB method (full circles) for order preserving jumps in the $L1_2$ structure at perfect order. The corresponding jump paths are shown in the lower part of the columns.	92
8.24	The energetics of the three main stages of an elementary jump process and their corresponding atomic configurations: An atom (red) moves from its initial position (1) to the final position (3). The saddle point state (2) is reached as the jumping atom enters the 4-atom window (grey).	94
8.25	Top: Initial configurations of the environment for the ordering-disordering jump $A:\alpha \rightarrow \beta$ for B antisites within the first four coordination shells. Bottom: Change of barrier height with respect to the barrier height of the jump in a perfectly ordered lattice (through a 4-atom window consisting of A atoms only). The dotted line is a guide to the eyes to demonstrate the declining influence of antisites with respect to distance to the jumping atom.	96
8.26	Change of barrier height for B jumps with respect to the barrier height of the jump in a perfectly ordered lattice (through a 4-atom window consisting of A atoms only). The dotted line is a guide to the eyes to demonstrate the declining influence of antisites with respect to distance to the jumping atom.	98

List of Tables

4.1	Neighborhood environment for the first 15 coordination shells in fcc based structures. The relative vector components are shown in units of $2a$ for clarity, where a is the lattice spacing. The distance is in units of a . The total number of neighbors of any species in this coordination shell is also shown.	22
4.2	Order-preserving (left) and ordering-disordering (right) jump types in the $L1_2$ structure. The jumping atom has to cross a 4-atom window of common nearest neighbors. In the bottom lines the point defects present before and after the jump are also shown.	27
6.1	Pure barrier heights for all possible jump types and window configurations (definition: see Fig.6.4) in $L1_2$ Ni_3Al obtained by <i>ab initio</i> calculations. The relative energy values refer to a $2 \times 2 \times 2$ supercell and were obtained by NEB calculation. All values are in eV. Order preserving jumps: A: $\alpha \rightarrow \alpha$, B: $\alpha \rightarrow \alpha$ (left side) Ordering-disordering jumps: A: $\alpha \rightarrow \beta$, B: $\beta \rightarrow \alpha$ (right side)	44
6.2	Obtained fit parameters A , τ_1 and τ_2 for CSP and VSP model.	48
7.1	Order-preserving (left) and ordering-disordering (right) jump types in the $L1_2$ structure and their corresponding energy profiles, calculated <i>ab initio</i> using VASP (see text for details). The jumping atom has to cross a 4-atom window of common nearest neighbors. In the bottom lines the point defects present before and after the jump are also shown, V_α being a vacancy on the α -sublattice, B_α being an antisite B atom on the α -sublattice etc. . .	58
7.2	Pure barrier heights obtained by <i>ab initio</i> calculations for $L1_2$ Ni_3Al . For the definition of all possible jump types and window configurations see Tab. 7.1 and Fig. 7.1. The bold relative energy values refer to a $3 \times 3 \times 3$ supercell whereas values for a $2 \times 2 \times 2$ supercell are also shown for comparison. All values are in eV. Order-preserving jumps: A: $\alpha \rightarrow \alpha$, B: $\alpha \rightarrow \alpha$ (left side) Ordering-disordering jumps: A: $\alpha \rightarrow \beta$, B: $\beta \rightarrow \alpha$ (right side)	59
8.1	Calculated equilibrium values of fcc Al and spinpolarized fcc Ni. The lattice constant a_0 is in \AA , the bulk modulus B in GPa, B' is the pressure derivative of B . The values of E are in eV/atom. Experimental (exp.) and computed (comp.) values are shown for comparison.	69

8.2	Calculated equilibrium values $L1_2$ Ni_3Al . The lattice constant a_0 is in \AA , the bulk modulus B in GPa, B' is the pressure derivative of B . Experimental (exp.) and computed (comp.) values are shown for comparison . . .	71
8.3	Barrier heights ΔE_{is} for order-keeping Ni jumps and selected window configurations calculated with the straight jump path and the Nudged Elastic Band method. Values were calculated <i>ab initio</i> within a $2 \times 2 \times 2$ supercell. All energies are in eV. The position in fractions of the jump path of the saddle point calculated with the NEB method is also shown. For the definition of window configurations see Fig. 4.6 in Sec. 4.4.	84
8.4	Barrier heights ΔE_{is} for order-keeping Al jumps and selected window configurations calculated with the straight jump path and the Nudged Elastic Band method. Values were calculated <i>ab initio</i> within a $2 \times 2 \times 2$ supercell. All energies are in eV. The position in fractions of the jump path of the saddle point calculated with the NEB method is also shown. For the definition of window configurations see Fig. 4.6 in Sec. 4.4.	86
8.5	Barrier heights ΔE_{is} for ordering-disordering Ni jumps and selected window configurations calculated with the straight jump path and the Nudged Elastic Band method. Values were calculated <i>ab initio</i> within a $2 \times 2 \times 2$ supercell. All energies are in eV. The position in fractions of the jump path of the saddle point calculated with the NEB method is also shown. For the definition of window configurations see Fig. 4.6 in Sec. 4.4.	88
8.6	Barrier heights ΔE_{is} for ordering-disordering Al jumps and selected window configurations calculated with the straight jump path and the Nudged Elastic Band method. Values were calculated <i>ab initio</i> within a $2 \times 2 \times 2$ supercell. All energies are in eV. The position in fractions of the jump path of the saddle point calculated with the NEB method is also shown. For the definition of window configurations see Fig. 4.6 in Sec. 4.4.	90
8.7	A jumps (for index see Fig. 8.25). The distance of the Al antisite to the initial position of the jumping atom in units of the lattice spacing a , and all energies are given in eV. The configurations of the last two rows are not shown in Fig. 8.25.	95
8.8	B jumps (for index see Fig. 8.25). The distance of the Al antisite to the initial position of the jumping atom in units of the lattice spacing a , and all energies are given in eV. The configurations of the last two rows are not shown in Fig. 8.25.	97

Chapter 1

Introduction

1.1 General motivation

The desired favorable properties of many alloy materials depend on detailed atomic configuration. Chemical long-range order, for instance, imposes strict conditions on the movement of dislocations in intermetallic compounds, thus improving mechanical strength. Order, by its reduction of crystal symmetry, can also define preferred alignment directions of magnetic momenta allowing increased writing density in storage media and influences electric conductivity, corrosion resistance etc. As one is interested both in the service reliability (stability) and ease of manufacturing of these materials, kinetics of configurational transformations must be understood. Kinetic Monte-Carlo simulation (KMC) has proved to be a valuable tool for this purpose as it is easy to perform and free from additional assumptions, its only input being the probabilities for the jumps of individual atoms. Every effort to improve the determination of the latter will therefore reflect in the validity of the whole method.

1.2 Organization of this work

This thesis is structured as follows. First we give a short introduction into the role of Monte-Carlo simulation (MC) in the field of materials science. Then we deal with common MC methods as found in literature and their respective advantages and problems. We then explain the motivation for the specific topic treated in this thesis. In the next sections, we dwell on such technical details as cannot be discussed in detail within the condensed form of a journal article. The main body of our results is then contained in two published articles which have been included in the text. In a final section these

and additional results are further discussed and a general outlook on future work and prospects is given.

1.3 Overview

In this thesis an improved model for kinetic Monte-Carlo (KMC) simulations of atom configuration in alloys is presented. KMC is a valuable tool to explicitly study development of a system towards an equilibrium state, allowing a detailed study of the atom kinetics at work. In chapter 2 the basics of kinetic Monte-Carlo simulation are shown with a focus on the residence time algorithm (RTA) which was the appropriate choice for my study. This algorithm is suitable to describe vacancy-mediated diffusion in a substitutional solid solution like the test system (Ni_3Al) chosen. In KMC simulation a valid expression for the activation barrier for atom jumps is all-important as it is the only input. It extends from an initial equilibrium position up to a transitional saddle point, both dependent on local environment. However, if one takes a look into the literature little work was done regarding variable saddle points. While some authors (e.g. [1], [2], [3], [4]) set all saddle points to a constant, mostly undefined value, others connect this energy level to the sort of the jumping atom (e.g. see [5], [6], [7]). Some authors (e.g. [8], [9], [10]) try to overcome this obstacle by running molecular dynamics simulations (e.g. with EAM potentials) with the limitation of a shorter timescale. Recognizing the pivotal importance of having reliable and theoretically well-founded values for the individual atom jump rates, the main endeavor was directed towards their calculation.

As the model alloy for my investigations I took the technically important L_{12} -ordered intermetallic compound Ni_3Al possessing special high temperature strength characteristics. In chapter 4 the face centered cubic (fcc) based L_{12} structure is defined and some properties are discussed. An important feature of this structure is that an atom jumping into a nearest-neighbor site has to pass an intervening 4-atom-window consisting of common nearest neighbors of both - the jumping atom and the vacant lattice site.

It was surmised that the specific atom occupancy of this window exerts a decisive influence on the saddle point height and therefore on jump energy barrier and the jump rate according to transition state theory (TST). This is explained and the importance analysed in chapter 8.

It was decided to do an extensive *ab initio* study on jump energy profiles and barriers, dependent on 4-atom window occupancy and variable surroundings in the next nearest neighbor positions. For these calculations based on density functional theory (DFT) the reliable and well established software VASP (Vienna Ab initio Simulation Package) was employed. An introduction to density functional theory and some comments to VASP can be found in chapter 5. The impact of our results on kinetics was studied, both globally and with respect to detailed jump statistics by various KMC simulations based on an self-developed code.

Chapter 2

Kinetic Monte-Carlo Simulations (KMC)

In this chapter the basics of kinetic Monte-Carlo simulations are introduced. The advantage of this approach is that when studying the kinetics of a system only single atom jump probabilities have to be calculated (e.g. see [11]). In the following, after the explanation of a Markov process following the way of [12] the three most important algorithms (Metropolis, Glauber and residence time) for this kind of simulations are introduced.

2.1 The single atom jump as a Markov process

In most intermetallics the elementary diffusion step is the jump of an atom into a nearest-neighbor (NN) vacancy. Considering the vacancy, any of Z nearest-neighbor atoms surrounding it may change places with it. In a system where the atom states are sufficiently thermalized between jumps, the jump probabilities depend only on the present configuration of the system as it is and not on how it was reached by previous jumps. This loss of memory is the hallmark of a Markov process. Let us regard an ensemble of identical systems with a vacancy on a specified lattice site, which we call state α . Exchange of the vacancies with any of the Z NN atoms leads to one of the follow-up states β^j ($j=1,\dots,Z$) (see Fig. 2.1).

Designating by p_α the fraction of systems of the ensemble in state α (and analogously for p_β^j) we have with the jump rate (= jump probability per unit time) $\Gamma_{\alpha\beta}^j$

$$\begin{aligned}\dot{p}_\alpha &= - p_\alpha \sum_{j=1}^Z \Gamma_{\alpha\beta}^j \\ \dot{p}_\beta^j &= p_\alpha \Gamma_{\alpha\beta}^j.\end{aligned}\tag{2.1}$$

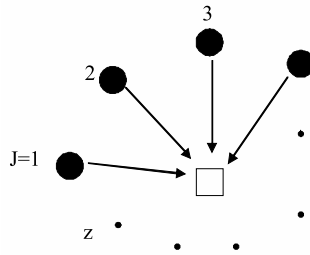


FIGURE 2.1: Schematic picture of the state before the single atom jump: a vacancy (square) is surrounded by Z nearest-neighbor atoms (dots). Each of this atoms may exchange their position with the vacancy. This corresponds to the state α of the system. After the j th atom has jumped into the vacancy the system finally reaches state β^j .

Assuming all systems of the ensemble to be in state α at $t = 0$, this system of equations is solved by

$$\begin{aligned} p_\alpha &= \exp\left(-\sum_j \Gamma_{\alpha\beta^j}^j t\right) \\ p_{\beta^j} &= \frac{\Gamma_{\alpha\beta^j}^j}{\sum_j \Gamma_{\alpha\beta^j}^j} \left[1 - \exp\left(-\sum_j \Gamma_{\alpha\beta^j}^j t\right)\right]. \end{aligned} \quad (2.2)$$

An example of these functions is plotted in Fig. 2.2. It is seen that the probability of the initial state decays exponentially, while the follow-up states approach their final probability distribution with the same time constant, just as it happens in radioactive decay with several decay channels.

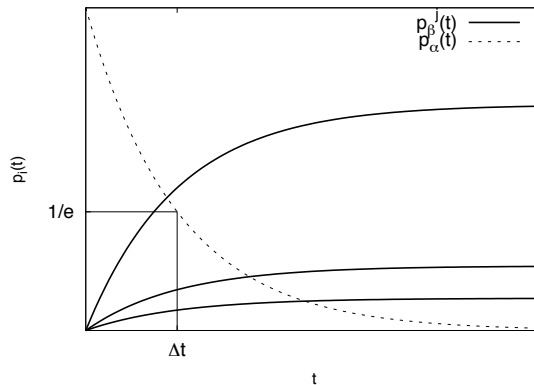


FIGURE 2.2: Atom jumps as a Markov process, time evolution of probabilities (example): initial state α (dashed line) follow-up states β^j (full lines). At the marked coordinates the probability of the initial state has decreased to $1/e$.

The jump frequencies (jump probabilities per unit time) according to transition state theory (see chapter 3.1) always have the form

$$\Gamma_{\alpha\beta}^j = \Gamma_0 \exp\left(-\frac{\Delta E_{\alpha\beta}^j}{k_B T}\right), \quad (2.3)$$

where Γ_0 may be called an attempt frequency and $\Delta E_{\alpha\beta}^j$ is an energy difference which must be supplied by thermal activation. The different Monte-Carlo algorithms commonly used can now be distinguished according to the time at which the equation system in Eq. 2.2 is evaluated.

2.2 Metropolis/Glauber algorithms

The original Metropolis algorithm [16] is obtained if the probabilities in Eq. 2.2 are evaluated at short times $t = \Delta t_{MC} = 1/\Gamma_0$ and a specific successor state $\beta^j = \beta$ is pre-selected by a random variable. The solution of Eq. 2.2 then takes on the very simple form

$$\begin{aligned} p_\alpha &\approx 1 - \exp\left(-\frac{\Delta E_{\alpha\beta}}{k_B T}\right) \approx 1 \\ p_\beta &= 1 - \exp(-\Gamma_{\alpha\beta} t) \approx \exp\left(-\frac{\Delta E_{\alpha\beta}}{k_B T}\right). \end{aligned} \quad (2.4)$$

If $\Delta E_{\alpha\beta} \leq 0$ then p_β is assumed to be equal to one, and the jump to take place anyhow. If $\Delta E_{\alpha\beta} > 0$ it is decided by a second random variable r whether the transition takes place or not. If r is equally distributed in the interval $[0,1]$ the jump takes place if

$$0 \leq r \leq \exp\left(-\frac{\Delta E_{\alpha\beta}}{k_B T}\right).$$

The obvious disadvantage of the Metropolis algorithm is a possibly large number of futile jump attempts if $\Delta E_{\alpha\beta}/k_B T \gg 1$. The formulation of the probabilities as in Eq. 2.4 has been perceived as unsatisfactory as they do not add up to one. After the introduction of a renormalizing factor the probabilities are known as those of the Glauber algorithm [17]

$$p_\beta = \begin{cases} \frac{1}{1 + \exp\left(-\frac{1}{k_B T} \Delta E_{\alpha\beta}\right)} & \text{if } \Delta E_{\alpha\beta} \leq 0 \\ \frac{\exp\left(-\frac{1}{k_B T} \Delta E_{\alpha\beta}\right)}{1 + \exp\left(-\frac{1}{k_B T} \Delta E_{\alpha\beta}\right)} & \text{else.} \end{cases} \quad (2.5)$$

2.3 Residence time algorithm (RTA)

If, in contrast to the Metropolis/Glauber variant of kinetic Monte-Carlo simulation, the time is chosen long enough so that the probability for the system to remain in its initial state has decreased significantly, then at each Monte-Carlo step a jump can be expected. With $p_\alpha(\Delta t) = (1/e) p_\alpha(0)$ the time interval one has to wait for a jump is given by

$$\Delta t = \frac{1}{\sum_{i=1}^Z \Gamma_{\alpha\beta}^i}. \quad (2.6)$$

(Also compare Fig. 2.2). This is the so called residence time algorithm (RTA)[13], [14], [15].

As can easily be shown this time interval also corresponds to the average decay time $\langle t \rangle$ of the initial state α .

As the time intervals Δt so calculated vary in the course of the simulation one has to keep a log of them. If they shall finally be translated into physical time it is necessary (although by no means easy) to make reasonable assumptions about the attempt frequency Γ_0 . Setting $\Gamma_0=1$ is tantamount to choosing arbitrary time units, which may be sufficient if only relative variations in the kinetic behavior are to be studied.¹

The long-time probability $p_{\alpha\beta}^j(t = \infty)$ for a nn atom j to jump into the vacant lattice site follows from Eq. 2.2 as

$$p_{\alpha\beta}^j = \frac{\Gamma_{\alpha\beta}^j}{\sum_{i=1}^Z \Gamma_{\alpha\beta}^i}. \quad (2.7)$$

Having determined the average decay time, the jump channel (the follow-up state) is selected according to the probability distribution in Eq. 2.7 by an equally distributed random number $r \in [0,1]$. Jump channel j is chosen if

$$\sum_{k=1}^j p_{\alpha\beta}^k < r \leq \sum_{k=j}^{j+1} p_{\alpha\beta}^k.$$

In the RTA transition probabilities to all of the Z follow-up states have to be calculated. Therefore the algorithm is effective only if Z is not too large, a condition which is fulfilled for the vacancy mechanism and nearest-neighbor jumps. The advantage of the RTA is that in each MC time interval a jump does take place.

¹In a conceptually even more pure variant of the algorithm not an average decay time of the initial state is used but the decay times are chosen individually according to the probability distribution given by p_α by means of another random variable. The results however do not seem to justify the extra effort.

A requirement which is usually invoked is that the thermodynamic equilibrium state shall also correspond to a dynamic equilibrium of jumps in configuration space. This principle is known as detailed balance. Denoting the occupancy of state α in equilibrium with f_α etc., we have

$$f_\alpha \Gamma_{\alpha\beta} = f_\beta \Gamma_{\beta\alpha}. \quad (2.8)$$

If the equilibrium corresponds to a canonical ensemble, and if we can take for granted that the attempt frequencies for the jump and its reverse are equal, it follows that

$$\frac{f_\alpha}{f_\beta} = \exp \left[-\frac{1}{k_B T} (E_\beta - E_\alpha) \right] = \frac{\Gamma_{\beta\alpha}}{\Gamma_{\alpha\beta}}. \quad (2.9)$$

We note that the principle of detailed balance is indeed obeyed by the RTA (as is the case with the Glauber/Metropolis algorithm) although the form of the probabilities in Eq. 2.7 together with Eq. 2.3 seems to point to the contrary. But in detailed balance the *rates* and not the jump *probabilities* from both sides of a transition are set in relation. The rates are obtained by dividing the jump probabilities by the (variable) time interval Δt defined in Eq. 2.6, which just cancels out the denominator in Eq. 2.7.

Chapter 3

The single atom jump

In this chapter the single atom jump is discussed in terms of the famous transition state theory, following ref. [18]. For a more detailed treatment of this topic the reader might refer to this review and references therein.

In the second part of this chapter the Nudged Elastic Band method for calculating saddle point energies needed for transition rates is introduced.

3.1 Transition State Theory

The transition state theory (TST) [19] is a valuable method to estimate rates of transitions within a system when dealing with rare events or slow transitions. In other words by invoking TST it is possible to calculate transition rates for most diffusion events in intermetallics.

Let us have a look at a system (crystal) consisting of N atoms and having therefore $6N$ degrees of freedom (coordinates \vec{x}_i and momenta \vec{p}_i). A potential Φ of the total internal energy of the crystal can generally be written as a function of these degrees of freedom $\Phi \rightarrow \Phi(\vec{x}_1, \dots, \vec{x}_N; \vec{p}_1, \dots, \vec{p}_N)$.

In a classical system we can assume the momenta and the coordinates to be distributed independently of each other and treat the potential Φ as a function of the coordinates only leaving $3N$ degrees of freedom $\Phi \rightarrow \Phi(\vec{x}_1, \dots, \vec{x}_N)$. A principle sketch of such an energy landscape in configuration space is shown in Fig. 3.1.

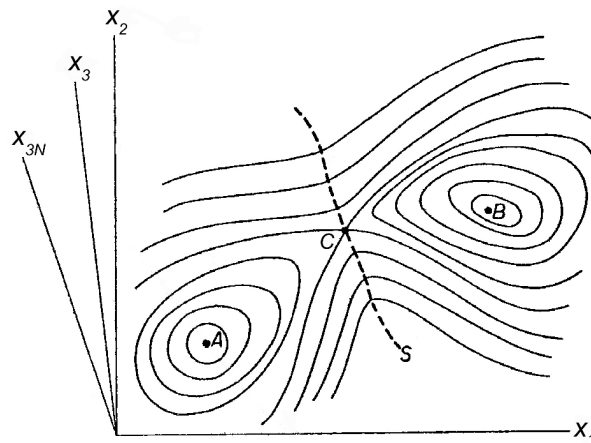


FIGURE 3.1: Energy landscape of a jump process. From: [18]

After the definition of our potential we want to describe a single atom jump within this energy landscape. An atom is located at its initial equilibrium position (basin A in Fig. 3.1). To shift its position to a new equilibrium position (basin B) this atom has to surmount an energy barrier (point C) lying between these two local minima of internal energy. The local energy maximum at the transition state topologically defines a saddle point. In order to take the atom over it, energy fluctuations (vibrations) are needed. Therefore we call this event a thermally activated process.

We can describe this situation invoking the transition state theory based on two main assumptions:

- We require that the states of the system can be thermalized sufficiently between two successive jumps of the atom and are therefore distributed according to a canonical ensemble up to the saddle point.
- Once the atom (system) has reached the saddle point and has a positive velocity in the direction of the new site, it will definitely end up there. This means that the curvature of the energy surface at the saddle point should not be too weak.

Then the transition rate can be calculated by the average number of systems crossing the saddle point in a time unit divided by the number of systems in A.

From these assumptions it follows that the transition rate Γ_{ij} (see [18])

$$\Gamma_{ij} = \Gamma_0 \exp \left[-\frac{(E_s - E_i)}{k_B T} \right], \quad (3.1)$$

where Γ_0 is a quotient of normal frequencies in the original equilibrium state and the saddle point, and E_s , E_i are the (free) energies of the saddle point state and initial equilibrium state, respectively.

Drawbacks of the TST

The two basic assumptions of the transition state theory are usually fulfilled in strongly bound metals at not too high temperatures. In this thesis, especially when dealing with intermetallics like Ni₃Al the TST is considered to be valid and appropriate. However, for completeness other approaches should be mentioned:

- **Diffusion theory of thermal activation.**

The diffusion theory of thermal activation [20], [21], [22] is more appropriate if the temperature is elevated and the curvature of the potential in the saddle point state is small. The reason is that then a reversal of the system motion at or near the saddle point is possible. In diffusion theory of thermal activation a steady-state flow of representative system points over the saddle point can then be derived in analogy with classical nucleation theory. This leads to a reduced attempt frequency as compared to transition state theory .

- **Dynamical theories.**

According to the first criterion in the transition state theory the states up to the saddle point state are thermalized and follow a canonical distribution. If one argues that a jumping atom does not stay long enough at the saddle point to reach the equilibrium, a dynamical theory of thermal activation, based on lattice dynamics has to be constructed (see e.g. [23], [24], [25]).

- **Molecular dynamics.**

The big alternative to Kinetic Monte-Carlo simulations based on the transition state theory is Molecular dynamics. In Molecular dynamics one solves the equation of motion of all atoms involved, including the jumping atom. This enables to take into account inertial and cooperative effects. To do this, reliable potentials have to be constructed to treat the interactions. One of the most prominent models for a potential is the so called (embedded-atom method) EAM. Nevertheless, Molecular dynamics can only be used on short time scales (pico-seconds) and potentials often have the flavour of arbitrariness, being based on patchy semi-empirical adaptations.

3.2 The Nudged Elastic Band (NEB) method

We saw in section 3.1 that a crystal can be described by a potential function in a 3N dimensional configuration space. Furthermore it was shown that an exchange of position of an atom with a vacancy leads from one equilibrium state of configuration and energy to another. To reach the new equilibrium state the system (in our case the jumping atom) has to pass a saddle point state located between initial and final state. According to transition state theory a transition rate (Eq. 3.1) can be calculated when explicit energies of both, the initial and the saddle point state are known.

As we will see in chapter 5.1 the calculation of equilibrium energies (initial and final states) can be reliably done by using state-of-the-art methods like *ab initio* calculations. On the other hand it is not a trivial task to find the optimum path corresponding to lowest activation energy in the migrational process. Therefore *ab initio* software packages like VASP offer the so called Nudged Elastic Band (NEB) [26] [27] method to optimize this path computationally.

This introduction of the NEB method is following the concept of Jonsson, Mills and Jacobson in [28]. The interested reader is referred to this article and references therein.

In the Nudged Elastic Band method a chain of images between two defined states of the system (initial and final equilibrium) is considered. These images can be regarded as replicas of the system as it follows the transition path of a jump along the potential energy surface $V(\vec{R})$.

They are connected with springs with a spring constant k in an additional dimension in the phase space. This elastically bound chain of states is now relaxed towards an optimized jump path that minimizes the energy necessary to do the transition (minimum energy path).

In detail, this is done as follows. After the definition of initial replicas as a first guess, for instance by linear interpolation, the force \vec{F}_i acting on image i , i.e.

$$\vec{F}_i = -\vec{\nabla}V(\vec{R}_i) + \vec{F}_i^{spring} \quad (3.2)$$

is calculated. Here the term \vec{F}_i^{spring} is the spring force acting on the image, i.e.

$$\vec{F}_i^{spring} = k_{i+1}(\vec{R}_{i+1} - \vec{R}_i) - k_i(\vec{R}_i - \vec{R}_{i-1}). \quad (3.3)$$

These forces are minimized by relaxing all the images simultaneously at each relaxation step. This minimization could be carried out in several ways. In the NEB method a 'nudging' is introduced. This means a projection of the perpendicular component of $\vec{\nabla}V(\vec{R}_i) \Rightarrow \vec{\nabla}V(\vec{R}_i)|_{\perp}$ and the parallel components of the spring force, i.e.

$$\vec{F}_i^0 = -\vec{\nabla}V(\vec{R}_i)|_{\perp} + (\vec{F}_i^{spring} \cdot \vec{\tau}_{\parallel})\vec{\tau}_{\parallel}. \quad (3.4)$$

$\vec{\tau}_{\parallel}$ is the unit tangent vector parallel to the path and

$$\vec{\nabla}V(\vec{R}_i)|_{\perp} = \vec{\nabla}V(\vec{R}_i) - (\vec{\nabla}V(\vec{R}_i) \cdot \vec{\tau}_{\parallel})\vec{\tau}_{\parallel}. \quad (3.5)$$

When the perpendicular components $\vec{\nabla}V(\vec{R}_i)|_{\perp}$ for each image i vanish all images lie on the minimum energy path.

Chapter 4

The $L1_2$ structure

4.1 General remarks

A lot of technically interesting binary alloys (e.g. Cu_3Au , Ni_3Al , Ni_3Ga , Fe_3Pt , ...) with a stoichiometric composition of A_3B crystallize in the $L1_2$ structure (Fig. 4.1). This structure (also called γ') is based on an underlying face centered cubic lattice (fcc, γ). In the $L1_2$ structure the minority B atoms are located at the cube corners while the majority A atoms are sitting on the face centers. As all four positions (one cube corner and three face centers per unit cell) are geometrically equivalent the numerical relation of A and B atoms is 3:1. The Pearson symbol for this structure is $cP4$. The symmetry of this structure allows 48 space group operations ($\text{Pm}\bar{3}\text{m}$) corresponding to the fcc lattice.

In the following sections symmetry properties of this structure are discussed. First the conventional and the primitive unit cell for the $L1_2$ lattice are introduced. After a discussion of possible divisions into sublattices the definition of the long range order parameter (LRO, η) connected to this structure is introduced. Furthermore important geometric facts are discussed, especially neighbor environments, pair correlation numbers and the 4-atom window between two nearest neighbor sites.

4.2 Properties of the L1₂ structure

4.2.1 Conventional and primitive unit cell

A lattice cell of the L1₂ structure is usually chosen with the minority (B) atoms located at the cube corners and the majority (A) atoms at the face centers of a simple cubic unit cell (see Fig. 4.1).

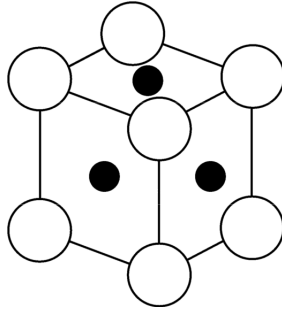


FIGURE 4.1: Left: Conventional cubic cell of the L1₂ structure. B atoms (white) are located on the cube corners and A atoms (black) on the face centers.

This choice is also known as conventional unit cell with primitive (simple cubic) lattice vectors $\vec{A}_1, \vec{A}_2, \vec{A}_3$:

$$\begin{aligned}\vec{A}_1 &= a\vec{e}_x \\ \vec{A}_2 &= a\vec{e}_y \\ \vec{A}_3 &= a\vec{e}_z,\end{aligned}\tag{4.1}$$

where a is the lattice spacing and \vec{e}_i are the cartesian unit vectors. The positions $\vec{B}_1, \vec{B}_2, \vec{B}_3, \vec{B}_4$ of the atoms with respect to the lattice vector in Eq. 4.1 - also called the basis - are then given by

$$\begin{aligned}\vec{B}_1 &= 0 \\ \vec{B}_2 &= \frac{1}{2}\vec{A}_2 + \frac{1}{2}\vec{A}_3 = a\left(\frac{1}{2}\vec{e}_y + \frac{1}{2}\vec{e}_z\right) \\ \vec{B}_3 &= \frac{1}{2}\vec{A}_1 + \frac{1}{2}\vec{A}_3 = a\left(\frac{1}{2}\vec{e}_x + \frac{1}{2}\vec{e}_z\right) \\ \vec{B}_4 &= \frac{1}{2}\vec{A}_1 + \frac{1}{2}\vec{A}_2 = a\left(\frac{1}{2}\vec{e}_x + \frac{1}{2}\vec{e}_y\right)\end{aligned}\tag{4.2}$$

This commonly used choice of unit cell has the advantage of conserving the symmetry of the underlying cubic lattice. Beside the advantage of orthogonality of lattice vectors it offers a convenient way to define domains and corresponding order parameters (see Sec. 4.2.2).

However, the conventional unit cell is not the smallest possible choice of a unit cell. Every structure based on the face centered cubic lattice can also be described by its primitive vectors

$$\begin{aligned} \vec{A}_1^p &= \frac{a}{2} (\vec{e}_y + \vec{e}_z) \\ \vec{A}_2^p &= \frac{a}{2} (\vec{e}_x + \vec{e}_z) \\ \vec{A}_3^p &= \frac{a}{2} (\vec{e}_x + \vec{e}_y) \end{aligned} \quad (4.3)$$

again with the lattice spacing a and the cartesian unit vectors \vec{e}_i . This choice of unit cell contains only 1 atom in contrast to Eq. 4.2 where 4 atoms lie within the smallest cell.

$$\vec{B}_1^p = 0 \quad (4.4)$$

The coordinates of each point P described by one of these two possibilities (Eq. 4.1 and Eq.4.3) $P_{[conv]}$, $P_{[prim]}$ ¹ can be linearly transformed with multiplication by the matrix T or its inverse T^{-1} to the corresponding alternative description by

$$P_{[conv]} = P_{[prim]} \cdot T^{-1} \quad \text{and} \quad P_{[prim]} = P_{[conv]} \cdot T, \quad (4.5)$$

where

$$T = \begin{pmatrix} 1 & 1 & -1 \\ -1 & 1 & 1 \\ 1 & -1 & 1 \end{pmatrix}, \quad T^{-1} = \frac{1}{2} \begin{pmatrix} 1 & 0 & 1 \\ 1 & 1 & 0 \\ 0 & 1 & 1 \end{pmatrix} \quad (4.6)$$

¹The squared brackets indicate the chosen basis set for the coordinates of one specific point in the lattice.

4.2.2 Division into sublattices and long range order parameter

According to the basis vectors defined in Eq. 4.2 the lattice of the L1₂ structure can be separated into 4 equivalent simple cubic sublattices. This division leads to the fact that within a crystal based on this lattice, 4 domains (defined by the location of B atoms) are possible according to which sublattice bears the B atoms.

The other possibility of dividing this structure into sublattices is based on the difference between cube corners and face centers. This leads to:

- The majority (α -) sublattice containing 3/4 of all lattice sites
- The minority (β -) sublattice containing 1/4 of all lattice sites

containing the A and B atoms respectively.

This choice points out the following geometric fact. Depending on which sublattice an atom sits different nearest neighborhood configurations have to be distinguished (Fig. 4.2 left and right). An A atom (α -sublattice) has a neighborhood in the first coordination shell of 8 A atoms and 4 B atoms. In contrast to this a B atom (β -sublattice) is surrounded by A (α) atoms only. This fact will play an important role with the environment dependent saddle point heights in atomic diffusion as discussed later.

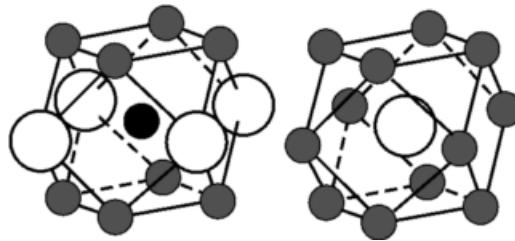


FIGURE 4.2: Nearest neighbor environments of the α - (left) and β -sublattice (right) for the state of perfect order. On the α -sublattice A atoms (black) have 8 further A atoms and 4 B atoms as nearest neighbors. On the β -sublattice a B atom (white) is surrounded by 12 A atoms in the first coordination shell.

Now we can define the long range order parameter. Let us regard a structure built by 2 atomic species A and B. When this structure contains N_A A atoms and N_B B atoms the overall number of atoms is then given by

$$N = N_A + N_B$$

with the concentrations c_A and c_B , where

$$c_A = \frac{N_A}{N} \quad \text{and} \quad c_B = \frac{N_B}{N}$$

and with the constraint

$$c_A + c_B = \frac{N_A + N_B}{N} = \frac{N}{N} = 1$$

If the structure is an ordered structure then it can be divided into sublattices. We define $f_{A\alpha}$ as the fraction of the $N_{A\alpha}$ A atoms located on the sublattice α with respect to the overall number of A atoms N_A . The analogous definition is used for the fraction $f_{B\beta}$ of B atoms sitting on the sublattice β .

$$f_{A\alpha} = \frac{N_{A\alpha}}{N_A} \quad \text{bzw.} \quad f_{B\beta} = \frac{N_{B\beta}}{N_B}$$

We now define the long range order parameter η

$$\eta = \frac{f_{A\alpha} - c_A}{1 - c_A} = \frac{f_{B\beta} - c_B}{1 - c_B}, \quad (4.7)$$

This definition ensures that the value of η lies between -1 and +1. Two special cases should be mentioned. Let us regard B atoms. Only in the state of perfect order all B atoms are located on the β -sublattice ($N_{B\beta} = N_B$). This leads to a corresponding long range order parameter of

$$\frac{\frac{N_B - c_B}{N_B}}{1 - c_B} = \frac{1 - c_B}{1 - c_B} = 1.$$

On the other hand in a randomly ordered state the number of B atoms located on the β -sublattice corresponds the concentration ($f_{B\beta} = c_B$) therefore leading to an η of

$$\frac{c_B - c_B}{1 - c_B} = 0.$$

4.2.3 Pair correlation numbers

In a face centered cubic lattice each lattice site is surrounded by 12 nearest neighbors and 6 next nearest neighbor sites. The further coordination numbers together with their distance relative to the coordinates of the lattice site in question can be found in Tab. 4.1.

From this table an interesting fact can be seen. Starting from the 9th coordination shell relative vectors occur that have the same distance to the site but refer to another plane and a different symmetry. As mentioned in Sec. 4.2.2 and shown in Fig. 4.2 for the L1₂ structure there are different atomic environments depending on which sublattice this site is located.

Coordination number	relative Vector	distance	# neighbors (any species)
Z ₁	(1,1,0)	$\frac{\sqrt{2}}{2}$	12
Z ₂	(2,0,0)	1	6
Z ₃	(2,1,1)	$\frac{\sqrt{6}}{2}$	24
Z ₄	(2,2,0)	$\frac{\sqrt{8}}{2}$	12
Z ₅	(3,1,0)	$\frac{\sqrt{10}}{2}$	24
Z ₆	(2,2,2)	$\frac{\sqrt{12}}{2}$	8
Z ₇	(3,2,1)	$\frac{\sqrt{14}}{2}$	48
Z ₈	(4,0,0)	$\frac{\sqrt{16}}{2}$	6
Z _{9a}	(4,1,1)	$\frac{\sqrt{18}}{2}$	24
Z _{9b}	(3,3,0)	$\frac{\sqrt{18}}{2}$	12
Z ₁₀	(4,2,0)	$\frac{\sqrt{20}}{2}$	24
Z ₁₁	(3,3,2)	$\frac{\sqrt{22}}{2}$	24
Z ₁₂	(4,2,2)	$\frac{\sqrt{24}}{2}$	24
Z _{13a}	(4,3,1)	$\frac{\sqrt{26}}{2}$	48
Z _{13b}	(5,0,1)	$\frac{\sqrt{26}}{2}$	24

TABLE 4.1: Neighborhood environment for the first 15 coordination shells in fcc based structures. The relative vector components are shown in units of 2a for clarity, where a is the lattice spacing. The distance is in units of a. The total number of neighbors of any species in this coordination shell is also shown.

4.2.4 Point defects in the L1₂ structure

There are two main contributions to equilibrium free energy (entropy) of a non-magnetic compound at a given temperature. The first one is vibrational modes (vibrational entropy) and electronic excitations (electronic entropy) and they generally play an important role at high temperatures close to the Curie temperature. The other one, more important at not too high elevated temperatures, is the creation of point defects which directly leads to a change in the chemical order of the compound and therefore to an increase of the configurational entropy.

In an L1₂ ordered compound four types of point defects relevant to order occur (Fig. 4.3):

- vacancies (V_α , V_β) and
- antisite atoms (B_α , A_β)

These defects can be located on both sublattices, designated by α and β . For completeness it should be mentioned that it can also be the case that atoms are located on interstitial sites. These sites are not part of the underlying lattice. In this work we do not consider interstitials because in a substitutional solid solution like Ni₃Al their concentration is negligible.

While antisite defects lead to a decrease in the degree of order the vacancies act as the main mechanism of diffusion. Vacant lattice sites allow neighboring atoms to change their position, whereby antisite defects can be generated. This exchange of position is just what we call 'a single atom jump'. The energetics of it were discussed in detail in chapter 3.

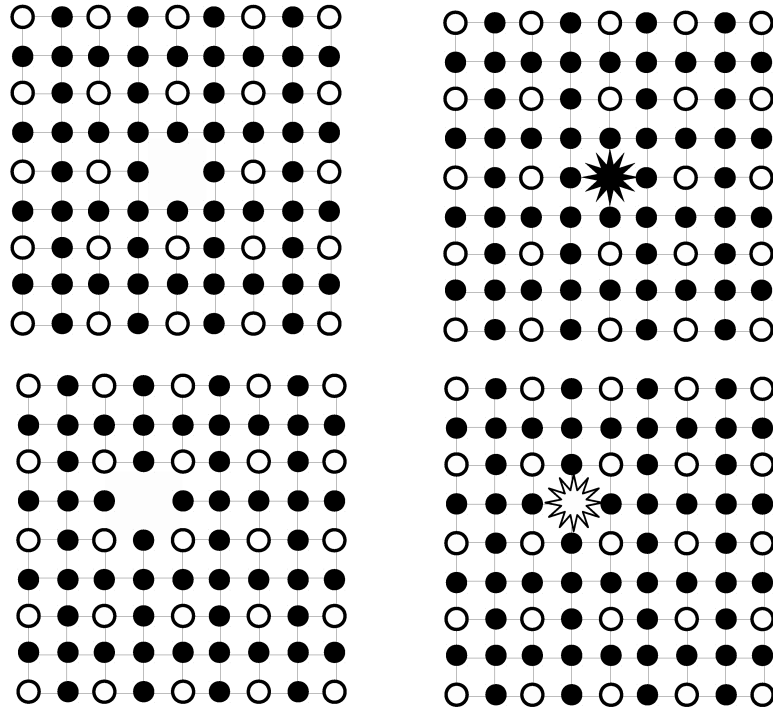


FIGURE 4.3: Possible point defects (vacancies - left and antisites - right) in the $L1_2$ structure on the minority (top) and majority (bottom) sublattice.

4.3 The 4-atom window in the L₁₂ structure

A further geometric fact of the L₁₂ structure which will play an essential role in the configurational dependence of the saddle point height in atomic diffusion is the 4-atom window between two nearest neighbor lattice sites. A detailed discussion of this fact is given in the following sections.

Let us regard an atom on an arbitrary lattice site and one of its nearest neighbor atoms on a face centered cubic lattice. When connecting these 2 lattice positions with a line, it has to pass through a window-like rectangular configuration of 4 common nearest neighbor atoms to both lattice sites (Fig. 4.4).

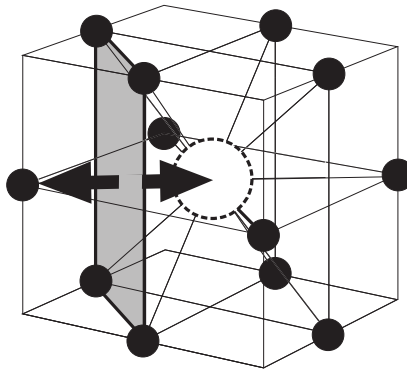


FIGURE 4.4: 4-atom window between an A atom located on the α -sublattice and a vacancy on the β -sublattice. It is made up of the four common nearest neighbor atoms.

Whereas in pure metals the configuration of this window is (apart from double vacancies) obviously always the same, in a two component alloy it can assume a set of different configurations, with probabilities depending on the degree of order and the composition.

In fcc based ordered intermetallics like (L₁₂, L₁₀, ...) the specific configuration of this window strongly depends on the degree of order and on the sublattices the two atoms in question are located on (see Fig.4.5). Therefore we have to distinguish the following 2 basic types of the 4-atom window in the case of perfectly ordered L₁₂:

- **4-atom window which consists only of A atoms:**

This window consisting only of majority atoms occurs in the case of connecting

lattice sites located on the minority and majority sublattices. See Fig. 4.5 (a) and (b) right.

- **4-atom window which consists of 2 A atoms and 2 B atoms:**

This window can be found if one connects two lattice sites of the majority sublattice. See Fig. 4.5 (b) left.

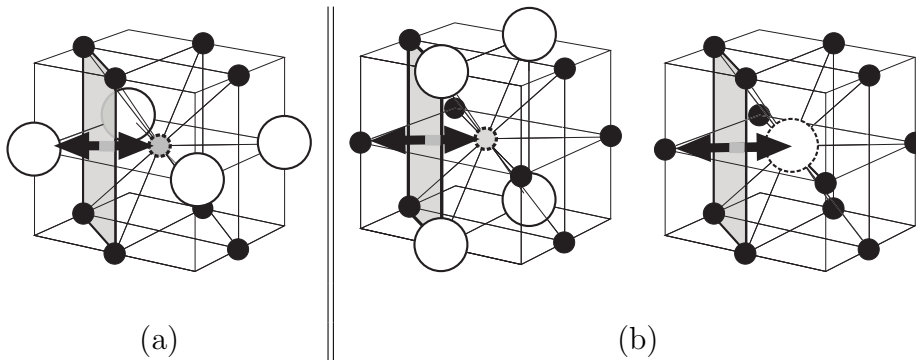


FIGURE 4.5: 4-atom window between 2 lattice positions in the L₁₂ structure for (a): B atoms and (b): A atoms and a neighboring vacancy. Note that in the case of an A atom the explicit configuration of the window depends on the sublattice of the neighboring vacant lattice site.

4.4 Classification of jumps and window types

4.4.1 Classification of jump types in the L1₂ structure

Classifying possible atom jumps, first we have to distinguish between ordering-disordering and order-preserving jumps. In ordering-disordering jumps the jumping atom and the vacancy are located on different sublattices. A jump of this kind leads to a change in the degree of order. In contrast to this we talk about an order-preserving jump if both are located on the same sublattice. In this case the degree of order remains the same after the jump has taken place.

We note that in the L1₂ structure, this is possible only on the majority α sublattice. The second distinction regards the jumping atom. This leads to four possible jump types which can be found in Table 4.2. In this table also the point defects before and after the jump are shown.

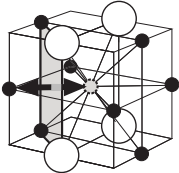
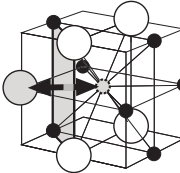
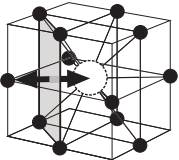
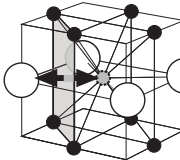
	order-preserving		ordering-disordering	
				
	A: $\alpha \rightarrow \alpha$	B: $\alpha \rightarrow \alpha$	A: $\alpha \rightarrow \beta$	B: $\beta \rightarrow \alpha$
defects before	V_α	V_α, B_α	V_β	V_α
defects after	V_α	V_α, B_α	V_α, A_β	V_β, B_α

TABLE 4.2: Order-preserving (left) and ordering-disordering (right) jump types in the L1₂ structure. The jumping atom has to cross a 4-atom window of common nearest neighbors. In the bottom lines the point defects present before and after the jump are also shown.

4.4.2 Classification of window types

After the definition of the four possible jump types in the L1₂ structure a classification of all possible configurations of 4-atom windows is given in Fig. 4.6. The easiest and obvious way to do this is according to the number of B atoms contained within the window. Note that we now drop the assumption of a perfectly ordered lattice.

Since the shape of the 4-atom window is rectangular with the length of lattice spacing a along the long side and $a/\sqrt{2}$ along the short side, three different geometrically independent configurations for the case of a window containing two B atoms have to be distinguished. All other configurations are symmetrically equivalent to those displayed.

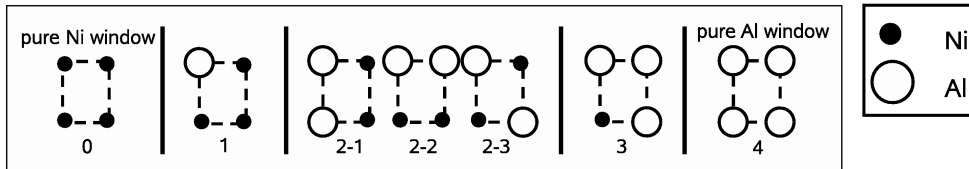


FIGURE 4.6: Possible configurations for the 4-atom window. Note three different geometrically independent window types in the case of 2 Al atoms within this window.

Chapter 5

Density Functional Theory

5.1 General remarks

The focus of this thesis lies on describing and studying the kinetics of an alloy starting from the most basic step possible - the single atom jump. In section 3 it is shown that a jump can be described by three important stages and their corresponding energies: initial, final and saddle point state.

According to transition state theory 3.1 we can calculate transition rates by the knowledge of the difference in energy of initial state and saddle point (Eqn. 3.1). Once we know transition rates we can use kinetic Monte-Carlo simulations (see section 2) to study the kinetics of a system.

How can we calculate the energy differences for different atomic configurations around the jumping atom in practice? For sure this is not possible from experimental data on order kinetics (for example resistivity measurements) as this data is always an average over a multitude of individual single atom jumps. Therefore insights into the energetics on single jumps are not possible from this data.

The presently best available method to obtain binding energies in the solid state is quantum-mechanical calculation from first principles (*ab initio*) based on density functional theory (DFT). We have decided therefore to employ it for our energy profile calculations.

In this chapter a concise overview of the basics of density functional theory is given. For a more detailed description the reader may refer to various books (e.g. [29], [30]). Starting from the many-body Schrödinger equation which cannot be solved with reasonable effort the general way to numerically solve it for total energies of ground states of systems is shown.

5.2 The many-body Schrödinger equation

We consider a system containing $i=1,\dots,N_e$ electrons in the field of $j=1,\dots,N_n$ ions. The electrons with mass m_e carry an electronic charge $-e$ and their coordinates $\vec{X}_i(\vec{r}_i, s_i)$ depend on positions \vec{r}_i and spins s_i . The nuclei have charges $Z_j \cdot e$ and masses M_j depending on the atom type. Their coordinates \vec{R}_j only depend on their positions. For this (non-relativistic) system we can write its time-independent Schrödinger equation, i.e

$$\hat{H}\Psi = E\Psi, \quad (5.1)$$

with wave function

$$\Psi = \Psi \left(\vec{X}_1, \dots, \vec{X}_{N_e}, \vec{R}_1, \dots, \vec{R}_{N_n} \right), \quad (5.2)$$

The Hamilton operator \hat{H} for this case is

$$\hat{H} = \hat{T}_e + \hat{T}_n + \hat{V}_{ee} + \hat{V}_{nn} + \hat{V}_{ne} \quad (5.3)$$

containing kinetic energies T_e , T_n of electrons and ions and all possible interactions V_{ee} , V_{nn} and V_{ne} .

The contributions are defined as (with $e=m_e=\hbar=1$)

- electronic kinetic energy T_e

$$\hat{T}_e = -\frac{1}{2} \sum_{i=1}^{N_e} \nabla_i^2, \quad (5.4)$$

- ionic kinetic energy T_n

$$\hat{T}_n = -\frac{1}{2} \sum_{j=1}^{N_n} \frac{\vec{\nabla}_j^2}{M_j}, \quad (5.5)$$

- electron-electron interaction V_{ee} (with $r_{ik} = |\vec{r}_k - \vec{r}_i|$)

$$\hat{V}_{ee} = \sum_{i < k}^{N_e} \frac{1}{r_{ik}}, \quad (5.6)$$

- nucleus-nucleus interaction V_{nn} (with $R_{jl} = |\vec{R}_l - \vec{R}_j|$)

$$\hat{V}_{nn} = \sum_{j < l}^{N_n} \frac{Z_j Z_l}{R_{jl}}, \quad (5.7)$$

- electron-nucleus interaction V_{ne} (with $r_{ij} = |\vec{R}_j - \vec{r}_i|$) - 'external potential'

$$\hat{V}_{ne} = - \sum_{i=1}^{N_e} \sum_{j=1}^{N_n} \frac{Z_j}{r_{ij}}. \quad (5.8)$$

After introducing suitable boundary conditions the energy eigenvalue spectrum is E_a with an lower limit E_0 , the so called ground state energy and its corresponding ground state wavefunction Ψ_0 . All wavefunctions (eigenstates) Ψ_a can be normalized:

$$\langle \Psi_i | \Psi_j \rangle = \delta_{ij}. \quad (5.9)$$

Furthermore, to obey the fermionic nature of electrons these states have to be antisymmetric with respect to exchange, i.e.

$$\Psi(\vec{X}_1, \dots, \vec{X}_i, \dots, \vec{X}_j, \dots, \vec{X}_{N_e}) = -\Psi(\vec{X}_1, \dots, \vec{X}_j, \dots, \vec{X}_i, \dots, \vec{X}_{N_e}). \quad (5.10)$$

If we further assume the Born-Oppenheimer approximation, the nucleus-nucleus interactions V_{nn} and the motion of the nuclei are separated from the Hamiltonian in Eq. 5.3. In order to obtain the total ground state energy $E_{0,tot}$ of the system V_{nn} has to be added explicitly, i.e.

$$E_{0,tot} = E_0 + V_{nn}. \quad (5.11)$$

The total energy can be understood as a functional of Ψ ,

$$E[\Psi] = \frac{\langle \Psi | \hat{H} | \Psi \rangle}{\langle \Psi | \Psi \rangle} \quad (5.12)$$

and it reaches its minimum for

$$E_0 = \min_{\Psi \rightarrow \Psi_0} E[\Psi]. \quad (5.13)$$

5.3 Density Functional Theory

A system of N_e electrons in its ground state has a one-particle density ρ_0 of

$$\rho_0(\vec{X}) = \int \Psi_0^*(\vec{X}, \vec{X}_2, \dots, \vec{X}_{N_e}) \Psi_0(\vec{X}, \vec{X}_2, \dots, \vec{X}_{N_e}) d\vec{X}_2 \dots d\vec{X}_{N_e} = |\Psi_0(\vec{X})|^2 \quad (5.14)$$

connected to its ground state Ψ_0 . Integrating the density over the space and spins leads to the number of electrons

$$\int \rho_0(\vec{X}) d\vec{X} = N_e, \quad (5.15)$$

which is conserved in a non-relativistic case. In the original concept of Hohenberg and Kohn [31] the energy functional and its minimization in Eq. 5.12 is replaced via Eq. 5.14 to

$$E_0 = E[\rho_0] = \min_{\rho} E[\rho]. \quad (5.16)$$

In other words instead of being a functional of wavefunctions, E_0 is now formulated as an energy functional of the density. The Hohenberg-Kohn theorem is an exact reformulation (under certain conditions) of the many-body Schrödinger equation invoking the density as a function of four variables only. This formulation is an improvement since the wavefunctions are dependent on $4N_e$ variables.

For practical implementation Kohn and Sham [32] introduced a more feasible concept employing single particle like wavefunctions ('orbitals') ϕ that build up the exact ground state density in Eq. 5.14, i.e.

$$\rho_0(\vec{X}) = \sum_i \phi_i^*(\vec{X}_i) \phi_i(\vec{X}_i), \quad (5.17)$$

The ground state total energy E_0 (see Eq. 5.13) is now derived by minimizing $E[\{\phi_i\}]$ under the constraint of Eq. 5.15

$$\int \rho_0(\vec{X}) d\vec{X} = \sum_i \int \phi_i^*(\vec{X}_i) \phi_i(\vec{X}_i) d\vec{X} = N_e \quad (5.18)$$

From that the so called Kohn-Sham equations

$$\hat{h}_{KS,i} \phi_i = \epsilon_i \phi_i \quad (5.19)$$

with the Kohn-Sham Hamiltonian h_{KS} ,

$$\hat{h}_{KS} = -\frac{1}{2}\nabla_i^2 + V_{eff}(\vec{X}) \quad (5.20)$$

are derived. The Hamiltonian consists of two parts. While the first one is the kinetic energy of a single particle the second one $V_{eff}(\vec{X})$ is the effective potential that contains all interactions, i.e.

$$V_{eff}(\vec{X}) = V_{ext} + V_{coul} + V_{xc}. \quad (5.21)$$

The so-called external potential V_{ext} can be identified with the electron-nucleus interactions in Eq. 5.8 and V_{coul} is the classical Coulomb interaction. Both can be treated exactly. The third term V_{xc} is the so called exchange-correlation potential. It is a functional derivative of the unknown exchange-correlation energy functional $E_{xc}[\rho]$ that contains the many-body electron-electron interactions, i.e.

$$V_{xc} = \frac{\delta E_{xc}[\rho]}{\delta \rho}, \quad (5.22)$$

Density functional theory in its formulation by Kohn and Sham yields the exact and correct ground state density as derived from Schrödinger equation. The only quantity that is to be approximated is the before mentioned exchange-correlation energy functional $E_{xc}[\rho]$. In other words these terms, V_{xc} and E_{xc} , have to be approximated. The usefulness of the approximation was the key part for the success of the density functional theory. Ways to treat this term will be discussed in the next chapter.

Having an approximation for E_{xc} the equations in Eq. 5.19 can be solved self-consistently resulting in the two fundamental quantities of density functional theory, the ground state density ρ_0 and the ground state total energy $E_0[\rho_0]$.

5.4 Approximations and Implementation

As seen in the previous chapter the exchange-correlation functional $E_{xc}[\rho]$ is unknown. For that reason it has to be approximated. The most common approximations are

- the local density approximation (LDA)

$$E_{xc}^{LDA}[\rho] = \int \rho(\vec{X}) \epsilon_{xc}(\rho) d\vec{X}. \quad (5.23)$$

Here the exchange-correlation energy E_{xc} is related to an exchange-correlation energy $\epsilon_{xc}(\rho)$ per particle in an (homogenous) free electron gas.

- the general gradient approximation (GGA)

$$E_{xc}^{GGA}[\rho, \vec{\nabla}\rho] \quad (5.24)$$

Here the local density approximation is extended by also including the gradient of the density.

For the actual calculations in this work the GGA [37] parametrisation of Perdew and Wang (PW91) [38] was chosen.

5.5 VASP

In this thesis for the calculation of ground state energies connected to given atomic arrangements the Vienna ab initio simulation package VASP [33], [34] was chosen. This software package was developed by Georg Kresse and his group. It is one of the most powerful DFT (and post-DFT) computer codes available, being a very important tool for a lot of working groups all over the world.

The first main feature of the VASP code is that it uses for Kohn-Sham orbitals ϕ_i (basis functions) plane waves and is therefore called a plane wave code.

The second (crucial) point is the construction of reliable pseudopotentials for valence states. For this task the VASP code relies on the projected augmented wave [35], [36] method.

Beside these elementary methods a lot of features according to relaxation algorithms, projections, summations, ... can be set in input files for VASP. Since the possibilities of simulations done with VASP are very extensive the interested reader is referred to the VASP manual which is available online [39].

It should only be pointed out here that the Nudged Elastic Band method for calculating transition paths introduced in chapter 3.2 is a standard tool included in VASP.

Chapter 6

Publication in *Intermetallics*

Title:

Monte-Carlo simulation of atom kinetics in intermetallics:
Correcting the jump rates in Ni₃Al.

Authors:

Martin Leitner

University of Vienna, Faculty of Physics, Department Dynamics of Condensed Systems

Doris Vogtenhuber

*University of Vienna, Faculty of Physics, Department of Computational Materials
Science*

Wolfgang Pfeiler

University of Vienna, Faculty of Physics, Department Dynamics of Condensed Systems

Wolfgang Püschl

University of Vienna, Faculty of Physics, Department Dynamics of Condensed Systems

Citation:

M. Leitner, D. Vogtenhuber, W. Pfeiler and W. Püschl, *Intermetallics* **18** 1091 (2010).

Article history:

Sent: 19th November 2009, Sent in revised form: 18th February 2010

Accepted: 19th February 2010.

6.1 Abstract

An improved Kinetic Monte-Carlo (KMC) algorithm for the simulation of atom configuration kinetics in intermetallics is introduced. In KMC a set of jump probabilities is computed from energy barriers. In transition state theory the barrier height is the difference between the initial equilibrium state and a saddle point state. It is on the latter that traditional treatments have made the most far-reaching assumptions, mostly setting it constant. A more detailed treatment of the saddle point state based on ab initio calculations of the actual jump profiles is proposed and demonstrated in Ni₃Al. It is shown in preliminary KMC simulations that individually computed saddle point energies make a considerable difference in jump statistics and overall kinetics of the long range order parameter.

6.2 Introduction

Intermetallic compounds with near-stoichiometric composition exhibit chemical long-range order at least below a critical temperature, in many cases even up to the melting point. Properties of considerable commercial value result from the ordered state. By imposing conditions on dislocation movement, order strengthens these materials, in some cases even progressively with rising temperature (flow stress anomaly [1], [2]). Besides that, many of these materials show good resistance to oxidation and corrosion [3]. When lattice distortion due to ordering leads to magneto-crystalline anisotropy these materials are prime candidates for magnetic recording purposes [4], [5]. In all these examples, for obvious reasons stability of the ordered state is a main concern. By the laws of thermodynamics the order parameter is a function of temperature. Starting e.g. from an equilibrium state at low temperature, after a sudden increase of temperature kinetic processes set in striving towards a new equilibrium state of less order. It is very important, from a standpoint of service reliability of materials, to know the nature and speed of such processes and the parameters influencing them. Changes of atom configuration in ordered alloys cannot be explained by a single parameter like migration enthalpy. Atom jumps must be differentiated as to their influence on order, as order-preserving or ordering-disordering. The specific atom surroundings have to be taken into account, and often it is necessary to consider complex hierarchies of energetic interactions. In contrast to other schemes of kinetic modelling which usually involve some kind of averaging before writing down the kinetic equations, Monte-Carlo (MC) simulation contains no assumptions apart from those entering in the single jump probabilities [6]. Its advantage is that it quite naturally reproduces the kinetics at all scales from atomic detail up to the evolution of a phase structure, though at corresponding computational cost. MC simulation has

been successfully applied in materials science, specifically in intermetallic compounds [7], [8], [9], [10], [11], [12], [13] - for a recent review see Haider, Kozubski, Abinandanan in [14]. It depends on the temperature range, the crystal structure and the strength of the inter-atomic bonding how we have to proceed in order to get realistic atom jump probabilities. When, as in intermetallic compounds far enough from the melting temperature, the transition state model [15] for atom jumps applies, transition probabilities are functions of the energies and vibration frequencies in the initial state and the saddle point state. We feel that especially saddle point energies have been a much neglected issue in many treatments based on these assumptions. In this paper in a first step we will try to improve on this point and so obtain more realistic jump probabilities.

6.3 Jump rates and energy barriers

Models for jump rate calculation

In many instances, so in intermetallics at not too elevated temperatures, transition state theory [15] may be considered valid ¹. The jump frequency Γ_{ij} from state i to state j is then given by

$$\Gamma_{ij} = \Gamma_0 \exp \left[-\frac{(E_s - E_i)}{k_B T} \right], \quad (6.1)$$

where Γ_0 is a quotient of normal frequencies in the initial equilibrium and the saddle point, and $(E_s - E_i)$ is the energy difference between these two positions. In most existing treatments making use of transition state theory the initial state is computed by means of some suitable Hamiltonian whereas the saddle point energy is left constant or at most made dependent on the type of the jumping atom [11], [12], [13]. Much MC work calculates the transition probabilities just from the initial and final energy states of the jumping atom. Saddle point energies enter here only implicitly, setting the time scale [7], [8], [9], [10]. In some cases saddle point energies were considered explicitly employing specific fitted potentials, so for instance by Oramus et al. [25]. We have reason to believe and will try to show quantitatively, that the respective atomic surroundings of the saddle point position should be considered for each jump.

The 4-atom window in the L1₂ structure

We discuss our concepts, which are however meant to be quite general, using the L1₂ ordered intermetallic compound Ni₃Al as a model system. The L1₂ structure is related to the fcc phase and has a stoichiometric composition of A₃B. A unit cell can be chosen with the B atoms located at the cube corners and the A atoms at the face centers. Henceforth, when talking about A atoms, these will always be Ni atoms, and B atoms will be Al

¹This assumption is questioned by Oramus et al. [32] for Ni₃Al on the basis of Molecular Dynamics calculations especially for highly correlated jumps.

atoms. As to atomic sizes, Al atoms are distinctly larger than Ni atoms, a fact which will have dramatic consequences for jump probabilities. The $L1_2$ structure can be divided into two sublattices (majority α - and minority β -sublattice) containing the A and B atoms respectively. Note that the neighborhood configurations for atoms on the two sublattices are different (Fig. 6.1).

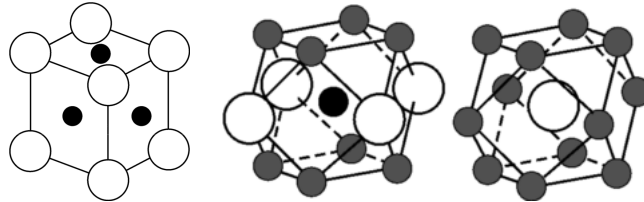


FIGURE 6.1: Conventional cubic cell of the $L1_2$ structure and nearest neighbor surroundings of the α - and β -sublattice. Majority A atoms are marked by filled dots, minority B atoms by open circles, respectively. On the α -sublattice an A atom has 8 further A atoms and 4 B atoms as nearest neighbors. An atom of kind B on the β -sublattice is surrounded by 12 A atoms in the first coordination shell .

When, in fcc-derived ordered structures such as $L1_2$, an atom moves to a nearest neighbor lattice site it has to pass through a rectangular 4-atom window. This window consists of common nearest neighbors to the original and the new position of the atom (Fig. 6.2). The specific configuration of this window depends on the degree of order and on the sublattices on which the atom sits before and after the jump.

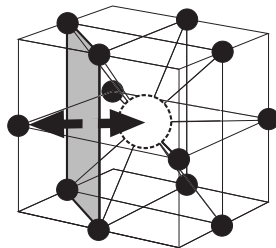


FIGURE 6.2: 4-atom window between an A atom located on the α -sublattice and a vacancy on the β -sublattice. It is made up of the four common nearest neighbor atoms.

Four types of point defects relevant to order occur in every ordered binary compound: vacancies (V_α , V_β) and antisite atoms (B_α , A_β) located on either sublattice. Based on the assumption that the elementary jump process is an exchange of a vacancy with one of its nearest neighbors, each jumping atom has to squeeze through this 4-atom window to exchange its position with the vacancy. So it is only natural to suppose that the occupancy of the window exerts the main influence on the the energy of the saddle point state the atom has to surmount.

How can we get reliable information on saddle point energies dependent on atom configuration? Obviously, this is not possible from experiments on order kinetics, since they always average over many different single atom jumps. In order to gain explicit insights into the energetics of atom jumps, we decided to perform first principles (*ab initio*) calculations according to a classification of possible jump types and window configurations.

6.4 *Ab initio* calculation of jump profiles

All *ab initio* calculations in this work are performed within the framework of density functional theory (DFT) using the Vienna *ab initio* simulation package VASP [16], [17]. The interaction between ionic cores and valence electrons is treated by the projector augmented wave method (PAW) [18], [19] with plane waves up to the energy of 350 eV. Exchange and correlation effects are described using generalized gradient corrections (GGA) [20] in the parametrization of Perdew and Wang (PW91) [21]. The Brillouin zone is sampled using a Monkhorst-Pack grid of k points [22].

To account for atomic defects in the system, supercells have to be constructed. One should be aware that supercells of different size correspond to different defect concentrations.

For the present demonstration purposes, supercells composed of 2x2x2 conventional cubic lattice cells are adopted. For better quantitative values, in a more detailed treatment calculations will be done in a 3x3x3 supercell. For all supercells describing the defect structures, the k -mesh has to be adapted for constant sampling density, yielding 6x6x6 for a 2x2x2 supercell. For Brillouin zone integration, the Methfessel-Paxton method with a smearing width of 0.2 eV is used.

Since we want to model a locally disturbed infinite solid, unwanted interaction with defects in neighboring supercells has to be avoided. Therefore, the atoms at the boundary of the supercell are kept fixed at their ideal positions. Only atoms that are fully contained in the supercell are allowed to relax. Geometry relaxation is performed with a conjugate gradient algorithm using Hellmann-Feynman forces, as implemented in VASP. It is assumed that equilibrium is reached if the forces on the non-fixed atoms are less than 0.02 eV/Å.

Jump profiles may be obtained by two approaches: One of them is 'static' displacement of the jumping atom along a designated jump path. Having obtained the equilibrium position of the monitored atom in its initial and final state after a full relaxation, a set of intermediate states (the jump path) is defined by linear interpolation of these positions. In each of these states the jumping atom is kept fixed on its intermediate position to avoid a relaxation into its initial or final position, while the surrounding atoms may relax.

The other approach, the nudged-elastic-band method (NEB) [23], [24] as implemented in VASP, is a standard tool for the determination of diffusion barriers. After a full relaxation of the initial and final state of each jump type, they are kept fixed and a reaction coordinate relating them is defined. Along the reaction path a set of intermediate states (images) of the system is defined, which are coupled in an additional dimension of phase space by spring forces to ensure continuity. To obtain the path that corresponds to the minimum of energy, each image is fully relaxed in the hyperspace perpendicular to the reaction coordinate and subject to the spring forces.

For configurations with a setup of high symmetry, straight path calculations and the NEB method yield the same results. In order to be consistent, in this work, all jump profiles were calculated using the NEB method, as in a 2x2x2 cell it is not excessively expensive anyhow.

Jump energy profiles were computed *ab initio* according to the following classification of possible jump types. Principally all possible jumps can be distinguished into order-preserving and ordering-disordering jumps (Fig. 6.3). If A or B atoms (B as antisites) move within the majority sublattice, order is preserved. In short notation, we will henceforth refer to these jumps as A: $\alpha \rightarrow \alpha$ and B: $\alpha \rightarrow \alpha$. If an atom jumps from one sublattice to the other, antisites are created or annihilated. We refer to these jumps as A: $\alpha \rightarrow \beta$ and B: $\beta \rightarrow \alpha$. Their jump profiles of course also refer to the cases A: $\beta \rightarrow \alpha$ and B: $\alpha \rightarrow \beta$ (reverse jumps).

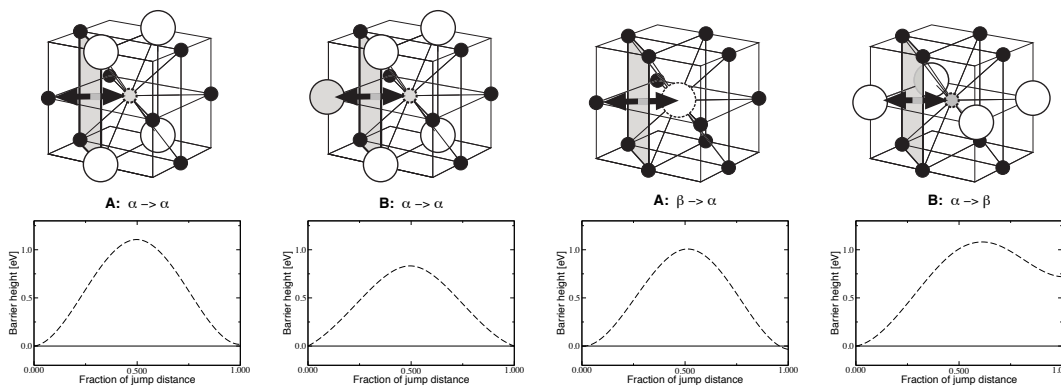


FIGURE 6.3: Basic jump types in the $L1_2$ structure: Order-preserving (left) and ordering-disordering jumps (right) with their corresponding jump profiles (in the case of B: $\alpha \rightarrow \alpha$, artificial asymmetry due to limited supercell size was corrected). The energy profiles were calculated *ab initio* using VASP. See text for details.

Since we expect the strongest influence on the jump barrier to be exerted by the occupancy of the 4-atom window the jumping atom has to pass, it is further necessary to obtain jump profiles for all possible window configurations (Fig. 6.4) for each of these basic jump types.

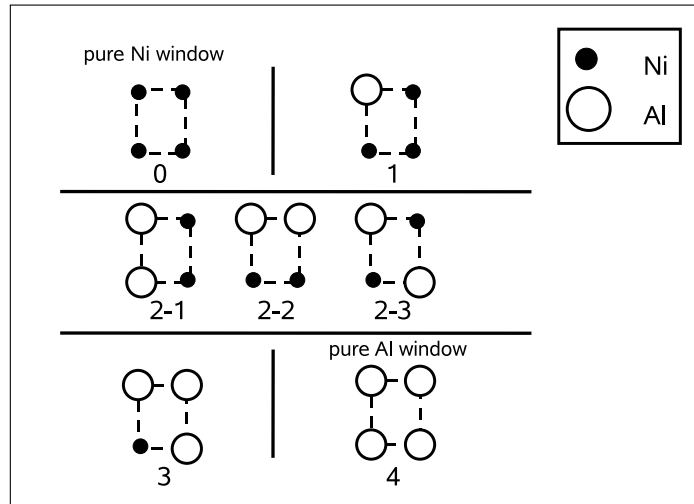


FIGURE 6.4: The seven geometrically independent window configurations

For the sake of analysis, we define a 'pure' barrier height E_{barr}^0 as the arithmetic mean of the forward and reverse barriers¹:

$$E_{barr}^0 = \frac{(E_s - E_i) + (E_s - E_j)}{2}. \quad (6.2)$$

6.5 Results for the jump profiles

Order preserving jumps

Our results for order preserving jumps in $2 \times 2 \times 2$ supercells are rendered in Table 1. With these jumps, atoms are only shifted within the majority α -sublattice. In the perfectly ordered lattice, the configuration of the initial and the final state is geometrically equivalent. Therefore $(E_j - E_i) = \Delta E_{ij} = 0$, and the barrier heights of forward- and backjumps should be the same ($E_{barr}^0 = (E_s - E_i) = (E_s - E_j)$). Any deviation from this rule is due to numerical artifacts caused by the restrictions we impose on the relaxation of particular atoms in the supercell. Thus, a slight asymmetry is introduced in the calculation cell, whereas there is no asymmetry in the real crystal.

Comparing the two possibilities of order-preserving atomic diffusion within the α -sublattice the following picture arises: As a general trend, the diffusion barrier for antisite (Al) atoms on the α sublattice is lower than for the majority Ni atoms which regularly sit there (except for configurations 3 and 4). This behavior corresponds qualitatively with MD calculations of previous authors [25]. We attribute this to the fact that the antisite

¹It has come to the attention of the authors that a very similar concept, there called 'kinetically resolved activation barrier' was introduced by Van der Ven et al. (2001) for diffusion of Li in Li_xCoO_2 [33]

TABLE 6.1: Pure barrier heights for all possible jump types and window configurations (definition: see Fig.6.4) in $L1_2$ Ni_3Al obtained by *ab initio* calculations. The relative energy values refer to a $2 \times 2 \times 2$ supercell and were obtained by NEB calculation. All values are in eV. Order preserving jumps: A: $\alpha \rightarrow \alpha$, B: $\alpha \rightarrow \alpha$ (left side) Ordering-disordering jumps: A: $\alpha \rightarrow \beta$, B: $\beta \rightarrow \alpha$ (right side)

window configuration	E_{barr}^0	window configuration	E_{barr}^0
<u>A: $\alpha \rightarrow \alpha$</u>		<u>A: $\alpha \rightarrow \beta$</u>	
0	1.02	0	1.03
1	1.00	1	1.32
2-1	1.10	2-1	1.54
2-2	1.03	2-2	1.28
2-3	1.17	2-3	1.64
3	1.09	3	1.53
4	1.09	4	1.48
<u>B: $\alpha \rightarrow \alpha$</u>		<u>B: $\beta \rightarrow \alpha$</u>	
0	0.29	0	0.72
1	0.55	1	1.20
2-1	0.83	2-1	1.77
2-2	0.83	2-2	1.60
2-3	0.99	2-3	1.96
3	1.28	3	2.35
4	1.76	4	2.92

atoms are less tightly bound on this sublattice than the other atom sort and therefore move in a shallower effective potential. For a jumping Ni atom, the barrier heights are remarkably constant for all possible window configurations. Compared to the configuration of highest possible order (window configuration 2-1), the variations (see Tab. 6.1 left side) range from -0.10 (window configuration 1) to $+0.07$ eV (window configuration 2-3), indicating that this jump type is not very sensitive to the nearest-neighbor atom configuration of the 4-atom window. On the other hand, for the second possible order-preserving jump process B: $\alpha \rightarrow \alpha$ the configuration of the window leads to a large variation. The jump of an Al atom is easiest through a window formed by 4 surrounding Ni Atoms (window configuration 0). Compared to this jump type, the barrier is increased by 1.47 eV for window configuration 4 (four surrounding Al atoms in the window). This qualitatively different behavior can easily be anticipated if one regards the difference of the atomic volumes of Ni and Al.

Ordering-disordering jumps

Ordering-disordering jumps (A: $\alpha \rightarrow \beta$, B: $\beta \rightarrow \alpha$ and their backjumps) lead to a creation (annihilation for the backjump) of an antisite (A_β , B_α) and to a change of the type of the vacancy (V_α , V_β). Both contributions enter the energy balance of the jumps.

Let us compare the two types of disordering jumps: The jump of an Al atom into a Ni vacancy (Fig. 6.3) leads to a final state of markedly enhanced energy, which is reasonable as the large Al atom, in its new position on the Ni sublattice is now surrounded by three equally large Al atoms as nearest neighbors (see Fig. 6.3 right). From that position, there is only a very low energy barrier to be surmounted for the backjump. It is therefore to be expected that this antisite-creating jump is immediately followed by the corresponding backjump with high probability, i.e. these processes show strong correlation.

Quite differently, a Ni atom jumping into an Al vacancy (where it fits in without any problem) in an otherwise perfectly ordered crystal (window configuration 0) is surrounded in its final state by nearest neighbor Ni atoms only (see Fig. 6.3). The jump transforms an energetically more expensive Al vacancy into a Ni vacancy [26], which practically compensates the antisite defect, hence the energy of the final state differs only very little from that of the initial state (Fig. 6.3).

The pure barrier heights resulting from *ab initio* calculated energy profiles for the possible jump types (Fig. 6.3) and window configurations (Fig. 6.4) for an environment of otherwise perfect long range order are given in Tab. 6.1 (right side).

6.6 MC Simulation results and discussion

In order to show the qualitative and quantitative difference between the traditional kinetic model with constant saddle point heights (CSP) and the proposed improved model with variable saddle point heights (VSP) we performed the following kinetic Monte-Carlo simulation: From an initial state of perfect long range order we let the system evolve at a finite temperature below the disorder temperature, towards an equilibrium state of imperfect order. As a kinetic Monte-Carlo algorithm well suited for the vacancy diffusion mechanism operative in intermetallics and specifically in Ni₃Al we chose the residence time algorithm (RTA) [27], [28], [29]. Its advantage is that in each MC time interval considered one atom jump definitely takes place. Therefore futile attempts as in the Metropolis [30] or Glauber [31] algorithms are avoided. In the RTA the average waiting time for an atom to jump into a given vacancy is computed as

$$\Delta t = \frac{1}{\sum_{j=1}^Z \Gamma_{ij}}, \quad (6.3)$$

the Γ_{ij} being the jump frequencies of any of the Z atoms surrounding the vacancy as nearest neighbors (Eq. (6.1)). Which of these atoms makes the jump is determined by a random variable $r \in [0,1]$ according to the set of probabilities

$$p_{ik} = \frac{\Gamma_{ik}}{\sum_{j=1}^Z \Gamma_{ij}}. \quad (6.4)$$

so that atom k jumps if

$$\sum_{j=1}^k p_{ij} < r \leq \sum_{j=1}^{k+1} p_{ij}.$$

For VSP the jump frequencies were adjusted making use of the *ab initio* barrier heights according to Tab. 6.1 by superimposing E_{barr}^0 to 1/2 of the energy difference before and after the jump (follows directly from Eq. (6.2)):

$$(E_s - E_i) = \Delta E_{is} = E_{barr}^0 + \frac{1}{2} \Delta E_{ij}. \quad (6.5)$$

Other configurations considering neighborhood antisite atoms outside the 4-atom window were not included in this stage of approximation as they yield effects of second order. The energies of the system before and after the jump were computed by adopting a simplified Hamiltonian according to Oramus et al. [3] with pair interactions up to the second coordination shell, with the following independent parameters (combined interaction energies, in eV per atom) :

$$\begin{aligned} \omega_1 &= 0.14, & \omega_2 &= -0.066, \\ \omega_1^* &= -0.07, & \omega_2^* &= -0.004 \end{aligned} \quad (6.6)$$

where $\omega = (E_{AA} + E_{BB} - 2E_{AB})$ is an ordering energy and $\omega^* = E_{AA} - E_{BB}$ is an asymmetry energy determining the kind of atom which jumps preferentially. The indices refer to the first and second coordination shell. The authors are aware that a more rigorous treatment should include many-body contributions, and work on a ternary cluster expansion (with vacancies) for the Ni-Al system is already under way. For the time being, the accuracy of the adopted approximation is amply sufficient to show our main point, the relevance of variable saddle point levels. The simulation cell contained 125,000 lattice sites and included 1 vacancy. Periodic boundary conditions in all directions were applied.

It is notoriously difficult to translate internal MC simulation time into real physical time. In order to compare the two conceptually different simulation models we chose to adopt the number of MC steps as a natural time scale. This is justified because when plotting elapsed MC time (Fig. 6.5), i.e. the sum of the time intervals Δt at each step, versus the number of MC steps, a linear relationship is obtained to a very good approximation.

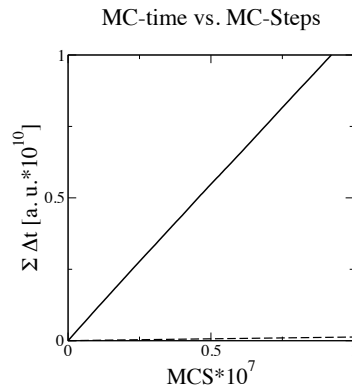


FIGURE 6.5: MC-Time vs. MC-Steps for the CSP (dashed line) and the VSP (solid line) model as obtained by the RTA algorithm at 1200 K. Although the both models differ in slope, both curves show a strictly linear behaviour.

In Fig. 6.6 the long-range order parameter is plotted after fitting a weighted sum of two exponentials to the numerical results

$$\eta(t) = A \exp\left(-\frac{t}{\tau_1}\right) + (1 - A) \exp\left(-\frac{t}{\tau_2}\right) \quad (6.7)$$

$$\text{with } 0 \leq A \leq 1; \tau_2 > \tau_1$$

for both models (CSP and VSP) as a function of the number of MC steps for two annealing temperatures, 1200 K and 1650 K with an initial state of perfect order. The two relaxation times τ_1 and τ_2 can be interpreted as a faster and a slower relaxation process [9].

The corresponding equilibrium degrees of long-range order are $\eta=0.97$ and $\eta=0.76$, respectively. As must be, both models, the traditional one with constant saddle point heights and the improved one with variable saddle point heights, lead to the same equilibrium value since the principle of detailed balance is fulfilled in each ansatz. A striking difference can however be noticed in the kinetics of the system. It is seen in Fig. 6.6 that more jumps are needed to produce a specified change of order in the improved model. The reason is a strong correlation effect between antisite-generating MC jumps and their backjumps.

It is noticed that a two-process kinetics comparable to Oramus et al. [9] was obtained for both final temperatures in the CSP as well as in the VSP model. The values of the relaxation times of the faster and the slower process correspond qualitatively with the published values in [9]. It should be pointed out that Oramus et al. studied situations of order-order small-step annealing with a different final temperature (1350 K) whereas we chose a comparatively large temperature step. It is planned to publish a more detailed comparison with this and other published results in a forthcoming paper. Nevertheless,

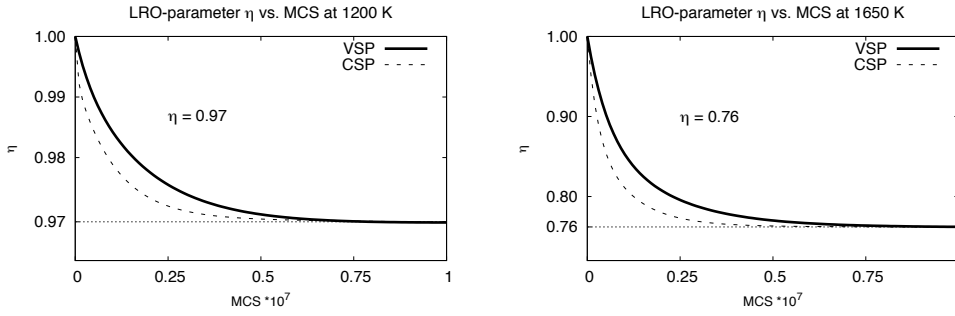


FIGURE 6.6: Long range order parameter η versus MC step number for the VSP (full line) and CSP (dashed line) models for the energy parameters adapted to Ni_3Al . Annealing temperatures are 1200 K (left) and 1650 K (right). In both cases the initial stage was a system corresponding to perfect order and containing 1 vacancy. Dotted line: final equilibrium value. Note the different scalings.

TABLE 6.2: Obtained fit parameters A , τ_1 and τ_2 for CSP and VSP model.

Temperature	model	A	τ_1 [MCS* 10^6]	τ_2 [MCS* 10^6]
1200 K	CSP	0.25	0.08	1.18
	VSP	0.09	0.22	1.63
1650 K	CSP	0.78	0.41	1.98
	VSP	0.45	0.52	1.81

we notice that there is no striking difference in the relaxation times of the slower and the faster process with respect to the CSP and VSP model, especially in the case of the higher final temperature of 1650 K. In contrast, the weight factors of the processes differ considerably (see Tab. 6.2).

A detailed jump statistics at different stages was carried out to get a deeper insight into the kinetics resulting from each ansatz. The first 100,000 steps of independent runs were analyzed to get a grip on the differences in the initial stages of ordering in both models. Results for the relative weights in jump statistics of the six standard cases (two kinds of order-preserving jumps, two kinds of ordering jumps and two kinds of disordering jumps) for the temperature of 1200 K and 1650 K can be found in Fig. 6.7. There is a marked difference in the relative frequency of jump types. For the CSP model, the diffusion of A atoms within the α -sublattice is dominating, leading to a high mobility of the vacancy within the system. For VSP the majority of jumps are of the type B: $\beta \rightarrow \alpha$ where a B atom exchanges its position with a vacancy located on the α -sublattice and the corresponding backjump. The reason for this behaviour can be found in Fig. 6.3 and Fig. 6.7. If a B atom jumps into a vacancy located on the α -sublattice, an energetically very unfavourable antisite is generated and there is a very high probability that the backjump to the initial configuration of the system is taking place within the next step, since the barrier to be surmounted is very small due to the enhanced energy of the antisite. This

behaviour leads to a 'trapping' of the vacancy on small time scales and to an effective decrease of mobility.

The same qualitative behaviour is seen in the equilibrium state of the systems. Here 1,000,000 MC steps of independent runs have been analyzed after reaching a stable degree of long-range order (Fig. 6.7).

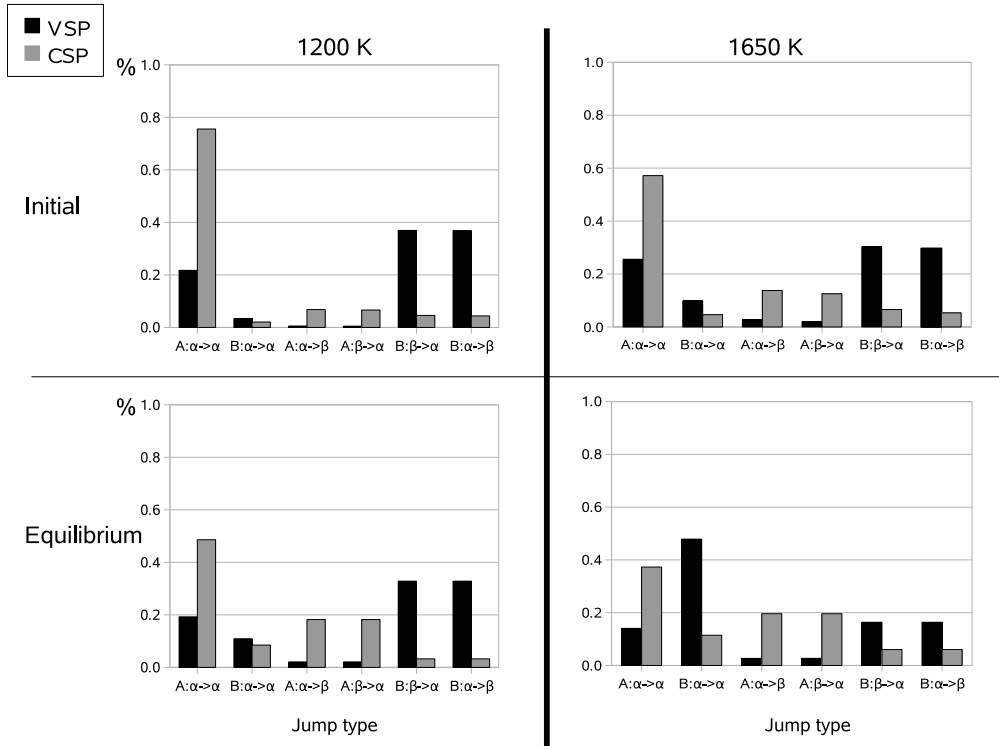


FIGURE 6.7: Fractions of all possible jump types in the the new, improved VSP model as compared to the CSP model at temperatures of 1200 K and 1650 K in initial and equilibrium phases of the kinetics. The corresponding long-range order parameter is 0.96 and 0.76, respectively. In the upper row the first 100,000 jumps of independent runs were analyzed to demonstrate the initial phase of ordering. The bottom row shows the fractions of jump types after the systems have reached their equilibrium states. These statistics are based on 1,000,000 jumps for each independent run. In the initial state, the frequencies of disordering and ordering jumps differ but very slightly.

This is however sufficient to generate the overall disordering effect.

Furthermore a statistics of the window types the jumping atoms pass through was recorded at the two temperatures considered. Here the behavior strongly depends on the jump type. As pointed out in the discussion of the *ab initio* results, the barrier height of an A atom diffusing on its own sublattice (A: $\alpha \rightarrow \alpha$) remains more or less constant independent of the configuration of the 4-atom window. This fact is also visible in the window statistics of this jump type comparing the old with the new model (see Fig. 6.8).

In both stages of the system (initial and equilibrium) the fractions of passed windows are very similar for each temperature.

In B: $\alpha \rightarrow \alpha$ jumps, however, a selection for energetically cheaper jumps through windows with less B atoms becomes evident. The probabilities in the VSP model are strongly shifted towards the window configuration cases 0 and 1 away from the 'standard case' 2-1 valid for the perfectly ordered lattice (Fig. 6.8).

In ordering-disordering jumps the energetic preference for low-B windows in the VSP model leads to a stronger concentration of probabilities towards the window configuration case 0 than would result in the CSP model out of the statistical occurrence of the various window types alone (Fig. 6.9).

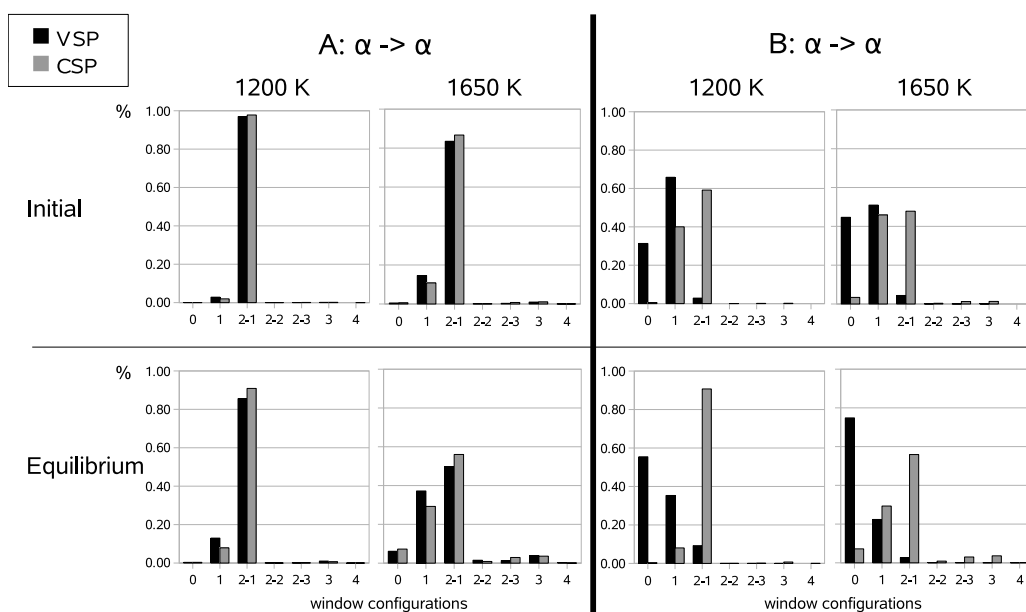


FIGURE 6.8: Comparison of fractions of all possible window types that are passed by A and B atoms in order-preserving jumps at 1200 K and 1650 K and in different phases of the kinetics (top: initial, bottom: equilibrium).

The results of Figs. 6.7-6.9, especially when comparing the two different temperatures 1200 K and 1650 K, should always be viewed having in mind the two factors from which they arise: 1) A possibly different distribution of antisites and/or window types due to the different degree of order, 2) the different energetic bias of jump types and window types in the two models CSP and VSP. For instance, at higher temperatures in equilibrium there are more B: $\alpha \rightarrow \alpha$ jumps just because due to the reduced degree of order there are more antisite B atoms on the α sublattice. Likewise, when looking at Fig. 6.8 and jump types B: $\alpha \rightarrow \alpha$, there is a distinctly greater preference for window type 0 (as compared to type 2-1) at 1650 K than is the case at 1200 K, even though the diminished energetic bias acts in the other direction. Once again, the reason is that at a lesser degree of order

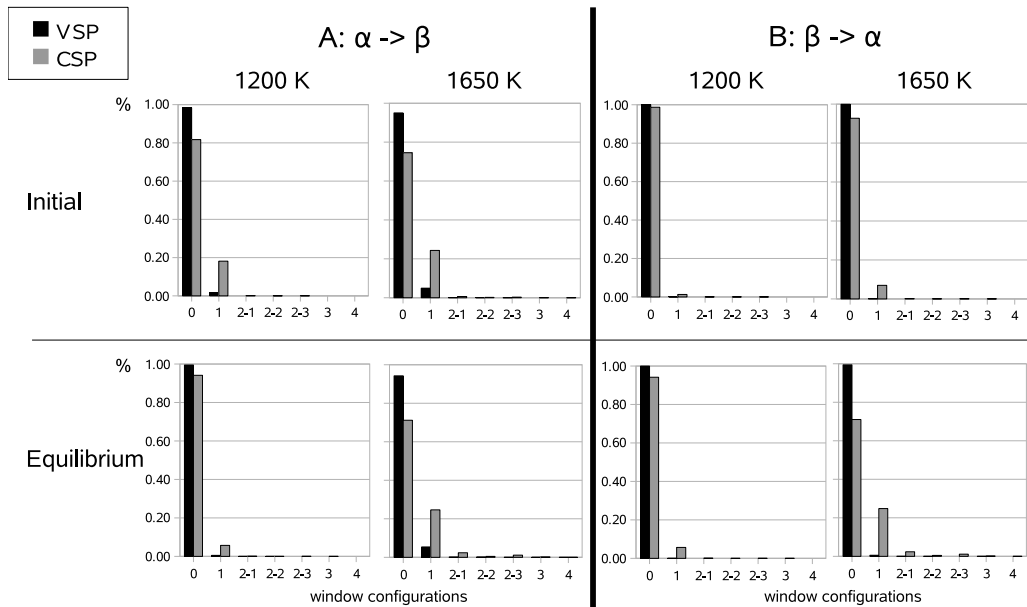


FIGURE 6.9: Comparison of fractions of all possible window types that are passed by A and B atoms in disordering jumps at 1200 K and 1650 K and in different phases of the kinetics (top: initial, bottom: equilibrium).

the predominance of the standard window type 2-1 for this kind of jump becomes less pronounced.

These preliminary KMC results are open to improvement regarding (i) a better crystal configuration Hamiltonian, (ii) calculation of the jump profiles on larger supercells and (iii) with different surroundings outside the 4-atom window. They show nevertheless the unmistakable effect which variable jump barriers have on jump statistics and the details of kinetics.

6.7 Conclusions

From energy profiles of atom jumps calculated *ab initio* we derived barrier heights in a long range ordered Ni₃Al model system. Making allowance for the individual atomic neighborhood of the jumping atom when being in saddle point position turns out to be vital. Though still preliminary, the results can be summarized as follows:

- Barrier height is strongly influenced by atom environment of saddle point position (4-atom window).
- *Ab initio* jump profiles can be consistently analyzed introducing a 'pure barrier height'. It increases monotonously with the number of B (Al) atoms belonging to the window.
- In a MC simulation of isothermal kinetics the introduction of variable saddle point heights (VSP) alters the kinetic details drastically. In the jump statistics the relative incumbencies of specified jump types are shifted. The long-range order parameter shows a distinctly changed kinetic behaviour, the main reason being strong correlation effects of disordering Al jumps.

Acknowledgments

This work was supported by the Austrian *Fonds zur Förderung der wissenschaftlichen Forschung* (FWF) under grant Nr. P19548-N16.

We thank Prof. Christoph Dellago for valuable technical support with our hardware configuration.

Bibliography

- [1] P. Veyssiere and G. Saada, in 'Dislocations in solids', Ed. F.R.N. Nabarro, Vol. 10, Amsterdam, North-Holland (1996).
- [2] J.H. Westbrook and R.L. Fleischer, in 'Intermetallic compounds-principles and practice', Vol. 1 and 2 (Wiley, Chichester, 1994).
- [3] N.S. Stoloff, C.T. Liu and S.C. Deevi, *Intermetallics* **8** 1313 (2000).
- [4] D. Weller, A. Moser, I. Folks, M.E. Best, W. Lee, M.F. Toney, M. Schwickert, J.U. Thiele and M.F. Doerner, *IEEE Trans. Magn.* **36** 10 (2000).
- [5] J. S. Chen, B.C. Lim, Y.F. Ding and G.M. Chow, *J. Magn. Mater.* **303** 309 (2006).
- [6] K. Binder and D. W. Heermann, in 'Monte Carlo Simulation in Statistical Physics', 3rd edition, Springer, Berlin-Heidelberg 1997.
- [7] T. F. Lindsey and B. Fultz, in 'Diffusion in Ordered Alloys', Ed. B. Fultz, R. W. Cahn and D. Gupta, The Minerals, Metals and Materials Society, 1993, p. 91.
- [8] P. Oramus, R. Kozubski, V. Pierron-Bohnes, M. C. Cadeville, C. Massobrio and W. Pfeiler, *Mat. Sci. Eng. A* **324** 11 (2002).
- [9] P. Oramus, R. Kozubski, V. Pierron-Bohnes, M. C. Cadeville and W. Pfeiler, *Phys. Rev. B* **63** 174109 (2001).
- [10] R. Kozubski, P. Oramus, W. Pfeiler, V. Pierron-Bohnes and M. C. Cadeville, in 'Proceedings Solid-Solid phase transformations 99 (JIMIC-3)', Ed. M. Koiwa, K. Otsuka and T. Miyazaki, The Japan Institute of Metals, 1999, p. 473.
- [11] M. Athenes, P. Bellon, G. Martin, and F. Haider, *Acta mater.* **44** 4739 (1996).
- [12] M. Athenes, P. Bellon and G. Martin, *Acta Materialia* **48** 2675 (2000).
- [13] T.A. Abinandanan, F. Haider and G. Martin, *Acta mater.* **46** 4243 (1998).

- [14] F. Haider, R. Kozubski and T.A. Abinandanan, in 'Alloy Physics: A Comprehensive Reference', Ed. Wolfgang Pfeiler, Wiley-VCH, 2007, p. 653.
- [15] G. H. Vineyard, *J. Phys. Chem. Solids* **3** 121 (1957).
- [16] G. Kresse and J. Furthmüller, *Phys. Rev. B* **54**, 169 (1996).
- [17] G. Kresse and J. Furthmüller, *Comput. Mater. Sci.* **6** 15 (1996).
- [18] P. Blöchl, *Phys. Rev. B* **50** 953 (1994).
- [19] G. Kresse and D. Joubert, *Phys. Rev. B* **59** 1758 (1999).
- [20] J.P. Perdew, J.A. Chevary, S.H. Vosko, K.A. Jackson, M.R. Pedersen, D.J. Singh and C. Fiolhais, *Phys. Rev. B* **46** 6671 (1992).
- [21] J.P. Perdew and Y. Wang, *Phys. Rev. B* **45** 13244 (1992).
- [22] H.J. Monkhorst and J.D. Pack, *Phys. Rev. B* **13** 5188 (1976).
- [23] G. Mills, H. Jonsson and G. K. Schenter, *Surf. Sci.* **324** 305 (1995).
- [24] A. Ulitsky and R. Elber, *J. Chem. Phys.* **92** 1510 (1990).
- [25] P. Oramus, R. Kozubski, V. Pierron-Bohnes, M. C. Cadeville, C. Massobrio and W. Pfeiler, *Defect and Diffusion Forum* **194-199** 453 (2001).
- [26] D. Vogtenhuber, J. Houserova, W. Wolf, R. Podloucky, W. Pfeiler and W. Püschl, *Defect and Diffusion Forum* **237-240** 133 (2005).
- [27] A.B. Bortz, M.H. Kalos and L.J. Lebowitz, *J. Comput. Phys.* **17** 10 (1975).
- [28] W.M. Young, E.W. Elcock, *Proc. Phys. Soc.* **89** 735 (1966).
- [29] F. Haider in 'Ordering and Disordering in Alloys', Ed. R. Yavari, Elsevier Applied Science, London and New York 1993, p. 215.
- [30] N. Metropolis, A.W. Rosenbluth, N.N. Rosenbluth and E. Teller, *J. Chem. Phys.* **21** 1087 (1953).
- [31] R.J. Glauber, *J. Math. Phys.* **4** 294 (1963).
- [32] P. Oramus, C. Massobrio, M. Kozłowski, R. Kozubski, V. Pierron-Bohnes, M. C. Cadeville and W. Pfeiler, *Comp. Mat. Sci.* **27** 186 (2003).
- [33] A. Van der Ven, G. Ceder, M. Asta and P.D. Tepesch, *Phys. Rev. B* **64** 184307 (2001).

Chapter 7

Publication in *Solid State Phenomena*

Title:

Saddle point energies from ab initio jump profiles in MC simulation of order kinetics in intermetallics.

Authors:

Martin Leitner

University of Vienna, Faculty of Physics, Department Dynamics of Condensed Systems

Doris Vogtenhuber

University of Vienna, Faculty of Physics, Department of Computational Materials Science

Wolfgang Pfeiler

University of Vienna, Faculty of Physics, Department Dynamics of Condensed Systems

Wolfgang Püschl

University of Vienna, Faculty of Physics, Department Dynamics of Condensed Systems

Citation:

M. Leitner, D. Vogtenhuber, W. Pfeiler and W. Püschl, *Solid State Phenomena* **172-174** 1022 (2011).

Article history:

Accepted: 19th April 2011.

7.1 Abstract

Kinetic Monte Carlo (KMC) simulation is a valuable tool to investigate configuration changes in intermetallic compounds. The elementary process is the jump of an atom from a lattice site to a neighboring vacancy. In classical transition state theory the jump rate contains the energy difference between the original equilibrium state and the saddle point (= transition) state. In traditional KMC the saddle point has mostly received rather careless treatment, setting it constant or relating it to the type of jumping atom. In the present work, saddle point heights were considered explicitly. Taking L1₂ ordered Ni₃Al as an example, jump energy profiles for various atom environments were calculated *ab initio* in relaxed configurations of a 3x3x3 supercell, employing the Nudged Elastic Band method where necessary. From these results, effective 'pure' saddle point heights were extracted. To show the effect on kinetics, simulations of order-order transitions were done with jump probabilities based on these results. When compared to the old assumption of constant saddle point heights, both overall kinetics and detailed jump statistics result considerably changed.

7.2 Introduction

Monte-Carlo simulation (MC, for a review see e.g. [1]) has been and still is one of the most important methods to deal in atomistic detail with atom configuration kinetics in alloys. MC simulation resting on the mathematical assumption of a Markov process, all modelling is contained in a set of transition probabilities which depend only on the current state of the system. In many instances, so in most cases in strongly bound intermetallics at not too high temperatures, these can be calculated by means of the classical transition state theory [5]. Apart from an attempt frequency given by lattice vibration modes as a pre-factor, the energy difference between the initial equilibrium and a saddle point state of the jumping atom enters via a Boltzmann factor. Whereas in treatments existing in the literature various schemes have been employed to calculate the energy of the initial state, like attention apparently has not been devoted to the saddle point state (for an overview see [1]). That its energy value is sensitive to individual atomic environment, and that these differences have an impact on kinetics, this paper intends to demonstrate, taking L1₂-ordered Ni₃Al as an example.

7.3 Jump rates and energy barriers

Jump rate calculation based on transition state theory. In state i an atom lies adjacent to a vacancy. In state j it has jumped into this vacancy. The corresponding transition rate is given by

$$\Gamma_{ij} = \Gamma_0 \exp \left[-\frac{(E_s - E_i)}{k_B T} \right], \quad (7.1)$$

with Γ_0 being a quotient of normal frequencies in the original equilibrium and the saddle point, and $(E_s - E_i)$ being the energy difference between these two positions. Several authors have taken account of various saddle point environments, mostly using indirect methods of energy calculation such as EAM potentials, e.g. [2], [3] or cluster expansion [4]. We want to show via *ab initio* calculations that the respective atomic surroundings of the saddle point position should be considered for each jump. In the analysis of jump barrier heights the following scheme has proved advantageous,

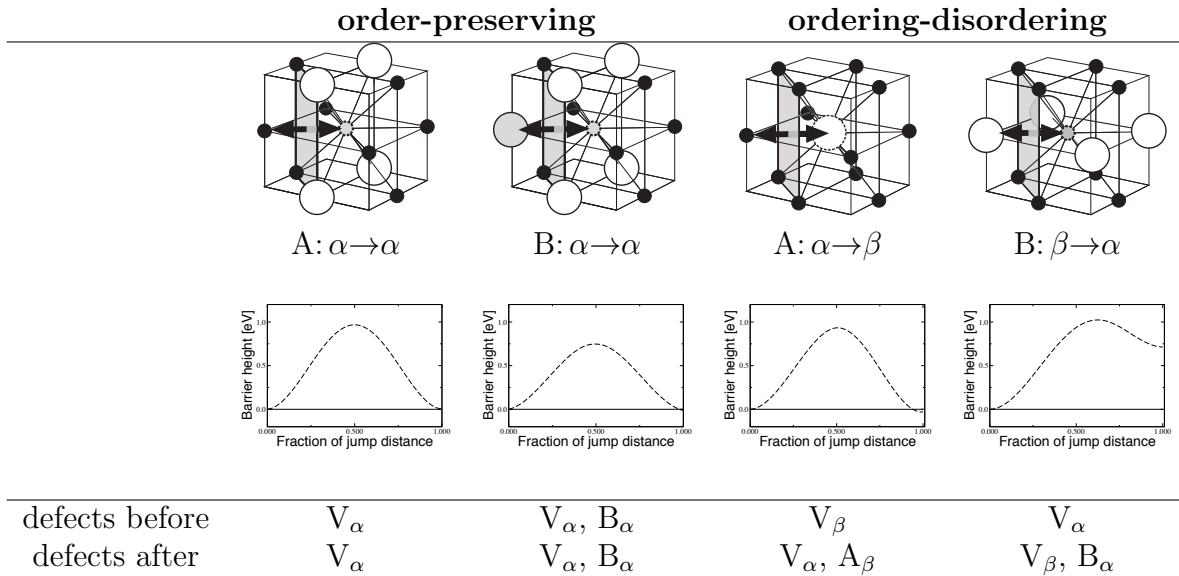
$$E_s - E_i = E_{is} = E_{barr}^0 + \frac{E_i + E_j}{2} \quad (7.2)$$

Here the barrier height E_{is} is composed of a 'pure' barrier height E_{barr}^0 superimposed on a baseline connecting the energy values E_i, E_j of the initial and final states. This definition of the barrier height also allows us to fulfil the principle of 'detailed balance' in KMC.

Jump types in the L1₂ structure. For the demonstration of our concepts we chose the technically interesting L1₂-ordered intermetallic compound Ni₃Al as a model system. Basic concepts (classification of jumps, window types) hold, however, for all L1₂ ordered binary alloys (and partly for other fcc based ordered structures like L1₀ or L1₁). For the perfectly ordered lattice the configuration of the neighboring atoms at each sublattice is different. While an A atom (α -sublattice) has a neighborhood in the first coordination shell of 8 A (α) atoms and 4 B (β) atoms, a B atom (β -sublattice) is surrounded by A (α) atoms only. Therefore nearest-neighbor (NN) jumps can take place only either within the α -sublattice or between the α - and β -sublattices. In the first case the state of long-range order is preserved, in the second case it is changed. This allows a classification of jumps according to Tab. 7.1.

Careful analysis showed that the influence on E_{barr}^0 (Eq. 7.2) of an antisite atom in NN position to the jumping atom is about an order of magnitude lower when it is not part of the 4-atom window of nearest neighbors common to the atom and the vacancy, as compared to the case when it belongs to this window. The configuration of this window therefore exerts the main influence on barrier height. All possible (geometrically independent) window configurations are shown in Fig. 7.1. To calculate jump energy profiles for this set of standard situations we employed *ab initio* density functional theory as the

TABLE 7.1: Order-preserving (left) and ordering-disordering (right) jump types in the L1₂ structure and their corresponding energy profiles, calculated *ab initio* using VASP (see text for details). The jumping atom has to cross a 4-atom window of common nearest neighbors. In the bottom lines the point defects present before and after the jump are also shown, V_α being a vacancy on the α-sublattice, B_α being an antisite B atom on the α-sublattice etc.



currently best method available.

Ab initio calculation of jump profiles. For all *ab initio* calculations based on the framework of density functional theory (DFT) the Vienna *ab initio* simulation package VASP [6], [7] was used with generalized gradient corrections (GGA) [8], [9].

Since our focus is on modeling a locally disturbed (infinite) crystal we have to find a way to avoid unwanted interactions with the periodically repeated defects in the 'neighboring' images of the original supercell. Therefore the atoms at the boundary of the supercell have to be kept fixed at their ideal lattice positions. The merits of this approach have been discussed by van der Walle [10]. The calculation supercell then has to be chosen

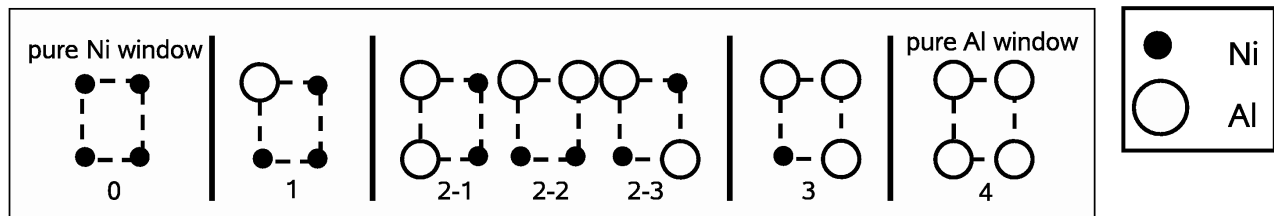


FIGURE 7.1: Definition of the seven geometrically independent window configurations

TABLE 7.2: Pure barrier heights obtained by *ab initio* calculations for L1₂ Ni₃Al. For the definition of all possible jump types and window configurations see Tab. 7.1 and Fig. 7.1. The bold relative energy values refer to a 3x3x3 supercell whereas values for a 2x2x2 supercell are also shown for comparison. All values are in eV. Order-preserving jumps: A: $\alpha \rightarrow \alpha$, B: $\alpha \rightarrow \alpha$ (left side) Ordering-disordering jumps: A: $\alpha \rightarrow \beta$, B: $\beta \rightarrow \alpha$ (right side)

window configuration	E_{barr}^0	window configuration	E_{barr}^0		
<u>A: $\alpha \rightarrow \alpha$</u>	2x2x2	3x3x3	<u>A: $\alpha \rightarrow \beta$</u>	2x2x2	3x3x3
0	1.02	0.97	0	1.03	0.95
1	1.00	0.94	1	1.32	1.18
2-1	1.10	0.97	2-1	1.54	1.39
2-2	1.03	0.97	2-2	1.28	1.15
2-3	1.17	1.06	2-3	1.64	1.40
3	1.09	0.97	3	1.53	1.36
4	1.09	0.93	4	1.48	1.34
<u>B: $\alpha \rightarrow \alpha$</u>	2x2x2	3x3x3	<u>B: $\beta \rightarrow \alpha$</u>	2x2x2	3x3x3
0	0.29	0.29	0	0.72	0.58
1	0.55	0.49	1	1.20	0.96
2-1	0.83	0.75	2-1	1.77	1.45
2-2	0.83	0.77	2-2	1.60	1.26
2-3	0.99	0.86	2-3	1.96	1.49
3	1.28	1.12	3	2.35	1.85
4	1.76	1.52	4	2.92	2.25

large enough so that residual forces on these atoms due to the elastic distortion around the defect(s) can be neglected. In our case, a supercell consisting of 3x3x3 conventional lattice cells (108 lattice positions) has proved sufficient, whereas a 2x2x2 supercell is not. As the jump path cannot *a priori* be assumed as straight, in the general case the Nudged Elastic Band method (NEB) [11], [12] has to be used. It turns out, however, that this is necessary only for B: $\alpha \rightarrow \alpha$ jumps [13].

7.4 Results

Results for the jump profiles. We want to point out some features of the values for the pure barrier height E_{barr}^0 shown in Tab. 7.2. Regarding order-preserving jumps, we see that, except for configurations 3 and 4, barrier heights for antisite atoms (B: $\alpha \rightarrow \alpha$) are lower than for regular A atoms. We explain this behavior by the fact that a B atom has weaker bonding on this sublattice and therefore moves in a shallower potential. Furthermore it is seen that the occupancy of the 4-atom window has almost no influence at all on A: $\alpha \rightarrow \alpha$ jumps. Regarding ordering-disordering jumps, the following picture arises: The jump barrier for an Al atom (B: $\beta \rightarrow \alpha$) increases with every Al atom in the window

it has to pass. The same behavior also holds for Ni atom jumps (A: $\alpha \rightarrow \beta$). However, in this jump a kind of 'saturation' occurs when it has to pass windows that consist of 2 or more Al atoms.

Results of MC Simulation. As an example to illustrate the consequences of incorporating variable saddle point heights we performed MC simulations of order-order relaxations. We chose the residence time algorithm [14] as it is particularly well suited for the vacancy mechanism of diffusion operative in intermetallics like Ni₃Al. Its principal advantage is that in each MC step an atom jump occurs.

For the jump frequencies we adopt the jump barrier composition according to Eqn. 7.2 where we used the pure barrier heights as calculated *ab initio* (Tab. 7.2) and for the energy baseline an Ising-type Hamiltonian adapted to experimental order temperatures from Oramus et al. [15]. A calculation cell of 125,000 atoms was chosen, periodically continued in all directions. We let the system evolve from an initial state of perfect order to an equilibrium state of partial order at 1200K and 1650K, respectively (the critical temperature for this model being $T_{O/D} = 1720$ K).

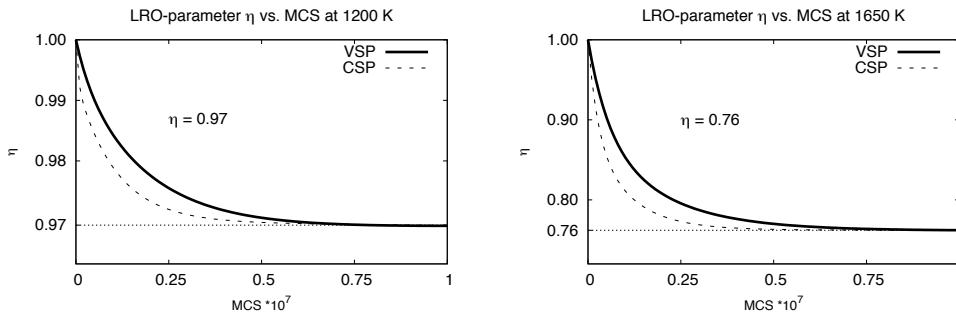


FIGURE 7.2: Relaxation curves of the long range order (LRO) parameter η for two annealing temperatures 1200 K (left) and 1650 K (right). The overall kinetics of the improved VSP (full line) model and the CSP (dashed line) model are compared for the energy parameters adapted to Ni₃Al. In both cases the simulation was started in an initial stage of perfect order (containing 1 vacancy) and the system was relaxed towards its equilibrium state, which is shown by the dotted line. Note the different scalings.

The kinetics of the long-range order parameter is shown in Fig. 7.2, where our model of variable saddle point heights (VSP) is compared to an alternative one of constant saddle point heights (CSP). In order to make possible a comparison of these different models, time is measured in numbers of MC steps. Although in a residence time algorithm individual time intervals vary considerably, the average time interval is remarkably constant (see Ref. [13]). In the new, VSP model the the ratio of relaxation rates at the beginning and at the end of the kinetic process is smaller than in the CSP model. The reason becomes

clear from a statistics of jump types (Fig. 7.3a, where the results for the VSP model appear in black). Whereas in the CSP model order-preserving Ni jumps predominate, in the VSP model antisite-generating Al jumps, linked in strong correlation to their reversals, retard the overall kinetics. This behavior can be understood when looking at the jump profile of the B: $\beta \rightarrow \alpha$ jump in Tab. 7.1: The antisite atom has a very low energy barrier favoring its immediate return to its regular position on the β -sublattice. Going

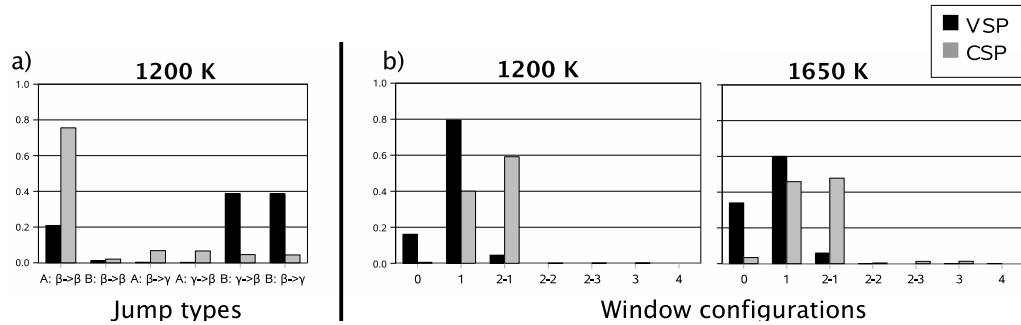


FIGURE 7.3: Initial phase of the kinetics at temperatures of 1200 K and 1650 K: improved VSP model (black) as compared to the CSP model (grey). The initial phase of ordering corresponds to the first 100,000 jumps of independent runs. a) Distribution of jump types according to Tab. 7.1. b) For order-preserving B: $\beta \rightarrow \alpha$ jumps, statistics of jumps through windows with different configurations according to Fig. 7.1

into still more detail by making a statistical evaluation of the jumps through 4-atom windows with different occupation reveals an expected clear preference of windows with a lower energy barrier. This becomes especially evident with B: $\alpha \rightarrow \alpha$ jumps (Fig.7.3b). Note that although window occupation 2-1 in this case is the sole starting configuration for a perfectly ordered lattice, it is virtually suppressed in the VSP model, even in the initial stages of the kinetics. As soon as a slight disordering produces a small number of energetically 'cheaper' windows, kinetics prefers them.

7.5 Conclusions

As a summary of our calculations we state that

- In order to get reliable atom jump energy barriers in $L1_2$ ordered Ni_3Al a $3 \times 3 \times 3$ calculation supercell (108 atom positions) is both mandatory and sufficient.
- For NN jumps the occupancy of a 4-atom window of common nearest neighbors to the original and final positions exerts the main influence on barrier heights.
- *Ab initio* jump energy profiles can best be rationalized by defining a pure barrier height superimposed on a baseline connecting the energies of the initial and final states.
- Pure barrier heights depend on window occupancy in different degree according to jump types. The dependence is most pronounced for jumps of B (Al) atoms, where barrier height strongly increases with the number of B atoms in the window.
- When incorporating variable saddle point heights into KMC simulation the overall kinetics is altered due to strong correlation effects. The detailed jump statistics shows a pronounced shift towards energetically more favorable windows.

Acknowledgments

This work was supported by the Austrian *Fonds zur Förderung der wissenschaftlichen Forschung* (FWF) under grant Nr. P19548-N16.

Bibliography

- [1] F. Haider, R. Kozubski and T.A. Abinandanan, in: *Alloy Physics: A Comprehensive Reference*, edited by W. Pfeiler, Wiley-VCH, 2007, p. 653.
- [2] Y. Le Bouar and F. Soisson: *Phys. Rev. B* Vol. 65 (2002), p. 0914103.
- [3] P. Oramus, C. Massobrio, M. Kozłowski, R. Kozubski, V. Pierron-Bohnes, M.C. Cadeville and W. Pfeiler: *Comput. Mater. Sci.* Vol. 27 (2003), p. 186.
- [4] A. Van der Ven, G. Ceder, M. Asta and P.D. Tepesch: *Phys. Rev. B* Vol. 64 (2001), p. 184307.
- [5] G. H. Vineyard: *J. Phys. Chem. Solids* Vol. 3 (1957), p. 121.
- [6] G. Kresse and J. Furthmüller: *Phys. Rev. B* Vol. 54 (1996), p. 169.
- [7] G. Kresse and J. Furthmüller: *Comput. Mater. Sci.* Vol. 6 (1996), p. 15.
- [8] J.P. Perdew, J.A. Chevary, S.H. Vosko, K.A. Jackson, M.R. Pedersen, D.J. Singh and C. Fiolhais: *Phys. Rev. B* Vol. 46 (1992), p. 6671.
- [9] J.P. Perdew and Y. Wang: *Phys. Rev. B* Vol. 45 (1992), p. 13244.
- [10] C.G. Van de Walle and J. Neugebauer: *J. Appl. Phys.* Vol. 95 (2004), p. 3851.
- [11] G. Mills, H. Jonsson and G. K. Schenter: *Surf. Sci.* Vol. 324 (1995), p. 305.
- [12] A. Ulitsky and R. Elber: *J. Chem. Phys.* Vol. 92 (1990), p. 1510.
- [13] M. Leitner, D. Vogtenhuber, W. Pfeiler and W. Püschl: *Intermetallics* Vol. 18 (2010), p. 1091.
- [14] A.B. Bortz, M.H. Kalos and L.J. Lebowitz: *J. Comput. Phys.* Vol. 17 (1975), p. 10.
- [15] P. Oramus, R. Kozubski, V. Pierron-Bohnes, M. C. Cadeville and W. Pfeiler: *Phys. Rev. B* Vol. 63 (2001), p. 174109.

Chapter 8

Additional results for $L1_2$ Ni_3Al

In this chapter considerations and results additional to those published in the papers in the preceding chapters 6 and 7 are given.

This chapter has the following outline:

- In subsection 8.1 some fundamental controls when seeking equilibrium values by *ab initio* calculation are discussed and results for pure Ni, Al and their compound $L1_2$ Ni_3Al are shown.
- In subsection 8.2 some comments and examples are given as to the choice of the supercell when dealing with defects and (slightly) disordered intermetallic crystals. Finally the choice of the supercells used in this thesis is introduced and justified.
- In subsection 8.3 the two most common techniques for calculating jump profiles (straight path and Nudged Elastic Band method) are introduced, explained and compared. The applicability of the two methods for various types of jump profiles is discussed.
- In subsection 8.4 the influence of neighboring defects lying outside the 4-atom window is investigated.

8.1 Ab initio calculations: Convergence and validation

8.1.1 Methodology

Before starting calculations of *ab initio* based values for supercells containing point defects, migration energies, etc. the reliability of the the data has to be assured by performing convergency tests for the pure metals and the undisturbed compound. Therefore the following basic steps were performed:

- The convergency of the choice of grid of k -points was checked for all above mentioned structures.
- The convergency of the choice of the cut-off energy of the plane waves was checked.
- The consistency with experimental behavior - groundstate, magnetic properties, was shown.

The commonly used criterion for convergency is (see VASP manual [39]) that the difference of the energy values between two increasing choices of values (e.g. k -points, cutoff energy) should be less than ± 1 meV/atom.

8.1.2 Results: equilibrium values of pure Metals Ni and Al

In this PhD thesis the study and modelling of order-disorder transitions in the $L1_2$ ordered intermetallic compound Ni_3Al is in the center of interest. Nevertheless, if it is planned to use *ab initio* calculated energies in kinetic Monte-Carlo simulations, it is very important to check whether the way of calculating these is reliable in pure metallic elements as a benchmark test.

Both, Ni and Al, condense (at standard conditions) in the face centered cubic structure. However, when talking about ground states there is one difference. In fcc Ni the ground state is ferromagnetic while fcc Al is paramagnetic. This behavior is reproduced by VASP.

Following the basic steps listed in Sec. 8.1 it is found (see Fig. 8.1) that a cut-off energy for plane waves of 450.0 eV and a Γ -centered k -points grid of $16 \times 16 \times 16$ leads to reliable results.

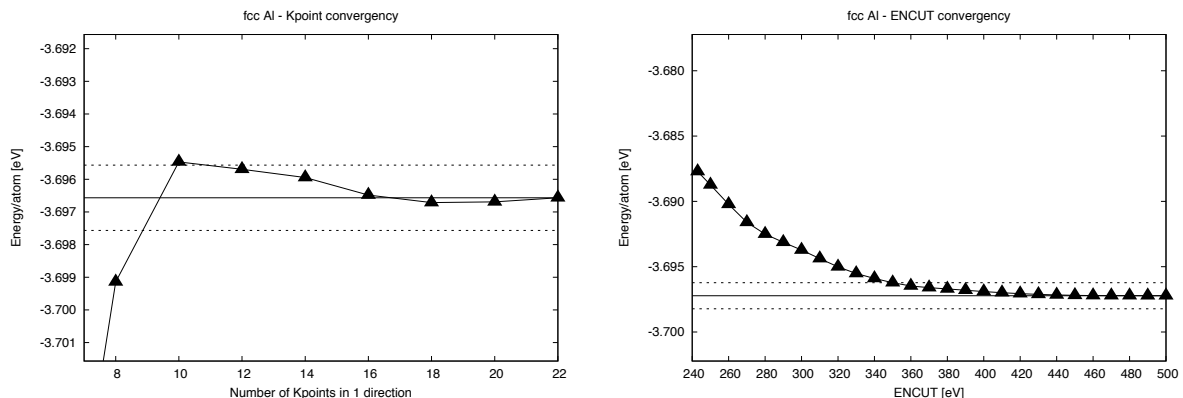


FIGURE 8.1: Face centered cubic Aluminum: convergence of the most important parameters in VASP. On the left the number of k -points in each direction is drawn against the energy per atom at a fixed volume. On the right side the cut-off energy for plane waves is plotted versus the energy/atom. The most reliable energy value corresponding to the highest setting is drawn as a solid line. The area of reliable settings is shown as dashed lines (± 1 meV/atom).

In static calculations the tetrahedron method with Blöchl corrections is suggested for very accurate total ground state energies (see VASP manual [39]). The volume of the supercell was varied by $\pm 5\%$ around the equilibrium value and the related energy values were fitted with the Birch-Murnaghan equation of states [40].

This equation of states has the advantage that its fitting parameters directly yield the equilibrium parameters of pure fcc Al and spin polarized fcc Ni. This procedure is shown in Fig. 8.3 and the results are summarized in Tab. 8.1.

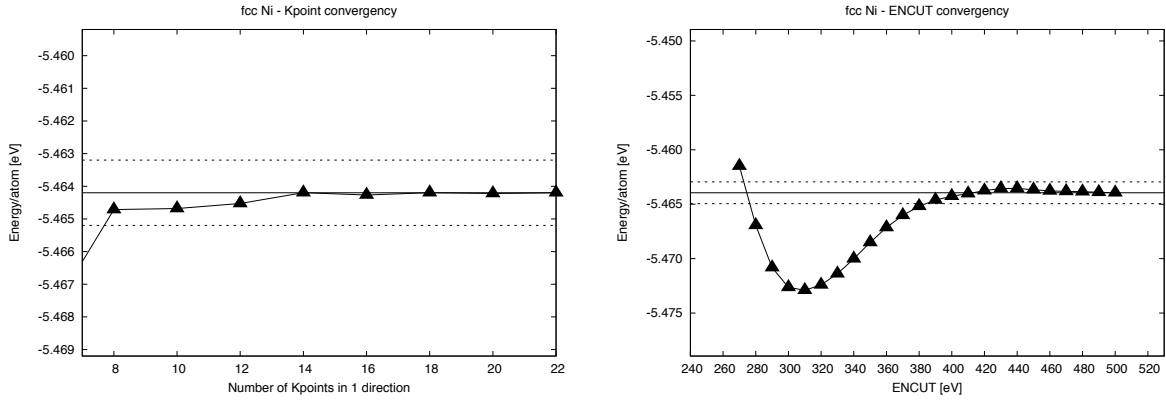


FIGURE 8.2: Face centered cubic Nickel (spin polarized): convergence of the most important parameters in VASP. On the left the energy per atom at a fixed volume is drawn against the number of k -point in each direction. On the right side the energy/atom is plotted versus the cut-off energy for plane waves. The most reliable energy value corresponding to the highest setting is drawn as a solid line. The area of reliable settings is shown as dashed lines (± 1 meV/atom).

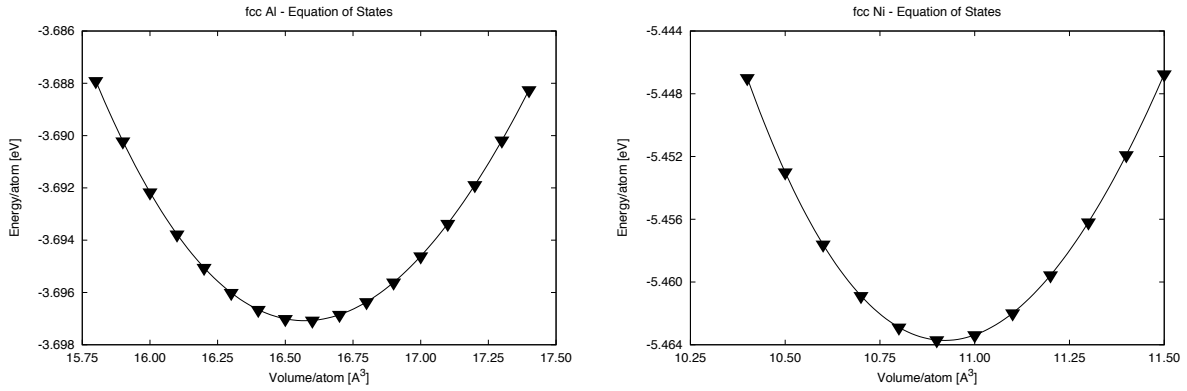


FIGURE 8.3: Energy vs. volume curve for fcc Aluminium and fcc Nickel. All values are per atom. The symbols show the calculated values.

	Reference	a₀	B	B'
Al	present work	4.047	74.8	4.7
	exp. [42],[47]	4.050	72	
	comp. [41]	4.041	77	4.7
Ni	present work	3.522	195.8	4.9
	exp. [42],[47]	3.524	186	
	comp. [46]	3.540	192	

TABLE 8.1: Calculated equilibrium values of fcc Al and spinpolarized fcc Ni. The lattice constant a_0 is in \AA , the bulk modulus B in GPa, B' is the pressure derivative of B. The values of E are in eV/atom. Experimental (exp.) and computed (comp.) values are shown for comparison.

8.1.3 Results: equilibrium values of undisturbed L1₂ Ni₃Al

The L1₂ unit cell contains 4 atoms (see Fig. 4.1). As pointed out in Section 4, no lattice distortion in the L1₂ structure is possible because of symmetry. Based on this fact a variation of the volume of this structure with the atoms fixed on their lattice sites (i.e. a simple scale transformation) directly leads to the ground state energy.

Following the basic steps in chapter 8.1 reliable values for the k -points sampling and the cut-off energy for plane waves were obtained for this 4-atom supercell. The results are given in Fig. 8.4. The cut off energy was chosen as 460 eV and the Monkhorst-Pack grid was chosen as 16 x 16 x 16 k -points.

With these settings the equilibrium values of L1₂ Ni₃Al were calculated by varying the volume of the 4-atom supercell by $\pm 5\%$ around the equilibrium value and by fitting of the obtained energy values to the Birch-Murnaghan equation of states. This method is shown in Fig. 8.5.

A summary of the obtained fitting results is given in Tab. 8.2. An important agreement should be pointed out here. The obtained lattice constant of 3.57 \AA is in good agreement with the experimental value of 3.58 \AA (e.g. [43]). This value is very important as we fix the volume of bigger supercells. Therefore it is needed for the following calculations.

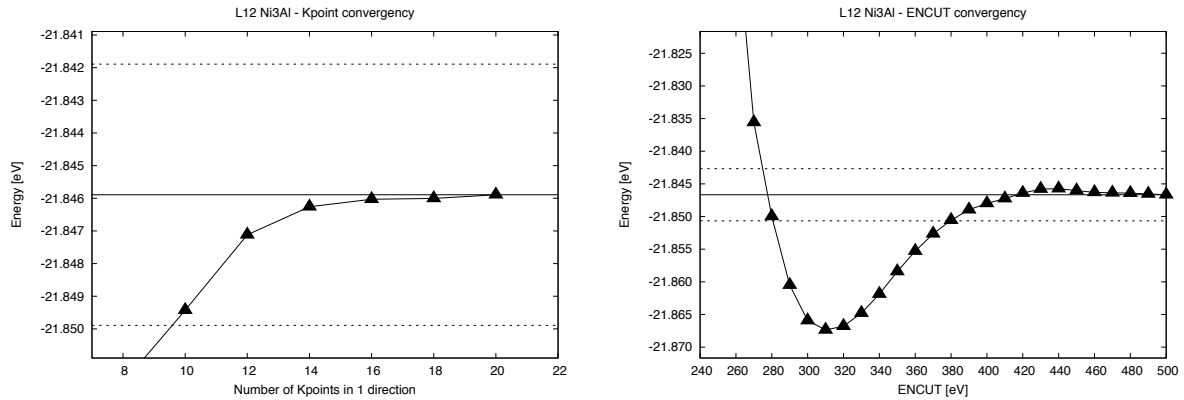


FIGURE 8.4: L1₂ Ni₃Al: convergence of the most important parameters in VASP. On the left the energy per atom at a fixed volume is drawn against the number of k -point in each direction. On the right side the energy/atom is plotted versus the cut-off energy for plane waves. The most reliable energy value corresponding to the highest setting is drawn as a solid line. The area of reliable settings is shown as dashed lines (± 1 meV/atom).

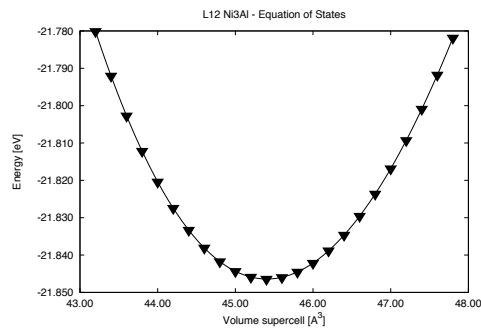


FIGURE 8.5: Energy vs. volume curve L1₂ Ni₃Al. All values are per atom. The symbols show the calculated values.

	Reference	a ₀	B	B'
L1₂ Ni₃Al	present work	3.567	180	4.7
	exp. [43],[44]	3.576	175	
	comp. [45]	3.576	177	

TABLE 8.2: Calculated equilibrium values L1₂ Ni₃Al. The lattice constant a₀ is in Å, the bulk modulus B in GPa, B' is the pressure derevative of B. Experimental (exp.) and computed (comp.) values are shown for comparison

8.2 *Ab initio* calculations: The size of the supercell

8.2.1 Methodology

When dealing with atomic defects in intermetallic systems, one has to be aware that different sizes of supercells correspond to different defect concentrations due to the limited size and the periodic boundary conditions (PBC) applied. Embedding one point defect into a supercell composed of 2x2x2 conventional cubic lattice cells (this corresponds to 32 lattice sites) arithmetically leads to a relatively high amount of defects (3.13 %) in the whole cristal. Even the computationally more expensive choice of a 3x3x3 supercell - containing 108 lattice sites - overestimates the density of vacancies (0.72 %) by several orders of magnitude. Therefore, in order to gain reliable results, it is necessary to use one of the following setups:

- **Sufficently large supercells**

This choice is (unfortunately) not feasible with respect to *ab initio* calculation. Even the VASP code that is highly optimised with fast algorithms is only able to handle supercells up to about 300 atoms with proper accuracy.

- **Supercell with fixed surface atoms**

As suggested in various publications (e.g. see [48]) the atoms at the 'surface' of the supercell are kept fixed at their ideal positions. Furthermore only atoms fully contained in the defined supercell may relax. In other words the fixed atoms act as a border of the locally disturbed crystal to the undisturbed solid. This choice

of supercell leads to a study of the number of conventional unit cells needed in a computation supercell to obtain reliable results. In other words, if the residual forces on the fixed atoms vanish or are reasonably small the chosen supercell is sufficiently large.

8.2.2 Results

It was decided to employ the second approach introduced in the previous chapter 8.2.1, i.e. supercells with fixed surface atoms. Supercells at a constant volume with the lattice spacing given in Tab. 8.2 were constructed for two sizes: 32 lattice sites ($2 \times 2 \times 2$ $L1_2$ unit cells) and 108 lattice sites ($3 \times 3 \times 3$). These two sizes of supercells are the smallest possible choices for the calculations of defect properties and activation energies in $L1_2$ Ni_3Al .

After a full relaxation (for technical details of the relaxation procedure see chapter 6.4) of the ions left free to relax the residual forces on fixed atoms were calculated for both sizes of supercells. An illustration is shown in Fig. 8.6. Here the forces are shown as arrows. Fig. 8.6 point out the importance of the choice of the larger $3 \times 3 \times 3$ supercell since the mentioned forces appear to be sufficiently small.

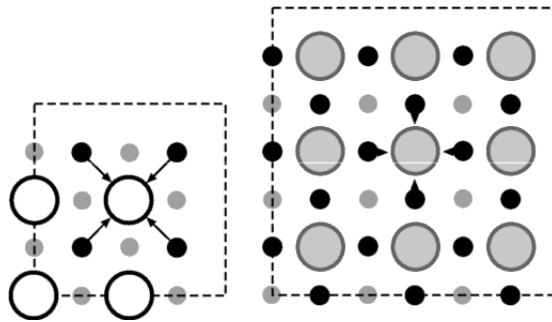


FIGURE 8.6: [010] side view: Residual forces (black arrows) on fixed 'surface' atoms of a 32-atom (left) and 108-atom (right) supercell of $L1_2$ Ni_3Al containing an Al vacancy. Aluminum atoms are drawn with larger dots in white (top layer) and grey (lower layers). Nickel atoms are small black (top layer) and grey (lower layers) circles. The dotted line indicates the 'surface' of the supercell.

In order to analyze in more detail the result shown in Fig. 8.6, the relaxations of atoms surrounding one point defect have been compared for $2 \times 2 \times 2$ and $3 \times 3 \times 3$ supercells. The displacements of surrounding atoms related to their specific coordination shell were analyzed with respect to their equilibrium distance in a perfectly ordered crystal. The results are given in Figs. 8.8 - 8.14. It is seen that the displacement of atoms with respect to the equilibrium distance decreases with distance (number of coordination shell). While it decreases to zero in the case of the larger choice of supercell it does not vanish for a $2 \times 2 \times 2$ supercell. In these figures also the atom type is distinguished. Ni atoms are shown with black and Al atoms with blue symbols. It is noted that for the choice of a $2 \times 2 \times 2$ supercell in general only the nearest neighbors are allowed to relax.

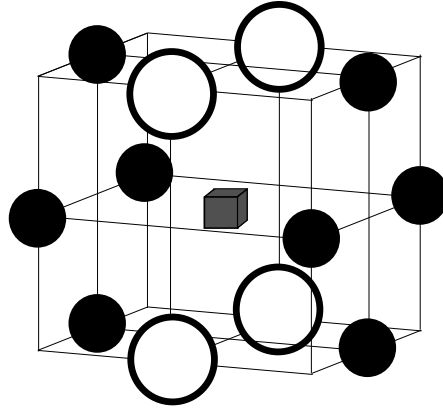
Ni vacancy

FIGURE 8.7: Local configuration around a Ni vacancy. Here only nearest neighbors are shown.

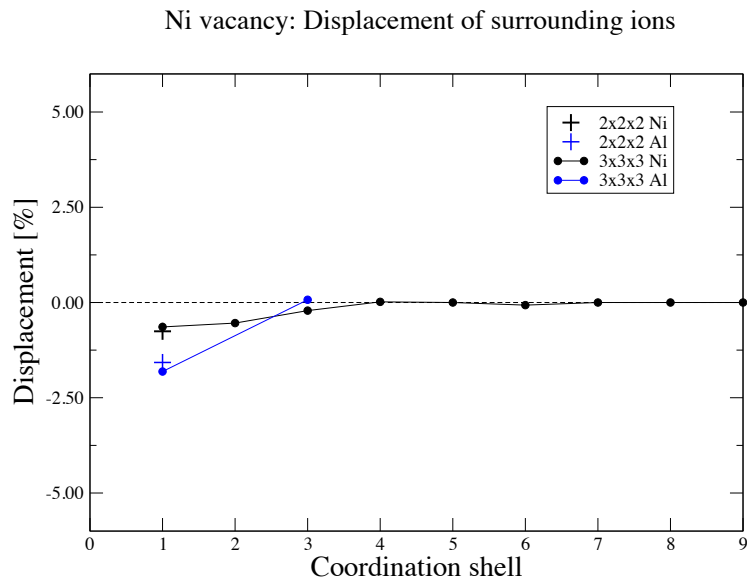


FIGURE 8.8: Relaxation of neighboring ions of a vacancy located on the majority sublattice in %. The values are given with respect to the equilibrium distance of the coordination shell in a perfectly ordered crystal. Two different choices of the size of the supercell are compared: $2 \times 2 \times 2$ with 32 lattice sites (crosses) and $3 \times 3 \times 3$ with 108 lattice sites (dots). Displacements of Ni and Al atoms are shown by black and blue symbols, respectively.

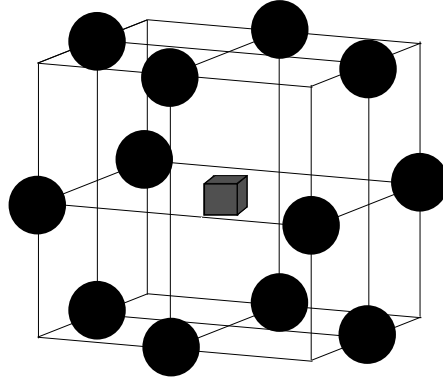
Al vacancy

FIGURE 8.9: Local configuration around an Al vacancy. Here only nearest neighbors are shown.

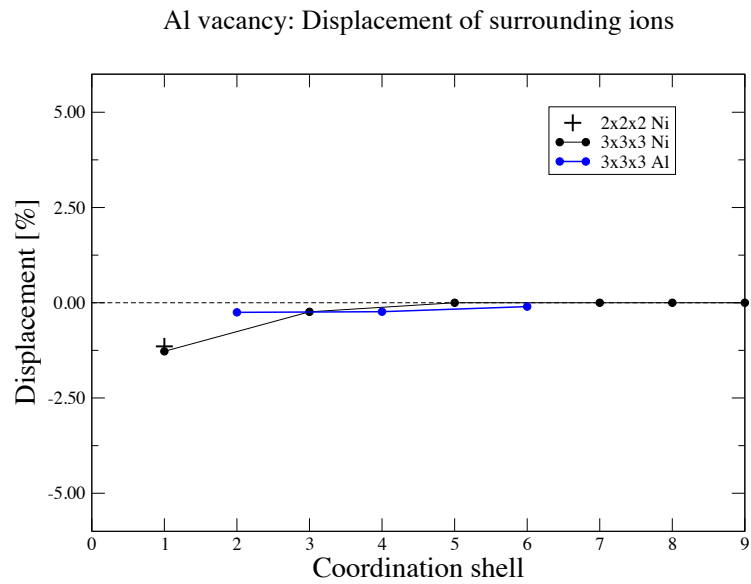


FIGURE 8.10: Relaxation of neighboring ions of a vacancy located on the minority sublattice in %. The values are given with respect to the equilibrium distance of the coordination shell in a perfectly ordered crystal. Two different choices of the size of the supercell are compared: $2 \times 2 \times 2$ with 32 lattice sites (crosses) and $3 \times 3 \times 3$ with 108 lattice sites (dots). Displacements of Ni and Al atoms are shown by black and blue symbols, respectively.

Ni antisite

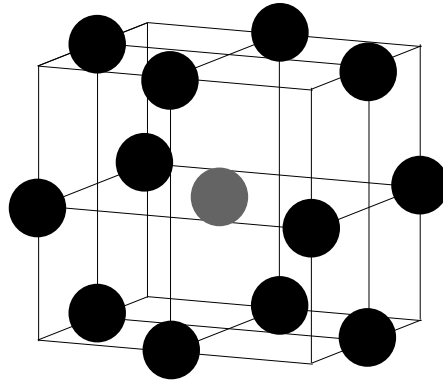


FIGURE 8.11: Local configuration around an Ni antisite. Here only nearest neighbors are shown.

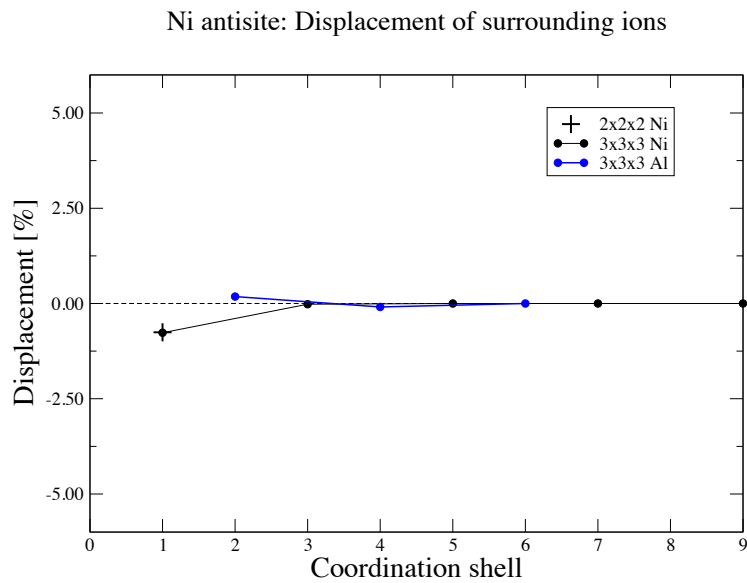


FIGURE 8.12: Relaxation of neighboring ions of an antisite located on the minority sublattice in %. The values are given with respect to the equilibrium distance of the coordination shell in a perfectly ordered crystal. Two different choices of the size of the supercell are compared: 2x2x2 with 32 lattice sites (crosses) and 3x3x3 with 108 lattice sites (dots). Displacements of Ni and Al atoms are shown by black and blue symbols, respectively.

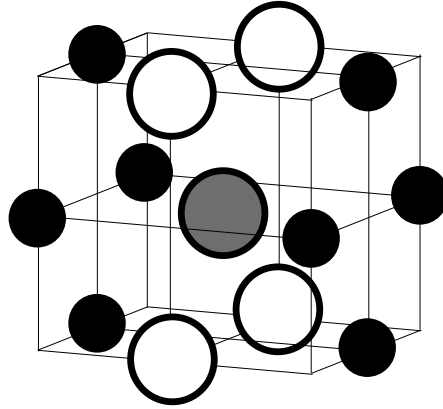
Al antisite

FIGURE 8.13: Local configuration around an Al antisite. Here only nearest neighbors are shown.

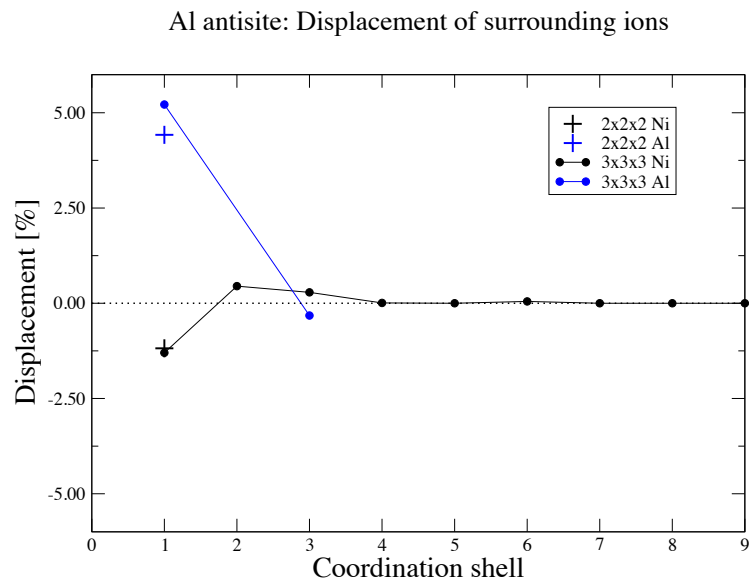


FIGURE 8.14: Relaxation of neighboring ions of an antisite located on the majority sublattice in %. The values are given with respect to the equilibrium distance of the coordination shell in a perfectly ordered crystal. Two different choices of the size of the supercell are compared: 2x2x2 with 32 lattice sites (crosses) and 3x3x3 with 108 lattice sites (dots). Displacements of Ni and Al atoms are shown by black and blue symbols, respectively.

8.3 Realistic jump paths: straight vs. curved

In this thesis the focus lies on the calculation of reliable energy values of saddle point states for jumping atoms to apply them to kinetic Monte-Carlo simulations. Generally speaking there are two main methods of calculating these energies: static displacement of the jumping atom from its initial towards its final state and the Nudged Elastic Band method which allows for more degrees of freedom, enabling thus a curved jump path.

In the following both methods are introduced and compared. Since the demand for computational power is dramatically different for these approaches *ab initio* calculations for selected jumps were done and checked against each other. After general remarks in chapter 8.3.1, methodology and technical details of the calculations are given in Sec. 8.3.2. Results and interpretations are shown in chapter 8.3.2.1.

8.3.1 General remarks

Static displacement:

First the initial and final equilibrium positions of the jumping atom are obtained after relaxation of the supercell. As a second step a jump path between these two equilibrium positions is defined. Usually this is done by linear interpolation of these positions. In other words the atom changes its position on a straight path from its initial towards its final position. Now the jumping atom is moved step by step ('statically') along this path.

In *ab initio* calculations of each of the intermediate states the jumping atom is fixed at its current position and not allowed to relax. This is done in order to avoid a relaxation towards its initial or final equilibrium position which is a local minimum of energy and therefore energetically more favorable than the intermediate state.

The advantage of this approach is that it saves computer time. All states can be treated as independent of each other and can therefore be calculated one by one.

Nudged Elastic Band:

On the other hand the Nudged Elastic Band method as introduced in section 3.2 is the state-of-the-art tool for the calculation of optimum jump paths and corresponding diffusion barriers. However, this method is computationally demanding.

The reason is the following: As pointed out above for each jump path one has to define a set of images of the whole system along the reaction path. According to the NEB formalism all of these images have to be relaxed in parallel since they are connected with 'springs'. Especially when dealing with large supercells (more than 100 atoms) very large and powerful computer resources are needed to get results within a reasonable time. Therefore it has to be decided carefully whether the achieved improvement of the results justifies the increased amount of computing time necessary to do a full NEB calculation.

If we calculate configurations with high symmetries the straight jump path method and NEB yield the same results. In the next chapter results of VASP calculations of these two approaches for 2x2x2 calculation supercells are shown and compared allowing thus to decide for which jump types NEB calculations are mandatory.

8.3.2 Methodology

For the choice of the 2x2x2 supercell (32 lattice sites) jump profiles for all jump and selected window types introduced in chapter 4.4 were calculated using the NEB method and a straight path. For this choice of supercell the Nudged Elastic Band method is not as expensive as it is for a 3x3x3 supercell (108 lattice sites) and therefore gives insight whether the achieved improvement of the results justifies the increased amount of computing time necessary to do a full NEB calculation.

This part is designed as follows. First technical details for both the straight jump path and the NEB method are introduced. Then *ab initio* results for energies and jump paths are given and compared, rounded up by an analysis.

General:

All calculations presented here were carried out within a 2x2x2 supercell containing 32 lattice sites. These lattice sites are occupied by an arrangement of 31 atoms and 1 vacancy. In the initial state the vacant spot is always located in the center of the supercell. The jumping atom is a nearest neighbor of the vacancy. A Monkhorst-Pack k -point grid of 6x6x6 is used. All settings are similar to the settings introduced in section 8.2 including the approach that the atoms located at the surface of the supercell are fixed.

Specific: straight jump path

After a full relaxation of the initial and final configuration of each jump type the equilibrium positions were linearly interpolated. This interpolation was done for 5 intermediate positions of the jumping atom. This odd number of steps ensures that the transition state where the jumping atom is located within the 4-atom window is very near to one of the calculated positions.

After the calculation of each energy value along the jump path these 5 values were interpolated by cubic splines from which the extrema were determined. Specifically, the maximum value was taken as the saddle point energy E_s . This value is significantly different from the value at half the jump path (within the 4-atom window) only for the case B: $\beta \rightarrow \alpha$ where the maximum is shifted slightly to the final equilibrium position. In all

other jumps the saddle point is located practically within the window.

Specific: Nudged Elastic Band

All saddle point energies for jump profiles and their corresponding jump paths were calculated with the NEB method as follows. Like above the fully relaxed configurations of the initial and final states were interpolated linearly as a starting point for the algorithm. In the case of NEB three relaxable images of the system were defined while the initial and the final images were kept fixed at their equilibrium states. The criterion that a saddle point state was found was that the absolute tangential force acting on the image in the middle of the chain be lower than 0.1 eV/Å.

If no image fulfilling this criterion is found after a full relaxation, first the tangential forces of all calculated images are interpolated to have an estimation for an image corresponding to the saddle point position where the tangential force is zero. Then the two fully relaxed images lying closest to this estimation and having a change of the sign of their tangential forces are fixed and linearly interpolated as a starting point for the following NEB calculation step. This is repeated until the saddle point is identified.

8.3.2.1 Results

In Tabs. 8.3 - 8.6 the numerical results of the *ab initio* calculations are summarized and in Figs. 8.16 - 8.22 the graphical representation of these values is given.

It can easily be seen that in the majority of the calculated jump and window types the NEB calculations lead to the same results as the straight jump path assumption. This indicates that the jumping atom stays on its 'direct' way towards its new equilibrium position. Only in the case of the order keeping jump B: $\alpha \rightarrow \alpha$ (see Tab. 8.4) it is found that the NEB method has to be employed. An example of the jump path for this case is shown in Fig. 8.23. The jumping B atom takes its optimum jump path by avoiding other B atoms contained within the 4-atom window.

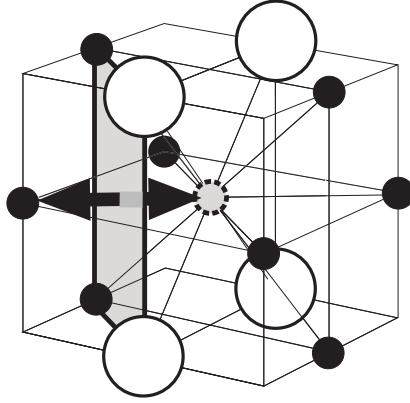
Order-keeping Ni jumps

FIGURE 8.15: Local configuration of order-keeping Ni jumps. This environment corresponds to perfect long range order.

Jump type	Window configuration	Position	ΔE_{is}	
			straight	NEB
<u>A: $\alpha \rightarrow \alpha$</u>	0	0.500	1.03	1.03
	1	0.500	1.01	1.01
	2-1	0.500	1.11	1.11

TABLE 8.3: Barrier heights ΔE_{is} for order-keeping Ni jumps and selected window configurations calculated with the straight jump path and the Nudged Elastic Band method. Values were calculated *ab initio* within a 2x2x2 supercell. All energies are in eV. The position in fractions of the jump path of the saddle point calculated with the NEB method is also shown. For the definition of window configurations see Fig. 4.6 in Sec. 4.4.

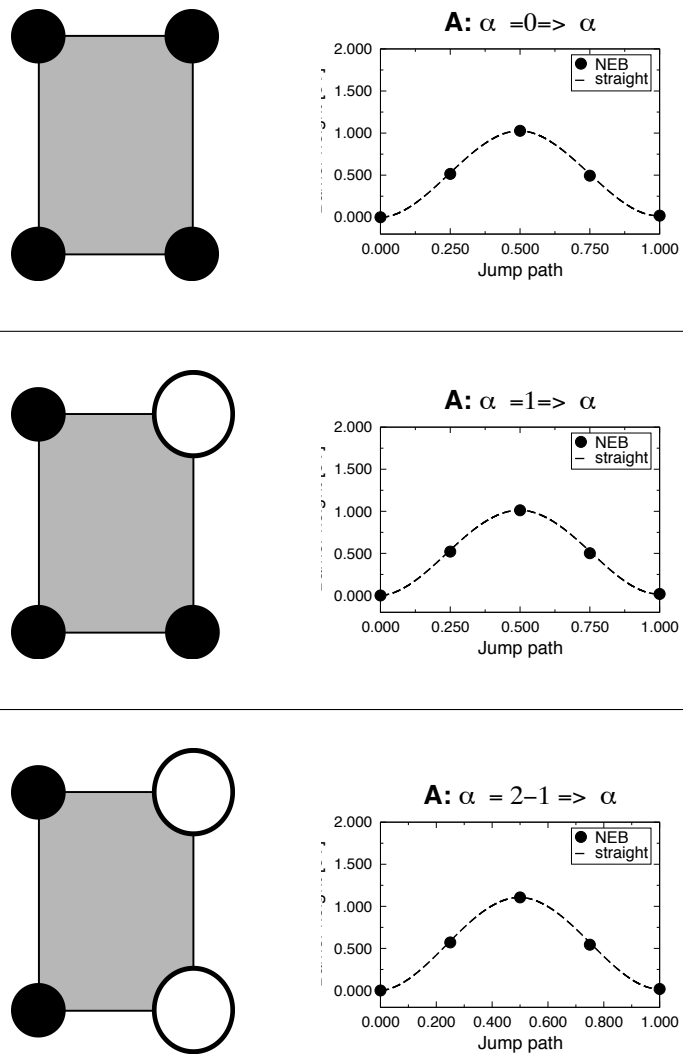


FIGURE 8.16: Comparison of jump profiles via static displacement along a straight path (dotted) and the NEB method (full circles) for Ni jumps in the $L1_2$ structure with different window configurations (for definitions see Fig. 4.6 in Sec. 4.4). Energy values are in eV.

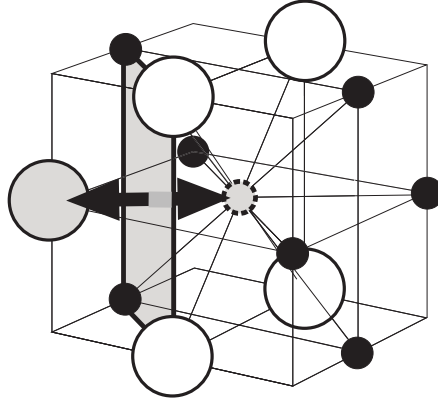
Orderkeeping Al jumps

FIGURE 8.17: Local configuration of order-keeping Al jumps. This environment corresponds to the highest possible degree of order.

Jump type	Window configuration	Position	ΔE_{is}	
			straight	NEB
B: $\alpha \rightarrow \alpha$	0	0.500	0.28	0.27
	1	0.500	0.57	0.52
	2-1	0.500	0.92	0.78

TABLE 8.4: Barrier heights ΔE_{is} for order-keeping Al jumps and selected window configurations calculated with the straight jump path and the Nudged Elastic Band method. Values were calculated *ab initio* within a 2x2x2 supercell. All energies are in eV. The position in fractions of the jump path of the saddle point calculated with the NEB method is also shown. For the definition of window configurations see Fig. 4.6 in Sec. 4.4.

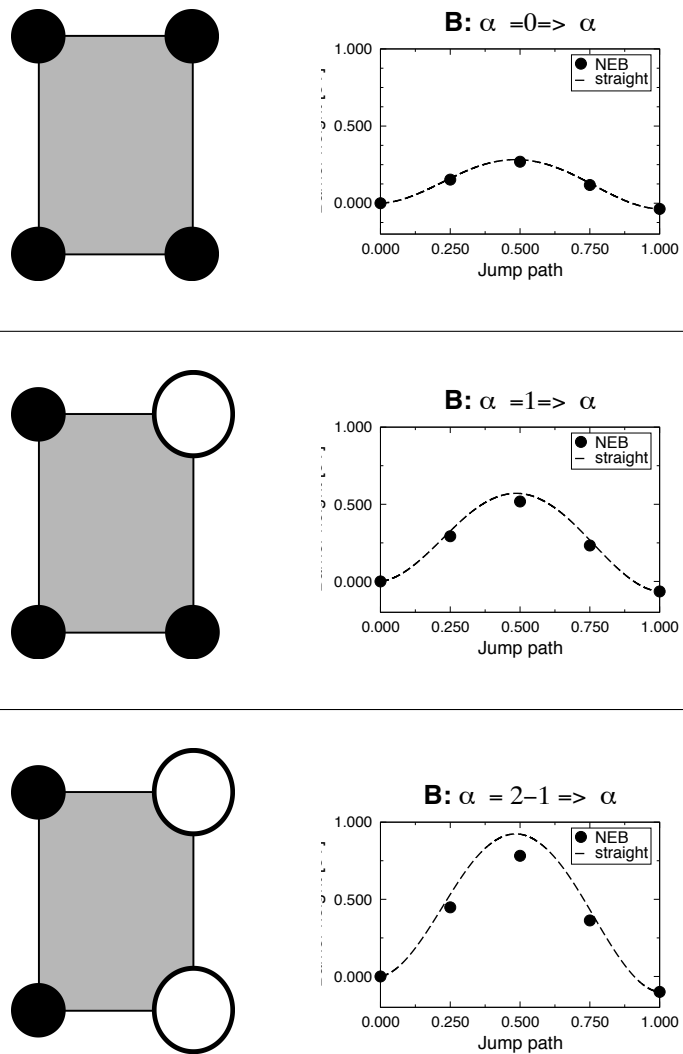


FIGURE 8.18: Comparison of jump profiles via static displacement along a straight path (dotted) and the NEB method (full circles) for order-keeping Al jumps in the $L1_2$ structure with different window configurations (for definitions see Fig. 4.6 in Sec. 4.4). Energy values are in eV.

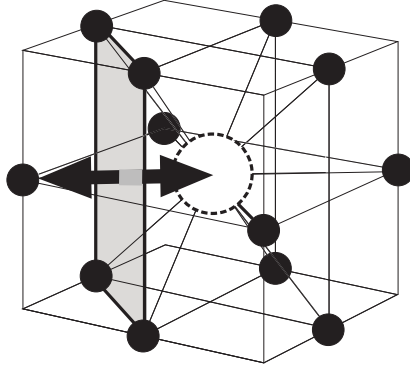
Ordering - disordering Ni jumps

FIGURE 8.19: Local configuration of ordering-disordering Ni jumps. This environment corresponds to perfect long range order.

Jump type	Window configuration	Position	ΔE_{is}	
			straight	NEB
<u>A: $\alpha \rightarrow \beta$</u>	0	0.500	1.04	1.04
	1	0.516	1.44	1.44
	2-1	0.531	1.71	1.71
	2-2	0.516	1.45	1.45

TABLE 8.5: Barrier heights ΔE_{is} for ordering-disordering Ni jumps and selected window configurations calculated with the straight jump path and the Nudged Elastic Band method. Values were calculated *ab initio* within a 2x2x2 supercell. All energies are in eV. The position in fractions of the jump path of the saddle point calculated with the NEB method is also shown. For the definition of window configurations see Fig. 4.6 in Sec. 4.4.

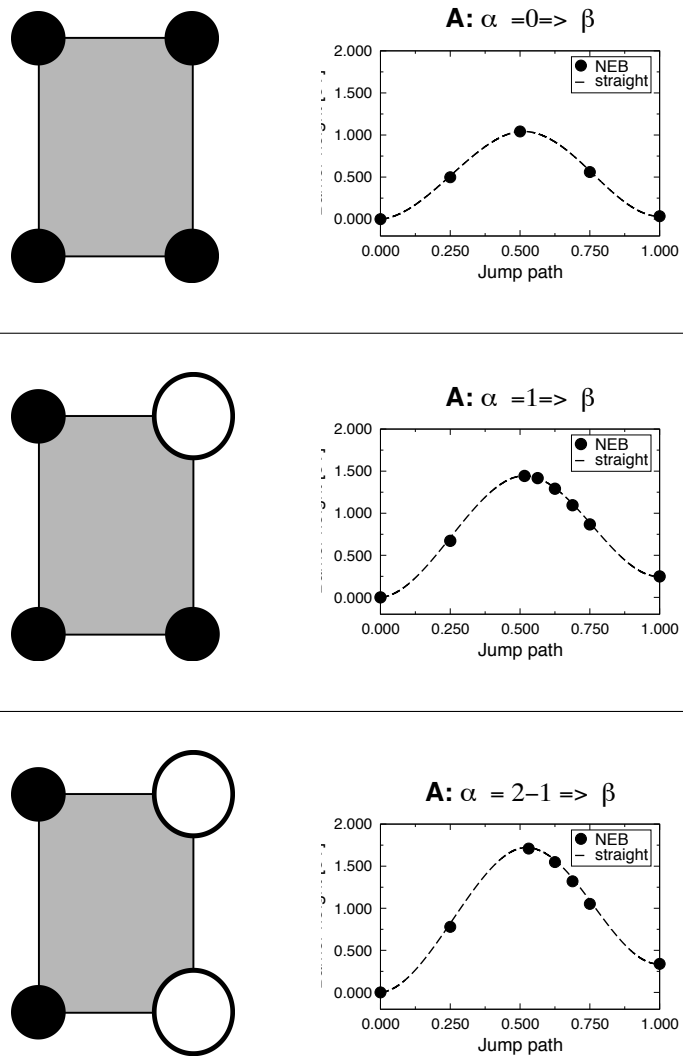


FIGURE 8.20: Comparison of jump profiles via static displacement along a straight path (dotted) and the NEB method (full circles) for ordering-disordering Ni jumps in the $L1_2$ structure with different window configurations (for definitions see Fig. 4.6 in Sec. 4.4). Energy values are in eV.

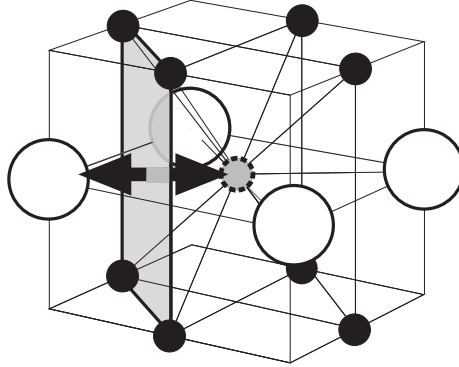
Ordering - disordering Al jumps

FIGURE 8.21: Local configuration of ordering-disordering Al jumps. This environment corresponds to perfect long range order.

Jump type	Window configuration	Position	ΔE_{is}	
			straight	NEB
<u>A: $\alpha \rightarrow \beta$</u>	0	0.625	1.08	1.08
	1	0.563	1.61	1.59

TABLE 8.6: Barrier heights ΔE_{is} for ordering-disordering Al jumps and selected window configurations calculated with the straight jump path and the Nudged Elastic Band method. Values were calculated *ab initio* within a 2x2x2 supercell. All energies are in eV. The position in fractions of the jump path of the saddle point calculated with the NEB method is also shown. For the definition of window configurations see Fig. 4.6 in Sec. 4.4.

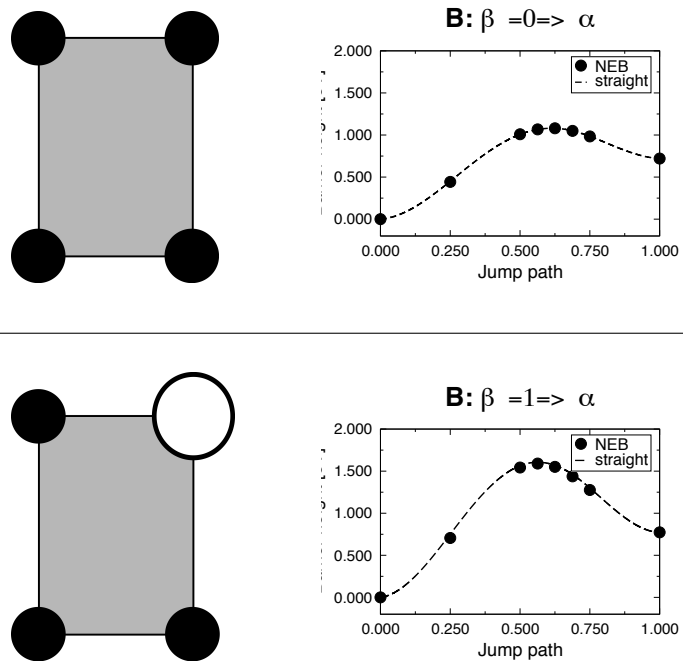


FIGURE 8.22: Comparison of jump profiles via static displacement along a straight path (dotted) and the NEB method (full circles) for ordering-disordering Al jumps in the $L1_2$ structure with different window configurations (for definitions see Fig. 4.6 in Sec. 4.4). Energy values are in eV.

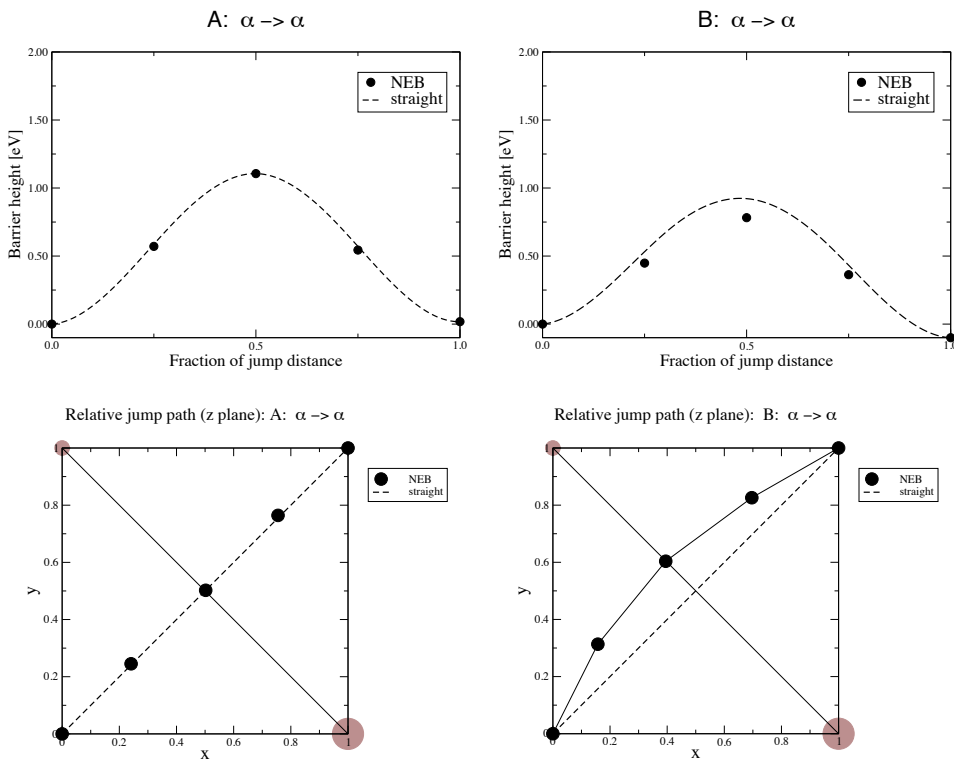
Example for jump paths

FIGURE 8.23: Comparison of jump profiles via static displacement along a straight path (dotted) and the NEB method (full circles) for order preserving jumps in the $L1_2$ structure at perfect order. The corresponding jump paths are shown in the lower part of the columns.

8.4 Dependence of saddle point on neighboring defects at various distances

For intermetallics like L1₂ Ni₃Al diffusion is known to proceed by a vacancy mechanism. Therefore vacancies are located on regular lattice sites and allow one atom sitting in their first coordination shell (nearest neighbors) to exchange its position with it. In order to perform this jump the atom has to pass a saddle point located between its initial and final position. After this exchange the vacancy is located on the position where the jumping atom was sitting before.

The energetics and the geometric relations of a single atom jump can be divided into 3 main stages (Fig. 8.24):

1. Initial equilibrium position with corresponding energy E_i
2. Saddle point state and energy E_s
3. Final equilibrium position with energy E_j

In the general case the difference of final energy E_j and initial energy E_i is zero for any order-preserving jump process while it differs for any ordering-disordering exchanges. A jump that leads to a higher degree of disorder usually is connected to an elevated final energy E_j with respect to E_i .

Let us have a closer look on the saddle point state. We already know that to exchange its position with the vacancy in the L1₂ structure a jumping atom has to squeeze through a 4-atom window, introduced in Chapter 4.3. This window is located in the middle of the jump path and can bear different atomic arrangements.

To point out the influence of the configuration of this window on the saddle point energy of diffusion jumps we regard the following jump process (Fig. 8.24). An A atom exchanges its position with a vacancy located on the minority sublattice (A: $\alpha \rightarrow \beta$). The environment is slightly disordered since one antisite B _{α} is located within the window. In the initial state of the jump the atom is in an equilibrium position with its equilibrium energy E_i . Moving towards its final position and final energy E_j the A atom reaches a saddle point state with the corresponding energy E_s and a position within the 4-atom window.

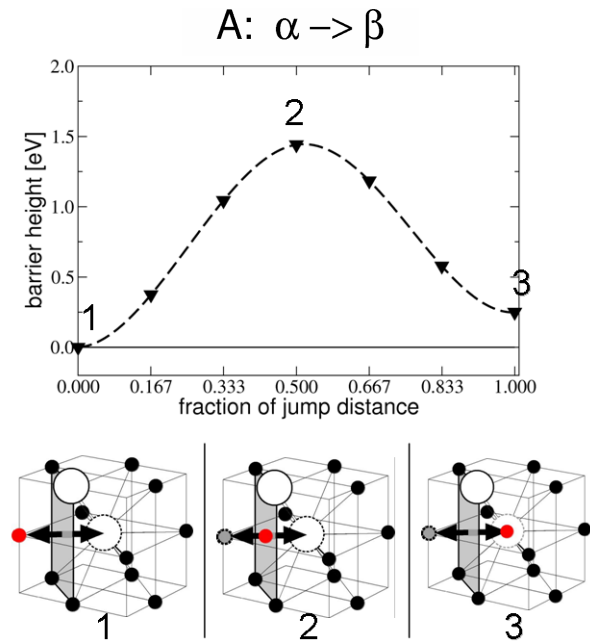


FIGURE 8.24: The energetics of the three main stages of an elementary jump process and their corresponding atomic configurations: An atom (red) moves from its initial position (1) to the final position (3). The saddle point state (2) is reached as the jumping atom enters the 4-atom window (grey).

Intuitively it is only natural to expect that the saddle point energy E_s strongly depends on the explicit configuration of this 4-atom window since all atoms contained in it are nearest neighbors of both, the jumping atom and the vacancy and have to be moved a little bit out of the way to let the jumping atom pass. Starting from this expectation we want to study the influence in a more quantitative way.

A jumps:

First we vary the positions of one B_α antisite within the first seven coordination shells with respect to the initial position of the jumping A atom and keep the distance to the vacancy fixed at nearest neighbor distance (Fig. 8.25 and Tab. 8.7).

Now the following picture arises: The biggest change of the barrier height energy due to the presence of a B antisite in the vicinity is found when it is located within the 4-atom window. The influence of the location of the antisite decays strongly with its distance to the initial position of the jumping atom. This is a strong indication that also in the general case the main influence on the jump barrier is exerted by the configuration of the 4-atom window. We therefore assume that antisites located outside this window have only second-order influence.

Index	Distance to jumping atom	E_{is}	ΔE_{ij}
reference barrier height		0.933	-0.03
(a)	0.707	1.227 (+0.294)	0.091
(b)	1.000	1.027 (+0.094)	0.136
(c)	1.225	0.964 (+0.031)	0.148
(d)	1.414	0.946 (+0.013)	0.070
	1.732	0.958 (+0.025)	-0.05
	1.871	0.938 (+0.005)	-0.05

TABLE 8.7: A jumps (for index see Fig. 8.25). The distance of the Al antisite to the initial position of the jumping atom in units of the lattice spacing a , and all energies are given in eV. The configurations of the last two rows are not shown in Fig. 8.25.

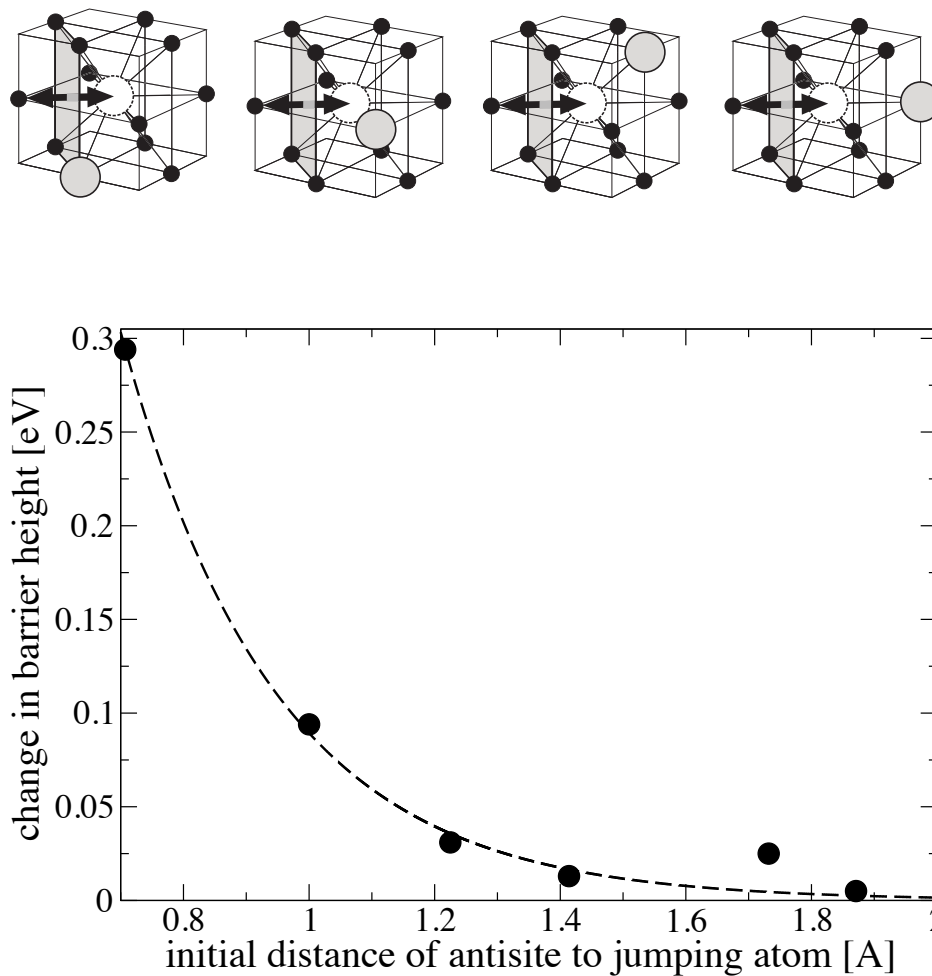


FIGURE 8.25: Top: Initial configurations of the environment for the ordering-disordering jump $A:\alpha \rightarrow \beta$ for B antisites within the first four coordination shells. Bottom: Change of barrier height with respect to the barrier height of the jump in a perfectly ordered lattice (through a 4-atom window consisting of A atoms only). The dotted line is a guide to the eyes to demonstrate the declining influence of antisites with respect to distance to the jumping atom.

B jumps:

Secondly we also study the change of the barrier height E_{is} with respect to the initial distance of one B_α antisite for a jumping B atom (B: $\beta \rightarrow \alpha$). Here the same behavior is found (see Fig. 8.26 and Tab. 8.8).

Index	Distance to jumping atom	E_{is}	ΔE_{ij}
reference barrier height		0.937	0.713
	0.707	1.354 (+0.417)	0.784
	1.225	1.101 (+0.164)	0.964
	1.581	1.013 (+0.076)	0.726

TABLE 8.8: B jumps (for index see Fig. 8.25). The distance of the Al antisite to the initial position of the jumping atom in units of the lattice spacing a , and all energies are given in eV. The configurations of the last two rows are not shown in Fig. 8.25.

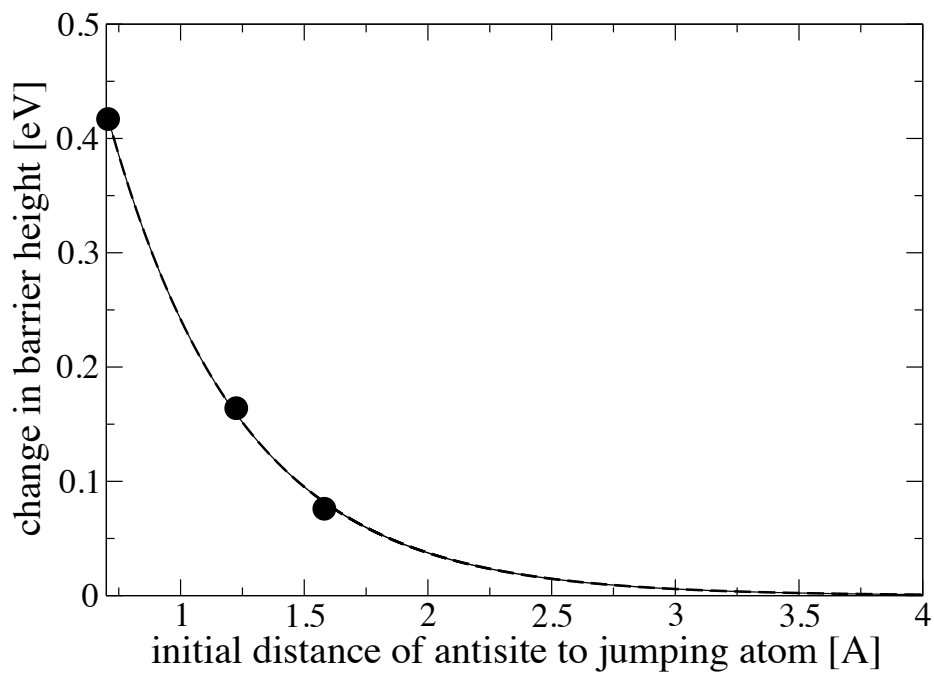


FIGURE 8.26: Change of barrier height for B jumps with respect to the barrier height of the jump in a perfectly ordered lattice (through a 4-atom window consisting of A atoms only). The dotted line is a guide to the eyes to demonstrate the declining influence of antisites with respect to distance to the jumping atom.

Chapter 9

Summary and Outlook

In this work an improved strategy to calculate energy barriers for atom jumps in Kinetic Monte-Carlo (KMC) simulations is proposed. The energy barriers enter in the jump frequencies via a Boltzmann factor in the framework of the transition state theory. The improvement introduced consists in taking explicitly account of the atomic environment of the transitional saddle point. In order to study the dependence on environmental configuration, extensive ab initio studies of jump energy profiles were undertaken, using the VASP software package. L1₂-ordered Ni₃Al was taken as a model system, as it is a technically important intermetallic alloy and fulfils the requirements for the transition state theory to be applied, its diffusion operating by a nearest neighbor vacancy mechanism. From the methodological point of view, it was found necessary to adopt a calculation supercell of at least 3x3x3 conventional lattice cells, so as to keep atoms at the boundary of the supercell free from constraining forces. A careful study showed that the majority of jump paths can be considered as practically straight, and for only a small class of curved jumps the computationally expensive Nudged Elastic Band (NEB) method has to be employed in order to obtain a minimal energy barrier. In the fcc lattice (on which L1₂ is based) nearest neighbour jumps into vacant lattice sites have to take place through a rectangular 4-atom window of nearest neighbors to the initial and final positions of the jumping atom. As expected, the occupancy of the 4-atom window exerts the predominant influence on the barrier height. Antisite defects near the jumping atom which do not form part of this window exert a lesser influence which decays in an exponential-like way with distance.

The energy profiles as obtained from the ab initio calculations were analyzed extracting a pure energy barrier as the arithmetic mean of the forward and backward jump barrier. As a general trend, the pure barrier increases with the number of the larger Al atoms,

the amount of the increase depending on jump type, however.

Finally, the impact on kinetics of configuration-dependent saddle points was studied by some model KMC simulations of the transition from perfectly ordered to partly ordered alloy configurations. Here, the jump barriers were constructed by reversing the analyzing process, viz. superimposing the pure barrier heights on the energy ramp from the initial to the final position of a jump. For the energy ramp, a simplified Ising type interaction model was used. The effect of the new paradigm when compared with fixed saddle point heights is startling indeed. It can be seen by a statistics of the various jump types that there is a clear bias towards energetically cheaper jump windows, even if their relative abundance is smaller. On the integral scale, there is a slowing-down of the order parameter kinetics due to correlation effects. Making allowance for variable saddle point heights does therefore make a difference.

Outlook

As usual no work or model can be considered as being immune against further improvement. Two items of improvement should be mentioned here, and ideas for ways how to put this into work are given.

As it was shown in the two publications included (chapters 6 and 7) the calculation of initial (and final) energies used in kinetic Monte-Carlo simulations was based on pair interaction potentials up to the next nearest neighbor. These potentials have been well tested and they lead to realistic equilibrium degrees of order. Especially they describe very well the order-disorder transition temperature of Ni₃Al. Since the main focus of this work is laid on the explicit treatment of saddle point energies these well tested potentials were used as a basis ramp for barrier heights calculated by *ab initio* calculations. However, it would be desirable to also treat the energetics of the initial (and final) state with higher accuracy and on better theoretical foundation.

One way to obtain reliable potentials with *ab initio* precision could be the cluster expansion (CE) [49]. In this treatment multi-body interactions between atoms are matched to values computed with high computational effort. This approach leads to a description of configuration dependent energy values in a large computational cell with the precision of calculations based on density functional theory. The cluster expansion approach is well established for the treatment of binary and ternary systems. However, the treatment of a binary compound containing vacancies is a non-trivial task and is therefore in the center of interest of ongoing research.

Undoubtedly the configuration of the 4-atom window has the greatest influence on the explicit height of the saddle point energy. This was demonstrated in chapter 8.4 for jumps of atoms of sort A and B with an antisite in their surroundings. However, a certain influence of antisites at a distance larger than the nearest neighbor distance might not be negligible. Since *ab initio* calculations for all possible neighborhood configurations are not feasible, an other way has to be found to treat this dependence satisfactorily. One way would be to select some of these neighborhood configurations at random and feed them into an energy expression that works as a trainable neural network [50].

The cluster expansion might also come in handy since each configuration dependent value can be - theoretically - fitted by CE. Ways to carry out this tasks are of great interest and are presently in the focus of various working groups.

So stay tuned!

Bibliography

- [1] T. F. Lindsey and B. Fultz, in 'Diffusion in Ordered Alloys', Ed. B. Fultz, R. W. Cahn and D. Gupta, The Minerals, Metals and Materials Society, 1993, p. 91.
- [2] P. Oramus, R. Kozubski, V. Pierron-Bohnes, M. C. Cadeville, C. Massobrio and W. Pfeiler, *Mat. Sci. Eng. A* **324** 11 (2002).
- [3] P. Oramus, R. Kozubski, V. Pierron-Bohnes, M. C. Cadeville and W. Pfeiler, *Phys. Rev. B* **63** 174109 (2001).
- [4] R. Kozubski, P. Oramus, W. Pfeiler, V. Pierron-Bohnes and M. C. Cadeville, in 'Proceedings Solid-Solid phase transformations 99 (JIMIC-3)', Ed. M. Koiwa, K. Otsuka and T. Miyazaki, The Japan Institute of Metals, 1999, p. 473.
- [5] M. Athenes, P. Bellon, G. Martin, and F. Haider, *Acta mater.* **44** 4739 (1996).
- [6] M. Athenes, P. Bellon and G. Martin, *Acta Materialia* **48** 2675 (2000).
- [7] T.A. Abinandanan, F. Haider and G. Martin, *Acta mater.* **46** 4243 (1998).
- [8] P. Oramus, R. Kozubski, V. Pierron-Bohnes, M. C. Cadeville, C. Massobrio and W. Pfeiler, *Defect and Diffusion Forum* **194-199** 453 (2001).
- [9] P. Oramus, C. Massobrio, M. Kozlowski, R. Kozubski, V. Pierron-Bohnes, M. C. Cadeville and W. Pfeiler, *Comp. Mat. Sci.* **27** 186 (2003).
- [10] Y. Le Bouar and F. Soisson: *Phys. Rev. B* **65** 0914103 (2002).
- [11] K. Binder and D. W. Heermann, in 'Monte Carlo Simulation in Statistical Physics', 3rd edition, Springer, Berlin-Heidelberg 1997.
- [12] W. Pfeiler, W. Püschl and R. Podloucky, *J. Mat. Sci.* **39** 3877 (2004).
- [13] A.B. Bortz, M.H. Kalos and L.J. Lebowitz, *J. Comput. Phys.* **17** 10 (1975).
- [14] W.M. Young, E.W. Elcock, *Proc. Phys. Soc.* **89** 735 (1966).

- [15] F. Haider in 'Ordering and Disordering in Alloys', Ed. R. Yavari, Elsevier Applied Science, London and New York 1993, p. 215.
- [16] N. Metropolis, A.W. Rosenbluth, N.N. Rosenbluth and E. Teller, *J. Chem. Phys.* **21** 1087 (1953).
- [17] R.J. Glauber, *J. Math. Phys.* **4** 294 (1963).
- [18] W. Püschl, H. Numakura and W. Pfeiler, in 'Alloy Physics: A Comprehensive Reference', Ed. Wolfgang Pfeiler, Wiley-VCH, 2007, p. 173.
- [19] G. H. Vineyard, *J. Phys. Chem. Solids* **3** 121 (1957).
- [20] H. A. Kramers, *Physica* **7** 264 (1940).
- [21] S. Chandrasekhar, *Rev. Mod. Phys.* **15** 1 (1943).
- [22] H. C. Brinkman, *Physica* **22** 149 (1956).
- [23] S. A. Rice, *Phys. Rev.* **112** 804 (1958).
- [24] N. B. Slater, in 'Theory of Unimolecular Reactions', Cornell University Press, Ithaca, NY 1959.
- [25] O. P. Manley, *J. Phys. Chem. Solids* **13** 244 (1960).
- [26] G. Mills, H. Jonsson and G. K. Schenter, *Surf. Sci.* **324** 305 (1995).
- [27] A. Ulitsky and R. Elber, *J. Chem. Phys.* **92** 1510 (1990).
- [28] H. Jonsson, G. Mills and K. W. Jacobsen, in 'Classical and Quantum Dynamics in Condensed Phase Simulations', World Scientific Publishing Co. Pte. Ltd., Singapore 1997, p. 387.
- [29] R. G. Parr and W. Yang, in 'Density Functional Theory of Atoms and Molecules', Oxford University Press, Oxford 1989.
- [30] H. Eschrig, in 'The Fundamentals of Density Functional Theory', EAGLE 004 2003.
- [31] P. Hohenberg and W. Kohn, *Phys. Rev.* **136**, B864 (1964).
- [32] W. Kohn and L. J. Sham, *Phys. Rev.* **140**, A1133 (1965).
- [33] G. Kresse and J. Furthmüller, *Phys. Rev. B* **54**, 169 (1996).
- [34] G. Kresse and J. Furthmüller, *Comput. Mater. Sci.* **6**, 15 (1996).
- [35] P. Blöchl, *Phys. Rev. B* **50** 953 (1994).

- [36] G. Kresse and D. Joubert, *Phys. Rev. B* **59** 1758 (1999).
- [37] J.P. Perdew, J.A. Chevary, S.H. Vosko, K.A. Jackson, M.R. Pedersen, D.J. Singh and C. Fiolhais, *Phys. Rev. B* **46** 6671 (1992).
- [38] J.P. Perdew and Y. Wang, *Phys. Rev. B* **45** 13244 (1992).
- [39] <http://cms.mpi.univie.ac.at/vasp/vasp/vasp.html>
- [40] F. Birch, *Phys. Rev.* **71** 809 (1947).
- [41] B. Grabowski, T. Hickel and J. Neugebauer, *Phys. Rev. B* **76** 024309 (2007).
- [42] C.S. Barrett and T.B. Massalski, *Structure of Metals* (third ed.), Pergamon Press, Oxford (1980).
- [43] P. Villars and L. Calvert, in 'Pearsons handbook of crystallographic data for inter-metallic phases', American Society of Materials International, Materials Park, OH (1991).
- [44] C. Stassis, F.X. Kayser, C.K. Loong and D. Arch *Phys Rev B* **24** 3048 (1981).
- [45] H. Schweiger, O. Semenova, W. Wolf, W. Püschl, W. Pfeiler, R. Podlucky and H. Ipsen, *Scripta Materialia* **46** 37 (2002).
- [46] Y. Wang, Z.-K. Liu, L.-Q. Chen, *Acta Mat.* **52** 2665 (2004).
- [47] C. Kittel, in 'Introduction to solid state physics', New York: Wiley (1996).
- [48] C.G. Van de Walle and J. Neugebauer, *J. Appl. Phys.* **95** 3851 (2004).
- [49] J. M. Sanchez, *Phys. Rev. B* **48** 14013 (1993).
- [50] C. Bos, F. Sommer and E. J. Mittemeijer, *Modeling Simul. Mater. Sci. Eng.* **14** 273 (2006).

Publications and presentations

Publications

- 2011 M. Leitner, D. Vogtenhuber, W. Pfeiler and W. Püschl
Saddle point energies from ab initio jump profiles in MC simulation of order kinetics in intermetallics.
Solid State Phenomena **172-174** p. 1022-1027 (2011)
- 2010 M. Leitner, D. Vogtenhuber, W. Pfeiler and W. Püschl
Monte-Carlo Simulation Of Atom Kinetics In Intermetallics: Correcting The Jump Rates In Ni₃Al.
Intermetallics **18**, p. 1091-1098 (2010)

Invited lectures

- 2008 M. Leitner, D. Vogtenhuber, W. Pfeiler and W. Püschl
Monte-Carlo simulation of atom kinetics in intermetallics: Correcting the jump rates.
Hokudai Simulation Salon, Hokkaido University, Sapporo, Japan,
13.11.2008

Lectures

- 2012 T. C. Kerscher, M. Leitner, S. Müller, and R. Podloucky
Cluster expansions for kinetic Monte-Carlo simulations: towards time evolution with DFT accuracy.
DPG Frühjahrstagung 2012, Berlin, Germany, 26.03.2012
- 2010 M. Leitner, D. Vogtenhuber, W. Pfeiler and W. Püschl
Saddle point energies from ab initio jump profiles in MC simulation of order kinetics in intermetallics.
Solid-Solid Phase Transformations in Inorganic Materials - PTM 2010, Avignon, France, 11.06.2010
- 2008 M. Leitner, D. Vogtenhuber, W. Pfeiler and W. Püschl
Adaptive jump barrier height in Monte Carlo configuration kinetics.
DPG Frühjahrstagung 2008, Berlin, Germany, 25.02.2008

Posters

- 2012 M. Leitner, T. C. Kerscher, S. Müller, and R. Podloucky
Toward kinetic Monte-Carlo simulations with ab initio accuracy.
DPG Frühjahrstagung 2012, Berlin, Germany, 26.03.2012
- 2011 M. Leitner, D. Vogtenhuber, R. Podloucky, W. Pfeiler and W. Püschl
Ab initio calculation of variable saddle point energies for atom jumps in $L1_2$ ordered Ni_3Al .
DPG Frühjahrstagung 2011, Dresden, Germany, 14.03.2011
- 2010 M. Leitner, D. Vogtenhuber, W. Pfeiler and W. Püschl
A study of order-order transitions in $L1_2$ ordered Ni_3Al based on first-principles calculations.
DPG Frühjahrstagung 2010, Regensburg, Germany, 21.03.2010

Curriculum Vitae

Personal Data

Name	Mag. Martin Leitner
Date of birth	24.01.1977
Place of birth	Leoben, Austria
Marital status	Single

Studies

since 06/2007	Universität Wien, Vienna, Austria Doctoral student at the Department of Dynamics of Condensed Systems Supervisor Ao. Univ.-Prof. Dr. Wolfgang Püschl.
10/1997 – 06/2007	Universität Wien, Vienna, Austria Degree in Physics Diploma thesis on 'Kinetische Monte-Carlo-Simulation mit variabler Barrierenhöhe an L_1 -geordnetem Ni_3Al ', supervisor Ao. Univ.-Prof. Dr. Wolfgang Püschl.

Education

09/1983 – 06/1987	Volksschule, Weisskirchen, Austria
09/1987 – 06/1990	Hauptschule, Weisskirchen, Austria
09/1990 – 06/1991	Hauptschule, Obdach, Austria
09/1991 – 06/1996	Handelsakademie, Judenburg, Austria

Work experience

since 08/2010	Scientific staff at the working group of Ao. Univ.-Prof. tit. Univ.-Prof. Dr. Raimund Podlousky, Department of Physical Chemistry, Faculty of Chemistry, University of Vienna.
06/2007 – 08/2010	Scientific staff at the Department of Dynamics of Condensed Systems, Faculty of Physics, University of Vienna.